

Tamal Das

# Modeling, estimation and control for optimal operation of separation processes in oil and gas industry

Thesis for the degree of Philosophiae Doctor  
Trondheim, November 2018

**Norwegian University of Science and Technology**  
Faculty of Natural Sciences  
Department of Chemical Engineering



**NTNU**

Norwegian University of Science and Technology

Thesis for the degree of Philosophiae Doctor

Faculty of Natural Sciences

Department of Chemical Engineering

© 2018 Tamal Das.

ISBN 978-82-326-3258-9 (printed version)

ISBN 978-82-326-3259-6 (electronic version)

ISSN 1503-8181

Doctoral theses at NTNU, 2018:234

Printed by Skipnes Kommunikasjon

*This thesis is dedicated to my parents (Mani and Bapi)*



# Abstract

The **primary** focus of this thesis is to develop models for oil and gas separation processes. These models form the basis for estimation of unmeasured variables and the control of important process variables. The **secondary** focus of the thesis is to use the developed models (gravity separator, hydrocyclone and compact flotation unit) for optimization, control or estimation. Key results include in-depth analysis of the different models and optimal operation of a separation system that combines these models. The **tertiary** focus of this thesis is on state and parameter estimation, which includes results on estimation of unmeasured variables by the use of simplified models and estimation algorithms, such as Kalman filter or Moving horizon estimator. To cater to these focuses, the thesis is divided into four parts.

**Part I** demonstrates the need for models via a case study on determining optimal operating points for an oil-water separation system. The maximization of oil content in the oily product is chosen as the objective.

**Part II** showed the use of estimation methods in combination with estimation-oriented models for estimation of unmeasured variables. In addition, a chapter is included on a method called pathfollowing that alleviates some of the computational challenges encountered by advanced estimators, such as moving horizon estimator.

**Part III:** This part presents three dynamic models, one each for - inline deoiling hydrocyclone (HC), compact flotation unit (CFU) and gravity separator. These models are able to predict important variables, such as oil in water and water in oil, which are difficult to measure, especially subsea. The optimal operation of the CFU is studied with an objective to minimize the use of flotation gas. In addition, a dynamic subsea separation system is constructed using the three models. The optimal operation of this system is studied under changing disturbances in order to propose a simple control structure.

**Part IV:** This part concludes the thesis with some final remarks and the way forward. It covers two additional topics - guidelines for model development and use of process models in industry.



# Acknowledgments

This thesis work can not envisaged without the support provided by my supervisor Associate Professor Johannes Jäschke all throughout my PhD and numerous discussions with my co-supervisor Professor Sigurd Skogestad. A token of gratitude is due to my master thesis supervisor Dr. Christian Borchert, who encouraged me to take up doctoral studies in the first place.

I would like to thank my colleagues for work related technical discussions, for providing help with my work, for creating a relaxed work environment and for spending leisure time outside work. Thanks to officemates - Adriaen, Christoph, Eka and Dinesh and other PhD students - Adriana, Pablo, Julian, Sigve, Cansu, Tobias and Bahareh. A special thanks to Sindre Johan Heggheim, who contributed meticulously as a master student under my close supervision. His work completed my long awaited desire to make a satisfactory gravity separator model. With his work getting concluded I started to see the end of my PhD.

I spent a lot of time towards the end of my PhD partying together with Vladimiro and having interesting discussions with him on Chemical Engineering and a whole lot of other stuff. It was a fun time off-work, which kept me focused at work as I had things to look forward to outside work.

Thanks to the SUBPRO project, which made the PhD research period quite interesting not only due to the visits to companies, but also due to frequent social activities. I will never forget that SUBPRO organized a course for teaching skiing, without which I would not have dared to ski - a very important skill to have living in Norway.

A very very special thanks to my family - my mom, my dad and my sister. They encouraged me and believed in my abilities from far away in India. During my PhD, I spent a lot of my free time talking to Alexandra Kokoshnikova and spent a lot of my vacation time together with her. Her presence in my life was crucial in the middle stages of my PhD. I extend heartfelt thanks to all of you.

Tamal Das  
Oslo, November 2018



# Contents

<b>Abstract</b>	<b>iii</b>
<b>Acknowledgments</b>	<b>v</b>
<b>Contents</b>	<b>vii</b>
<b>List of figures</b>	<b>xi</b>
<b>List of tables</b>	<b>xiii</b>
<b>1 Introduction</b>	<b>1</b>
1.1 Motivation	1
1.1.1 Need for process models	2
1.1.2 Need for models in oil and gas industry	2
1.1.3 Data driven vs first principles based models	2
1.2 Scope	2
1.3 Structure and summary of the chapters in this thesis	3
1.4 Main contributions	4
1.5 List of publications included in the thesis	5
1.6 List of publications not included in the thesis	5
<b>I Steady state liquid-liquid separation system</b>	<b>7</b>
<b>2 Modelling and optimization of liquid-liquid separation system</b>	<b>9</b>
2.1 Introduction	9
2.2 Process description	10
2.3 Models	11
2.3.1 Simplified models for inline cyclonic separators	11
2.3.2 Simplified model for gravity separator	13
2.4 Results	15
2.5 Conclusions	16
	vii

<b>II</b>	<b>Estimation results</b>	<b>17</b>
<b>3</b>	<b>Estimation of unmeasured disturbances in gravity separator</b>	<b>19</b>
3.1	Introduction . . . . .	19
3.2	Process description . . . . .	20
3.3	Model description . . . . .	21
3.4	Estimator . . . . .	24
3.5	Results and discussion . . . . .	25
3.6	Conclusion . . . . .	26
<b>4</b>	<b>Moving horizon estimator using pathfollowing approach</b>	<b>27</b>
4.1	Introduction . . . . .	27
4.2	Moving horizon estimation problem formulation . . . . .	29
4.2.1	A general Moving Horizon Estimation framework . . . . .	29
4.2.2	Ideal Moving Horizon Estimation . . . . .	30
4.2.3	Advanced step Moving Horizon Estimation framework . . . . .	31
4.3	Sensitivity in parametric nonlinear programming . . . . .	31
4.4	Sensitivity using pathfollowing . . . . .	33
4.5	Pathfollowing advanced step moving horizon estimation . . . . .	35
4.6	Case study . . . . .	36
4.7	Results . . . . .	37
4.7.1	Results from Ideal MHE, predicted MHE and EKF . . . . .	37
4.7.2	Results from pasMHE . . . . .	38
4.8	Conclusion and discussion . . . . .	38
<b>III</b>	<b>Models for control of separators and separation system</b>	<b>41</b>
<b>5</b>	<b>Modeling and control of an inline deoiling hydrocyclone</b>	<b>43</b>
5.1	Introduction . . . . .	43
5.2	Process Description . . . . .	44
5.3	HC modeling . . . . .	45
5.3.1	Model equations (PDEs) . . . . .	45
5.3.2	Discretization and equations for discretized volumes . . . . .	47
5.3.3	Re-entrainment equations . . . . .	50
5.3.4	Calculation of water quality . . . . .	51
5.3.5	Model parameters . . . . .	52
5.4	Control structure . . . . .	52
5.5	Results . . . . .	53
5.5.1	Steady state result . . . . .	53
5.5.2	Open-loop results . . . . .	54
5.5.3	Closed-loop results . . . . .	55
5.6	Conclusion . . . . .	55
<b>6</b>	<b>Modeling and optimal operation of a compact flotation unit</b>	<b>57</b>
6.1	Introduction . . . . .	57
6.2	CFU technology . . . . .	58

---

6.2.1	Concept of flotation . . . . .	58
6.2.2	A compact flotation unit design with induced gas flotation . . . . .	60
6.3	Control-oriented CFU model . . . . .	61
6.3.1	Modeling concept and assumptions . . . . .	61
6.3.2	Simplified initial swirl separation model . . . . .	63
6.3.3	Flotation model . . . . .	64
6.3.4	Model summary . . . . .	71
6.4	Case study . . . . .	71
6.4.1	Model parameters . . . . .	71
6.4.2	Dynamic model analysis (only stabilizing loop closed) . . . . .	71
6.4.3	Optimal operation . . . . .	74
6.5	Discussion and future work . . . . .	79
6.6	Conclusion . . . . .	81
<b>7</b>	<b>Modeling and optimal operation of a subsea separation system</b>	<b>83</b>
7.1	Introduction . . . . .	83
7.2	Coalescence based gravity separator model . . . . .	86
7.2.1	Process description . . . . .	86
7.2.2	Model description . . . . .	88
7.3	Optimal operation of a subsea separation system . . . . .	99
7.3.1	Separation system overview . . . . .	99
7.3.2	Case study and set-up . . . . .	101
7.3.3	Control structure design . . . . .	103
7.3.4	Analysis of the proposed control structure . . . . .	110
7.3.5	Controller tunings . . . . .	110
7.3.6	Closed loop simulation results . . . . .	111
7.4	Discussion . . . . .	116
7.5	Conclusion . . . . .	118
7.6	Acknowledgements . . . . .	119
<b>IV</b>	<b>Closing remarks</b>	<b>121</b>
<b>8</b>	<b>Conclusion and future work</b>	<b>123</b>
8.1	Conclusions . . . . .	123
8.2	Future work . . . . .	124
8.2.1	Validation of the models . . . . .	124
8.2.2	Optimal operation of a validated separation system . . . . .	124
8.2.3	Estimation using the validated models . . . . .	124
8.3	Guidelines for developing models . . . . .	124
8.4	Use of models in process industry . . . . .	125
<b>References</b>		<b>127</b>



# List of figures

2.1	The separation system. . . . .	10
2.2	Flow behavior inside a cyclonic separator. . . . .	12
2.3	Dimensions of the gravity separator. . . . .	14
2.4	Cross section at the beginning and end of the gravity separator. . . . .	14
2.5	Oil volume fractions of the outlets vs inlets in a deoiler. . . . .	15
2.6	Optimal flow splits of separators vs inlet oil volume fraction. . . . .	15
2.7	Optimal flow splits of separators vs inlet flow rate. . . . .	16
3.1	Schematic of gravity separation process. . . . .	20
3.2	Relating density to oil cut. . . . .	21
3.3	Batch analysis of water in oil emulsion. . . . .	21
3.4	Flow streams and variables in the model. . . . .	22
3.5	Area used in the model. . . . .	23
3.6	Control structure for gravity separator with Kalman filter. . . . .	24
3.7	True and estimated states and disturbances. . . . .	25
4.1	MHE initialization. . . . .	37
4.2	True states, EKF estimates and ideal MHE estimates. . . . .	37
4.3	Error between pasMHE solution and ideal MHE solution. . . . .	38
5.1	Schematic of an inline deoiling Hydrocyclone. . . . .	44
5.2	Swirl element. . . . .	45
5.3	Coordinate system and axial velocity profiles. . . . .	46
5.4	Discretizations. . . . .	48
5.5	Schematic of a single control volume. . . . .	48
5.6	HC control using OiW controller. . . . .	52
5.7	Steady state spatial profile of oil flow. . . . .	53
5.8	Open loop behavior of the hydrocyclone model. . . . .	54
5.9	Closed loop behavior of the hydrocyclone model. . . . .	55
6.1	Schematic of a flotation device. . . . .	59
6.2	Scenarios after collision between droplets and bubbles. . . . .	59
6.3	Gas flotation methods. . . . .	60
6.4	Simple CFU design considered in this paper. . . . .	61
6.5	Schematic view of the CFU model. . . . .	62
6.6	Loading process as a combination of an oil droplet and a free bubble. . . . .	62

6.7	Swirl split as a function of swirl intensity. . . . .	64
6.8	Control volumes. . . . .	66
6.9	Schematic of velocities. . . . .	67
6.10	Control loop for CFU with only stabilizing pressure loop closed. . . . .	72
6.11	Responses of the CFU with only a stabilizing pressure control loop closed. . . . .	73
6.12	Control loops for CFU with ratio control for water quality. . . . .	76
6.13	Optimal steady state number densities inside CFU represented spacially. . . . .	77
6.14	Dynamic responses showing optimal operation of CFU. . . . .	78
7.1	A subsea separation system. . . . .	84
7.2	Schematic of a three phase gravity separator. . . . .	86
7.3	Control volumes considered in gravity separator model. . . . .	88
7.4	Flows for each control volume in the gravity separator model. . . . .	90
7.5	Scenarios faced by sedimenting water droplets. . . . .	91
7.6	Control volume regions with different set of equations. . . . .	95
7.7	Our simulated subsea separation system. . . . .	99
7.8	Schematic of an inline deoiling hydrocyclone. . . . .	100
7.9	A schematic of a CFU. . . . .	101
7.10	Optimal steady state solution for nominal case. . . . .	105
7.11	Number densities in all control volumes in the gravity separator. . . . .	107
7.12	Control structure for the separation system. . . . .	109
7.13	Closed loop results for gravity separator. . . . .	112
7.14	Dynamic responses in droplet concentrations inside the gravity separator. . . . .	114
7.15	Closed loop results for hydrocyclones. . . . .	115
7.16	Closed loop results for compact flotation unit. . . . .	117

# List of tables

2.1	Properties of the oil and the brine used in the models . . . . .	10
2.2	Coefficients in the polynomial for estimating viscosity of emulsion . . .	11
2.3	Dimensions of the inline cyclonic separators . . . . .	11
2.4	Input to the gravity separator . . . . .	14
3.1	Simulation parameters . . . . .	25
5.1	Model parameters . . . . .	52
5.2	Steady state oil fractions . . . . .	53
6.1	Model parameters . . . . .	72
6.2	Controller tunings . . . . .	77
7.1	Model parameters for gravity separator . . . . .	102
7.2	Cases of inlet operating conditions . . . . .	105
7.3	Optimization results for different cases . . . . .	106
7.4	Loss from optimal under different disturbance cases. . . . .	110
7.5	Controller tunings using SIMC rules . . . . .	111



# Chapter 1

## Introduction

In this chapter we present the motivation for this thesis work, define the scope of the thesis and put the chapters into perspective. An overview of the thesis and a list of the publications that resulted from this thesis are given.

### 1.1 Motivation

Process control, process monitoring and condition monitoring are engineering disciplines that attempt to operate a process plant in a trouble-free manner, which enables a **safe, uninterrupted** and **optimal** operation. While safe operation ensures safety of the people working in the plant, and protection of the equipment and the environment, uninterrupted and optimal operation improves profitability of the plant. However, after safe operation, uninterrupted operation is prioritized over optimal operation because losses during interruptions are much worse than those during sub-optimal operation. Moreover, wanting to operate a plant optimally should not risk interruptions either.

The most important threats to a trouble-free plant operation are posed by changing disturbances and degradation of equipment. This begs for the plant to be operated in such a manner that under most circumstances, alarms are not triggered, safety systems are not activated and unplanned shutdowns are avoided. To meet these objectives, the operators working on the plant and, control and monitoring systems need to make judicious decisions continuously. These decisions are usually made based on the understanding of the process behavior and condition of equipment.

One way to gain understanding about the process behavior and equipment condition is to perform **experiments**, while the other is to develop **representative models**, often in combination with some experiments. Since conducting experiments to discover process behavior or nature of equipment degradation under all different operating conditions is inefficient and impractical, models are partially trusted. However, to blindly rely on models is advised neither.

Models need to be validated against experimental data before they are put to use. How much to trust a model is governed by the track record of the model in making close to accurate future predictions, especially in regions that have not been

validated. Provided a model is trusted, it can provide important information for developing control strategy, and methods for monitoring the process and equipment condition.

### 1.1.1 Need for process models

Typically, in process industry, models satisfy two main needs - **estimation of unmeasured variables** and **development of control strategy for optimal operation**. Models are very commonly used to infer variables that are not measured directly. Moreover, many models are treated as simulators to test control strategies. Finally, models are also useful for identification of optimal operating point as under certain circumstances, to predict what is optimal can be impossible without the help of a model.

### 1.1.2 Need for models in oil and gas industry

Within the oil and gas industry, safety is even more critical whereas profitability is very dynamic as oil prices fluctuate rapidly. Furthermore, operations are often taking place in a remote location, for example on a production platform, where a quick intervention to correct undesirable operating conditions is often difficult. Additional challenges surface when operations are subsea. Under subsea conditions, information about even fewer variables are available, either because they are unmeasured due to lack of qualified sensors for subsea use or because the sensors malfunction in subsea conditions. Besides, the regulations concerning oil and gas businesses are very strict. Hence, there is an even higher need for models in oil and gas industry to develop automation systems that can keep operations trouble-free and meet the regulatory requirements.

### 1.1.3 Data driven vs first principles based models

Since the amount of data logged in industry is in plenty, it is reasonable to employ data driven methods to infer useful information from logged data. However, data driven models are known to be very local in terms of region of validity and the parameters therein have no physical meaning, which makes it difficult to analyze the results from these models. Hence, in this thesis, data driven approaches were not used. First principles are used to develop models and the parameters in those models have either a direct physical meaning or are tuning parameters to compensate for the un-modelled effects.

## 1.2 Scope

In this thesis, the focus is on development of dynamic **models for separators** that are used for oil and gas processing. The separators considered in this thesis are gravity separator, hydrocyclone and compact flotation unit. The scope of the thesis also includes analysis of transient operation as well as optimal operation of these separators either individually or as part of a system consisting of all the separators. Estimation methods and application of estimation methods to obtain

unmeasured variables have been also included in the thesis. However, not all models have been studied for the suitability for estimation purposes. Model validation for any of the models is out of the scope of this thesis. Hence, all the analysis presented in this thesis are simulation based.

### 1.3 Structure and summary of the chapters in this thesis

This thesis is structured into four parts.

#### **Part I: Steady state liquid-liquid separation system**

**Part I** highlights the need for models for an oil-water separation system in order to determine optimal operating points. In **Chapter 2**, we present a separation system consisting of steady state models for three separators - a gravity separator, a de-oiling hydrocyclone and a de-watering hydrocyclone. Each separator has one operational degree of freedom i.e. flow split. The oil content in the oil rich product was maximized to find the three degrees of freedom. This work highlights the potential of simplified models to identify optimal operating points.

#### **Part II: Estimation results**

**Part II** shows some estimation results using models. In **Chapter 3**, we present a simplified dynamic gravity separator model based on a three layer principle, where the layers are water, oil and emulsion. This model is used with an extended Kalman filter to estimate inlet disturbances, such as inflow, oil cut and droplet diameter. This work highlights the benefits of using estimators and the potential of simplified dynamic models for estimation of unmeasured variables. In **Chapter 4**, we present an alternative approach called pathfollowing to solve a computationally expensive nonlinear moving horizon estimation (MHE) problem. This approach reduces the computational burden by solving a series of quadratic programs instead of nonlinear programs. This chapter highlights that alternative mathematical formulations of optimization problems can provide reasonably good solutions and can be real time implementable.

#### **Part III: Models for control of separators and separation system**

**Part III** presents three dynamic models, one each for - inline deoiling hydrocyclone, compact flotation unit and gravity separator. These models are used for control of these separators either individually or as part of a separation system. In **Chapter 5**, we developed a dynamic model for an inline de-oiling hydrocyclone and we presented a controller to control the oil in the water rich outflow. The chapter highlights the potential of modeling for regulatory control. In **Chapter 6**, we developed a dynamic model for a compact flotation unit (CFU) and we presented a control strategy for optimal operation of CFU including the control of oil concentration in the water outflow, which is a regulatory requirement in oil and gas industry. The chapter highlights the potential of modeling for regulatory control. In **Chapter 7**, we developed a dynamic coalescence driven gravity separator

model. This model is combined with the models from Chapter 5 and Chapter 6 to create a subsea separation system consisting of a bulk separation and a produced water treatment. This separation system is optimized using a steady state optimization problem in order to maximize the removal of water going out of the separation system. The solution of the optimization problem provides optimal operating points for each of the separators. A simple control structure is developed that ensures optimal operation without the need for any change in set-points of important variables when disturbances affect the process. The results present dynamic responses in each of the separators to changing disturbances. Additional results on droplet distribution within the gravity separator are also included to demonstrate the characteristics of the developed gravity separator model.

Some major insights from this chapter are that optimization is more meaningful when studying a separation system rather than individual separators, and that the tuning of controllers for regulatory control of each separator should be performed taking into account the responses from other separators. This chapter complements Chapter 2 by presenting sophisticated models and dynamic behavior of an entire separation system. Also, this chapter highlights that steady state optimization similar to the one in Chapter 2 can be performed with dynamic models as well. This chapter concludes the overall objective of the thesis work, which is to develop models that form the basis for estimation and control for optimal operation of separation systems in oil and gas processing.

## Part IV: Closing remarks

Chapter 8 concludes this thesis with a summary of the thesis and provides guidelines for possible future research that could follow the presented work. In addition, this chapter gives some advice to model developers and talks about the uptake of models in process industry.

### 1.4 Main contributions

There are three main contributions in this thesis:

1. Simple methods to develop models, demonstrated by development of
  - a coalescence based gravity separator model
  - a compact flotation unit model
  - an inline hydrocyclone model
  - a three layer based gravity separator model
2. Proposal of control structures for optimal operation of
  - a separation system consisting of bulk separation and produced water treatment
  - compact flotation unit
  - hydrocyclone
3. Pathfollowing approach to speed up the numerical solution of moving horizon estimation (MHE) problem.

## 1.5 List of publications included in the thesis

### Journal Papers

- T. Das, S. J. Heggheim, M. Dudek, A. Verheyleweghen and J. Jäschke, **Optimal operation of a subsea separation system consisting of a coalescence based gravity separator model and a produced water treatment.** *Submitted for publication in Industrial and Engineering Chemistry Research, 2018.*
- T. Das and J. Jäschke, **A simplified first-principles model of a compact flotation unit for use in optimization and control.** *Submitted for publication in Industrial and Engineering Chemistry Research, 2018.*

### Peer-Reviewed Conference Papers

- T. Das, J. Jäschke, **Modeling and control of an inline deoiling hydrocyclone.** *3rd IFAC Annual Conference on Decision and Control (CDC), 2018.*
- T. Das, J. Jäschke, **Pathfollowing approach for a sensitivity based moving horizon estimator.** *56th IEEE Annual Conference on Decision and Control (CDC), 2017.*
- T. Das, C. J. Backi and J. Jäschke, **A model for subsea oil-water gravity separator to estimate unmeasured disturbances.** *Computer Aided Chemical Engineering (European Symposium on Computer-Aided Process Engineering 27), vol. 40, 2017.*
- T. Das, P. F. Tyvold and J. Jäschke, **Modelling and optimization of compact subsea liquid-liquid separation system.** *Computer Aided Chemical Engineering (European Symposium on Computer-Aided Process Engineering 26), vol. 38, 2016.*

## 1.6 List of publications not included in the thesis

### Peer-Reviewed Conference Papers

- A. Reyes-Lúa, C. Zotică, T. Das, D. Krishnamoorthy and S. Skogestad, **Changing between Active Constraint Regions for Optimal Operation: Classical Advanced Control versus Model Predictive Control.** *Computer Aided Chemical Engineering (European Symposium on Computer-Aided Process Engineering 28), vol. 43, 2018.*



## Part I

# Steady state liquid-liquid separation system



## Chapter 2

# Modelling and optimization of compact subsea liquid-liquid separation system

Subsea separation systems require compactly sized separators because they are easier to install on the sea bed and require less material of construction to withstand high pressures subsea. The compactness of the separators is brought about by using cyclonic forces, which are many times stronger than gravitational force to drive separation. Existing models are typically intended for design purposes, but they are computationally intensive and are not suitable to be used in numerical optimization methods. Hence, in this work, we developed a simple, yet reasonably accurate model for a subsea separation system, in which the oil-water emulsion feed undergoes a preliminary bulk separation in a gravity separator into two crudely separated streams. A further purification is carried out for the oil-rich stream in a dewaterer and the water-rich stream in a deoiler. Our models calculate the oil cut in the outgoing streams based on separator design and operational parameters, such as flow split, feed flow rate, and oil cut of the incoming stream. The deoiler model was calibrated using data from literature and the system was used for optimization to maximize the oil cut in the oil-rich product using the flow splits of the individual separators as degrees of freedom. The model was used to study the optimal flow splits corresponding to different feed rates and inlet oil cuts.

*Published in Computer Aided Chemical Engineering. vol. 38, 2016.*

### 2.1 Introduction

Subsea processing of hydrocarbons can offer significant reduction in operating costs and capital costs and can prolong hydrocarbon production from low pressure reservoirs. Hence, it not only results in higher economic value, but also enables production from wells that are otherwise economically infeasible to extract from. However, the subsea facilities, being compact, are challenging to control due to short residence time of fluids within them. To be able to study and operate such systems optimally, a good model of the system is required. These models can provide results

that are reliable and easy to interpret, which empirical models fail to provide. In the past decade, several attempts have been made to understand oil-water separation. (Slot, 2013) modelled swirl separators for design purposes, while (van Campen, 2014) investigated droplet dynamics inside liquid-liquid axial cyclones. (Sayda and Taylor, 2007) provided a dynamic model for liquid-liquid separation in a continuous water-continuous gravity separator. In this work, we developed a system of simplified steady state models of separators to study optimal operation. We calibrate our deoiler model against experimental results provided by (van Campen, 2014).

## 2.2 Process description

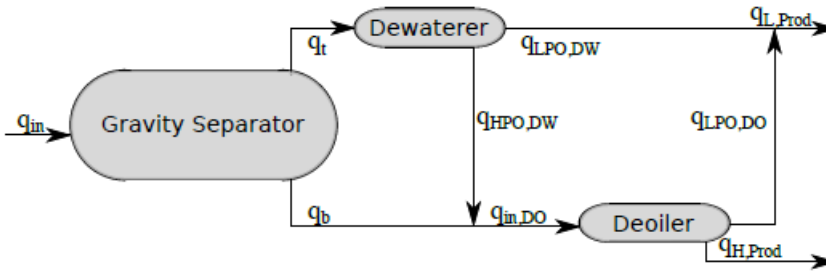


Figure 2.1: The separation system.

Figure 2.1 shows the overall separation system with the flow connections. The outlets from the gravity separator ( $G$ )  $q_t$  and  $q_b$  are the top and the bottom flows, respectively. The top flow  $q_t$  is likely to be rich in oil and needs to be treated further to remove the residual water in it. Hence, this stream is fed to the dewaterer ( $DW$ ). The  $LPO$  stream out of the dewaterer is oil-rich and combines with the oil-rich  $LPO$  stream out of the deoiler ( $DO$ ) to give the final oil product. The  $HPO$  stream out of the dewaterer that is rich in water combines with the water-rich stream out of the gravity separator and is fed into the deoiler for the removal of the residual oil. The water rich  $HPO$  stream out of the deoiler is the separated water out of the system.

The fluid properties used in the model are chosen in order to reconstruct the oil phase and the water phase used in the experiments conducted by (van Campen, 2014). To imitate the subsea scenario, brine is considered as the water phase. The densities and viscosities of the two phases are given in Table 2.1.

Table 2.1: Properties of the oil and the brine used in the models

Liquid	Density [ $kg/m^3$ ]	Viscosity [ $mPa.s$ ]
Oil	881	8.8
Brine	1064	1.0

## 2.3 Models

Liquid-liquid systems typically exist as emulsions made of a continuous phase and a dispersed phase. In case of oil-water systems, oil is usually the lighter of the two phases. An oil continuous system is called water-in-oil system (WiO) because the water phase exists as the dispersed phase, while a water continuous system is called oil-in-water system (OiW) consisting of oil as the dispersed phase. Due to the difference in densities of the two phases, water sediments in WiO systems or oil creams in OiW systems. The movement of the dispersed phase in emulsions can be approximately assumed to be described by the following terminal velocity expression given by Stokes' law, where  $r_d$  is the droplet radius of the dispersed phase,  $g$  is the acceleration due to gravity,  $(\rho_d - \rho)$  is the difference in densities of dispersed phase and the continuous phase and  $\mu$  is the viscosity of the fluid.

$$v = \frac{2r_d^2(\rho_d - \rho)g}{9\mu} \quad (2.1)$$

The viscosity of the emulsion is a function of the oil cut expressed as a third order polynomial in Table 2.2. The polynomial function has been fitted to the values measured by (van Campen, 2014). The emulsion undergoes a phase inversion from OiW to WiO at an oil cut of about 0.66. Hence, there are two polynomial fits, one representing oil cuts lower than 0.66 and the other representing oil cuts higher than 0.66 or water cuts lower than 0.34. The coefficients of the polynomial fits are given in Table 2.2.

Table 2.2: Coefficients in the polynomial for viscosity of emulsion  $\mu = \mu_c(1 + a\varphi + b\varphi^2 + c\varphi^3)$ , where  $\mu_c$  is the viscosity of continuous phase and  $\varphi$  is the volume fraction of the dispersed phase

Emulsion	$\varphi$ [-]	a [-]	b [-]	c [-]
Oil-in-water	0 - 0.66	110	-400	470
Water-in-oil	0 - 0.34	-1.6	27	23

### 2.3.1 Simplified models for inline cyclonic separators

All cyclonic separators considered in this paper are cylindrical in shape with one axial input and two axial outlets. The inlet conditions and the dimensions of the separators are given in the Table 2.3. The strength of the swirl element is represented by swirl number  $\Omega$ , which is further used in the model equations.

Table 2.3: Dimensions of the inline cyclonic separators

Length $L$ [m]	Outer pipe $R$ [m]	Deoiler inner pipe $R_i$ [m]	Dewaterer inner pipe $R_i$ [m]	Swirl number $\Omega$ [-], large / strong / weak
1.7	0.05	0.025	0.043	7.0 / 5.0 / 3.5

The cyclonic separators, i.e. deoiler and dewaterer have been modelled in the same way. We present the deoiler model here. The model for dewaterer is analogous

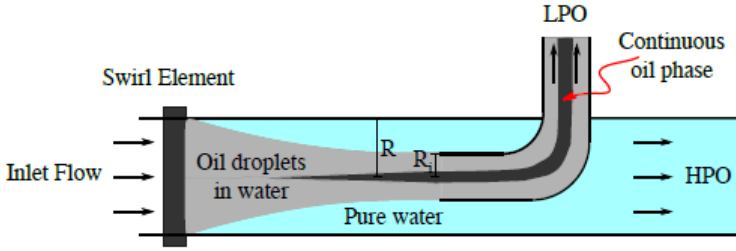


Figure 2.2: Flow behavior inside a cyclonic separator.

to that of the deoiler with an essential difference that the dispersed phase is water instead of oil. The deoiler has an axial inlet and two outlets. The outlet close to the axial center having a circular cross-section with radius  $R_i$  is called the light phase outlet (LPO) and the associated flow rate is denoted by  $q_{LPO}$ . The other outlet having an annular cross-section that starts at radius  $R_i$  and ends at the separator radius  $R$  is called the heavy phase outlet (HPO) and the associated flow rate is denoted by  $q_{HPO}$ . The flow inside the separator is assumed to be consisting of two plug flows corresponding to the two outflows, the velocities of which are given by (2.2).

$$v_z(r) = \begin{cases} \frac{q_{LPO}}{\pi R_i^2}, & \text{if } 0 \leq r \leq R_i \\ \frac{q_{HPO}}{\pi(R^2 - R_i^2)}, & \text{if } R_i < r \leq R \end{cases} \quad (2.2)$$

The plug velocities can be changed by changing the outlet flow split ( $FS$ ), which is  $q_{LPO}/q_{in}$ . When the fluid enters the separator, it encounters a swirl element that introduces a tangential component to the velocities of the fluid particles. The tangential velocity considered in this model at an axial position increases linearly from the center to a radius  $R_c$ , beyond which the velocity stays constant until the edge of the separator. The tangential velocity  $v_\theta^0$  at the inlet of the separator just after the swirl element is given by (2.3), where the  $v_\theta^{max}$  is expressed as a product of the bulk axial velocity  $v_{z,b}$  and the swirl strength  $\Omega$ .  $R_c$  represents Rankine vortex and typically has a value  $0.25R$ , as reported by (Dirkzwanger, 1996). The function for  $v_\theta^0(r)$  is not continuously differentiable at  $r = R_c$ . This function has been smoothed using method by (Balakrishna and Biegler, 1992) to enable ease in computation while using numerical optimization solver *fmincon* in MATLAB.

$$v_\theta^0(r) = \begin{cases} v_\theta^{max} \frac{r}{R_c}, & \text{if } 0 \leq r \leq R_c \\ v_\theta^{max}, & \text{if } R_c < r \leq R \end{cases} \quad (2.3)$$

The tangential velocity undergoes a decay along the length of the separator due to a loss in momentum, expressed by (2.4). The damping coefficient  $C_{decay}$  of 0.04 was reported by (Dirkzwanger, 1996) and (Slot, 2013). The radial velocity  $v_r$  of the dispersed droplets is calculated using the (2.1) and replacing the  $g$  in that

expression with radial acceleration  $v_\theta^2(r, z)/r$ .

$$v_\theta(r, z) = v_\theta^0(r) e^{\frac{-C_{decay}z}{2R}} \quad (2.4)$$

The oil volume fractions in the *LPO* and *HPO* streams are given by (2.5) and (2.6), respectively and the oil volume fraction at any spacial location  $\alpha_c(r, z)$  inside the separator is given by (2.7), which can be derived by oil flux balance. (2.5) assumes that all the droplets that enter the separator at radii lesser than  $r_{in}$  travel through the separator to end up in the *LPO*.

$$\alpha'_{LPO} = \alpha_{in} \frac{FS(R^2 - R_i^2) + (1 - FS)(r_{in}^2 - R_i^2)}{FS(R^2 - R_i^2)} \quad (2.5)$$

$$\alpha'_{HPO} = \frac{\alpha_{in} - \alpha'_{LPO}FS}{1 - FS} \quad (2.6)$$

$$\alpha_c(r, z) = \alpha_{in} \frac{FS(R^2 - R_i^2) + (1 - FS)(r_{in}^2 - R_i^2)}{(1 - FS)(r^2 - R_i^2) + FS(R^2 - R_i^2)} \quad (2.7)$$

The empirical correlation for droplet radius  $r_d$  is fitted against results by (van Campen, 2014).

$$r_d(v_\theta^{max}) [m] = \begin{cases} (-53.5v_\theta^{max} + 300) \cdot 10^{-6}, & v_\theta^{max} [m/s] \leq 4.45 \\ (-4v_\theta^{max} + 80) \cdot 10^{-6}, & v_\theta^{max} [m/s] > 4.45 \end{cases} \quad (2.8)$$

To compensate for the errors in assumption of a simplistic flow pattern, it is assumed that a re-entrainment of one flow in the other flow due to the difference in the velocities of the two plug flows is highly likely. Hence, a re-entrainment flow rate of  $q_{re-en}$  enters the *LPO* stream given by  $k_{re-en}(v_{LPO} - v_{HPO})$ , where parameter  $k_{re-en}$  was determined to be  $2.10^{-4} m^2$  by fitting the model to the experimental results by (van Campen, 2014). Accordingly, changes are made in the oil volume fraction  $\alpha_{LPO}$ , while  $\alpha_{HPO}$  is computed as  $(\alpha_{in} - \alpha_{LPO}FS)/(1 - FS)$ .

$$\alpha_{LPO} = \frac{\alpha'_{LPO}(q_{LPO} - q_{re-en}) + \alpha'_{HPO}q_{re-en}}{q_{LPO}} \quad (2.9)$$

We solved for the inlet radius  $r_{in}$  of the entering droplet that will exit exactly at  $R_i$  at outlet boundary. To solve this boundary value problem (BVP), the radial velocity  $v_r$  was integrated using a second order, explicit Runge-Kutta integrator with a constant time step of one-tenth of the residence time  $L/v_{HPO}$ . The BVP was solved using a *shooting method* given by (Constantinides and Mostoufi, 1999), which uses the Newton-Raphson method.

### 2.3.2 Simplified model for gravity separator

The gravity separator has been modelled considering mono-dispersed oil droplets. The model is a steady state adaptation of the dynamic model given by (Sayda and Taylor, 2007), considering two phases instead of three phases. The separator

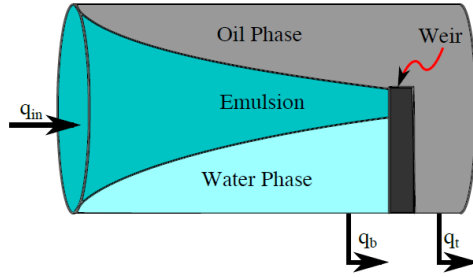


Figure 2.3: Dimensions of the gravity separator.

dimensions used in the model are given in Table 2.4. The droplets move vertically upwards travelling from the inlet of the separator to the end of the separator as shown in the Figure 2.3. The bottom outlet, i.e. the heavy phase outlet  $q_b$  contains the emulsion that remains un-separated under the weir height  $H_w$ . The height  $\Delta h$  at the end of the separator, which denotes the level of pure water phase, can be computed as  $Lv_v/v_h$ , where  $L$ ,  $v_h$ ,  $v_v$  are the length of the separator, the horizontal velocity and the vertical velocity of the droplets, respectively.  $v_h$  can be calculated

Table 2.4: Input to the gravity separator

Length $L$ [m]	Outer pipe $R$ [m]	Weir height $H_w$ [m]	Droplet diameter $D_d$ [ $\mu\text{m}$ ]
7	1.7	2.55	120

as  $q_b/A_b$ , where  $A_b$  is the section of the circular area of the cylinder lying below the weir as shown in Figure 2.4.  $v_v$  is given by (2.1). The oil volume fraction of the outlets  $\alpha_b$  and  $\alpha_t$  can be calculated as  $\alpha_{in}A_e/A_b$  and  $[\alpha_{in}q_{in} - \alpha_b q_b]/q_t$ , respectively, where  $A_e$  is as shown in Figure 2.4.

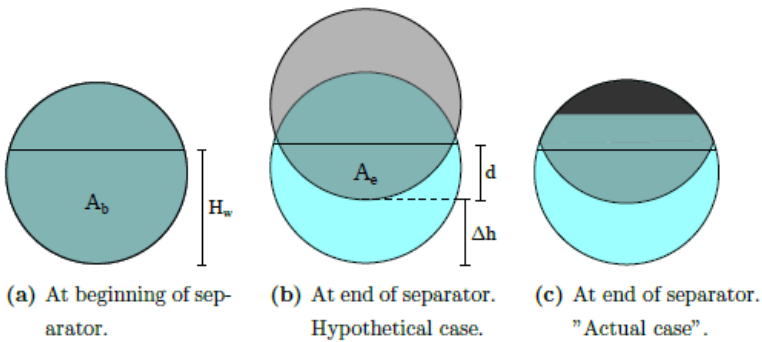


Figure 2.4: Cross section of gravity separator at the beginning and end of the gravity separator.

## 2.4 Results

The model of separation system was used to maximize the oil volume fraction in the overall light phase outlet  $q_{L,Prod}$  with a constraint of oil cut in final water-rich stream to be less than 3%. The optimizer found optimal flow splits of the three separators for several inlet oil cuts and inlet flow rates. The model for deoiler has been calibrated against experimental results from (van Campen, 2014). Figure

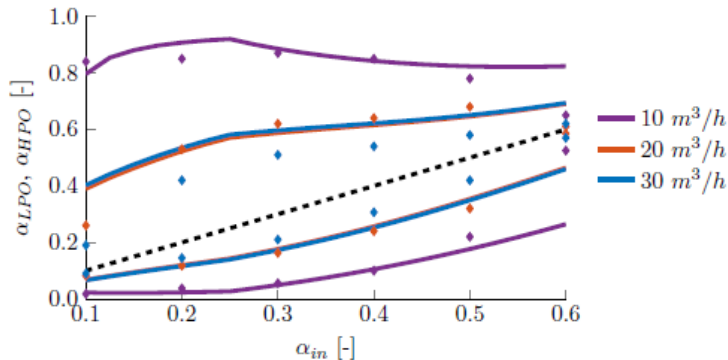


Figure 2.5: Oil volume fractions of the outlets vs inlets in a deoiler (experimental vs model results).

2.5 presents the comparison of the experimental results with the model results for different inlet oil volume fractions to the deoiler. The model was fitted for a throughput of  $10 \text{ m}^3/\text{h}$ . The model overpredicts the separation performance at higher throughput, and very low and very high inlet oil cuts possibly because of unaccounted effects of droplet break-up and droplet coalescence.

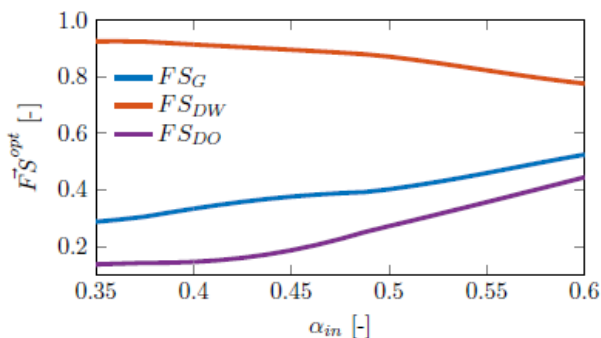


Figure 2.6: Optimal flow splits of separators vs inlet oil volume fraction ( $q_{in} = 20 \text{ m}^3/\text{h}$ ).

The optimization results in Figure 2.6 are as expected as the flow split for dewaterer falls and that for deoiler and gravity separator rise as inlet oil cut rises because

of higher oil load. Figure 2.7 shows optimal flow splits for changing throughput. The sign of the slope of optimal flow splits change around  $20 \text{ m}^3/h$  because both the deoiler and the dewaterer reach peak separation performance at  $8 \text{ m}^3/h$ .

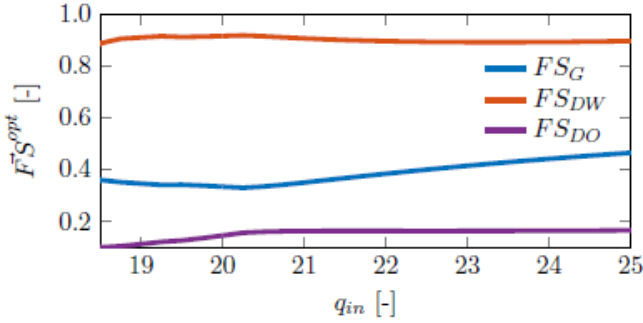


Figure 2.7: Optimal flow splits of separators vs inlet flow rate ( $\alpha_{in} = 0.4$ ).

## 2.5 Conclusions

The model for deoiler has been fitted to match data for oil concentrations  $\alpha_{in} \in [0.1 \text{ } 0.4]$  and for a throughput of  $10 \text{ m}^3/h$ . Hence, the model deviates from the experimental results close to the phase inversion point i.e. close to  $\alpha_{in} = 0.66$  and for high inlet flow rates. Further experimental work for lower oil cuts will help improve the model. The optimal flow splits have been found to be close to the oil cut in the inlet of the respective separators, as expected.

## Acknowledgements

We gratefully acknowledge good discussions with Sigurd Skogestad at the outset of this work.

## Part II

# Estimation results



## Chapter 3

# A model for subsea oil-water gravity separator to estimate unmeasured disturbances

In subsea oil and gas industry, sensors for process monitoring are often unavailable, unreliable or expensive. Hence, state and parameter estimation can be a viable alternative. In this work, we developed a simplified 6-state model for gravity separator (often used as a first stage separator in subsea separation systems) with lumped fluid properties. We used the model in an Extended Kalman Filter estimator using measurements of levels and densities of fluids inside the separator in order to estimate unmeasured disturbances, namely inlet total flow rate, inlet oil cut and inlet droplet diameter. Results show that the estimated disturbances converge to their true values when process changes.

*Published in Computer Aided Chemical Engineering. vol. 40, 2017.*

### 3.1 Introduction

For subsea oil and gas processing, accurate monitoring of subsea separation systems is quintessential because depending on water purity at separator outlet the water separated from the oil is either re-injected in a well, rejected in the sea or transported for downstream processing; each of which has its own limitation or capacity constraint. Gravity separators have been repeatedly used as bulk separators in subsea processing projects, including the first project Troll C ([Horn et al., 2003](#)). These separators are simple in design and efficient under rapidly changing inlet conditions and provide volume for slug handling.

([Arntzen, 2001](#)) reported that gravity separators have three layers: oil, emulsion and water. However, the latest dynamic model found in the literature is based on a principle of two layers, namely oil and water with a spatially shrinking emulsion volume in the middle ([Sayda and Taylor, 2007](#)). In this work, we develop an estimation oriented dynamic model of a gravity separator based on a three layer principle. We use this model inside an Extended Kalman Filter to estimate unmeasured disturbances and to filter the measured states. The filtered water level is

used in a feedback PI control law to determine manipulated variable  $u_{MV}$ , which is water outflow, in order to keep the water level at a predefined set point. The estimated input disturbances can be used for process monitoring, such as for adding chemicals for de-emulsification.

### 3.2 Process description

In a gravity separation process, a mixture of water and hydrocarbons consisting of gas and oil from upstream oil wells enters the separator. Most of the gas is flashed out instantaneously with minor traces remaining in the liquids at the outlet. The liquids separate along the length of the separator as they move towards the outlet as shown in Figure 3.1. Due to the difference in densities, they segregate into three layers: oil (top layer), emulsion (middle layer) and water (bottom layer). A weir is situated in between the water and oil outlets ensuring that only the oil layer flows over it, thereby the oil level is self-regulated. The oil is extracted from the outlet zone and is transported for downstream processing. The emulsion at the inlet is also the source of the emulsion layer below the oil. This layer can grow or shrink in thickness based on the extent of separation. The water layer is extracted from

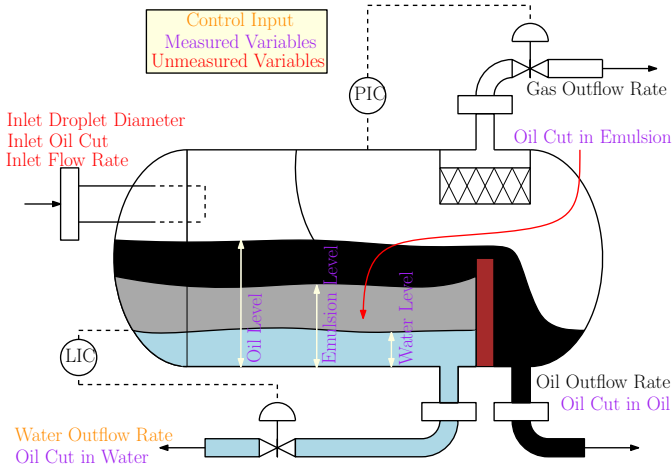


Figure 3.1: Schematic of gravity separation process.

the bottom of the separator in order to keep the water level constant, whereas the gas pressure is regulated using the gas outflow. For regulation purposes, the gas pressure and the three levels inside the separator are measured. The sensor technology for level measurement is often relying on density measurements along the height of the separator. Hence, densities along the separator height are also assumed measured. The inlet stream to the separator is dependent on upstream conditions, which include reservoir and well characteristics. When a new production well is commissioned, the liquids at the inlet consists of an oil rich emulsion with water droplets dispersed in an oil continuum. However, the oil cut (the volume fraction of oil in a mixture of oil and water) from a production well gradually

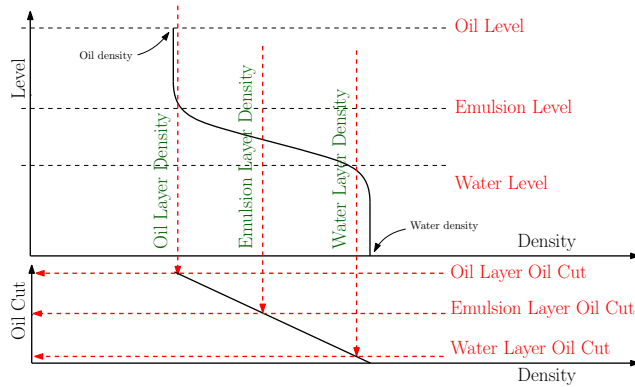


Figure 3.2: Relating density to oil cut.

drops as the reservoir ages, thereby causing an inversion of phases, which results in an emulsion with oil droplets dispersed in water continuum. The separation dynamics are affected by unmeasured disturbances, such as inlet flow rate, inlet oil cut and inlet droplet diameter of the dispersed phase. The oil cuts of the oil outlet and the water outlet are indicators of the separation performance of the gravity separator and can be easily estimated assuming a linear dependence between oil cut and density as shown in Figure 3.2.

### 3.3 Model description

The model has been constructed under the following assumptions: 1) We assume constant and uniform oil droplet size because we perceive that in continuous separation, sedimentation and droplet-interface coalescence happen so fast that effects of non uniform distributions can be neglected. 2) The inlet stream is a water in oil emulsion, which would under batch analysis develop two interfaces: A coalescing interface and a sedimenting interface as shown in Figure 3.3.

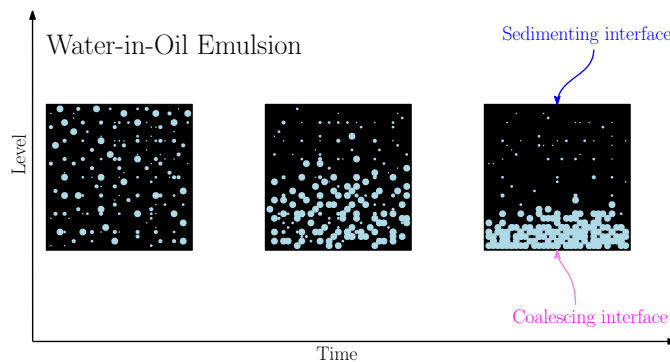


Figure 3.3: Batch analysis of water in oil emulsion.

We assume that the ideas of the two interfaces can be extended to continuous separation systems, such that the emulsion layer has two interfaces through which separation takes place. The model considers three bulk volumes of fluids one for each of the three layers denoted by  $V$  with a subscript (as shown in Figure 3.4). Each volume has its own bulk oil cut denoted by  $\epsilon$  with a subscript. The inlet flow  $F_{in}$  with oil fraction  $\epsilon_{in}$ , being an emulsion goes directly into the emulsion layer. The emulsion layer has the top interface as the sedimenting interface and the bottom interface as the coalescing interface. A pure stream of oil  $F_{up}$  goes up from the emulsion layer to the oil layer and a pure stream of water  $F_{down}$  goes down to the water layer. However, the oil layer and the water layer do not remain pure homogeneous layers because of the contaminations caused by turbulence and shear between the layers. This contamination is accounted for by the emulsion to oil reentrainment stream  $q_{up}$  and emulsion to water reentrainment stream  $q_{down}$ , which have been derived heuristically. The outlet streams include oil outflow over the weir  $F_{oil}$ , a possible emulsion outflow over the weir  $F_{emulsion}$  if the emulsion level rises higher than the weir height and the water outflow from the bottom  $F_{water}$ , which is used to control the water level. We used  $r$  and  $L$  as radius and length of the cylindrical gravity separator. For  $F_{up}$  we used the sedimentation equation and for  $F_{down}$  we used the coalescing equation presented in (Henschke et al., 2002).

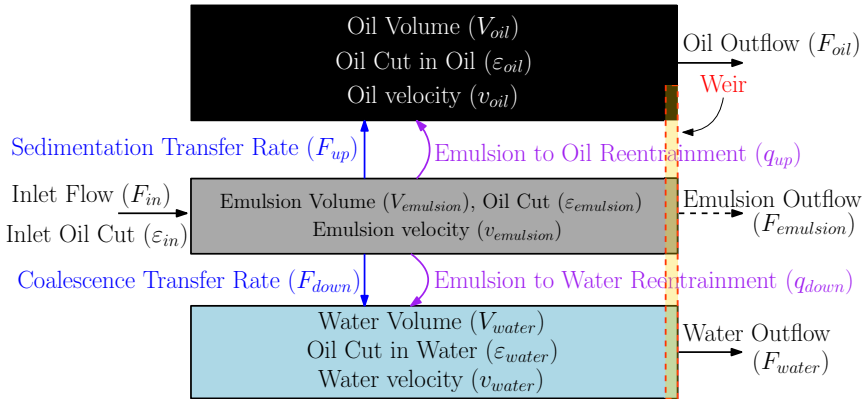


Figure 3.4: Flow streams and variables in the model.

The model was derived by assuming constant densities for pure oil and water phases. The differential equations for the top level of each layer from the separator bottom were derived by writing the rates of change of the respective volumes. These equations are in (3.1), (3.2) and (3.3). Similarly, the rates of change of the pure oil volume in each layer were written to derive the differential equations for the oil cut in each layer. These equations are in (3.4), (3.5) and (3.6). Here,  $h$  with a subscript denotes the respective layer level.  $A_c$  and  $A_t$  with a parenthesis denote cross-sectional area and transfer area, respectively corresponding to each layer level as shown in Figure 3.5.

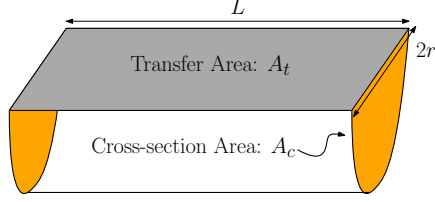


Figure 3.5: Area used in the model.

$$\frac{dh_{water}}{dt} = \frac{F_{down} + q_{down} - F_{water}}{2L\sqrt{2rh_{water} - h_{water}^2}} \quad (3.1)$$

$$\frac{dh_{emulsion}}{dt} = \frac{F_{in} - F_{up} - q_{up} - F_{water} - F_{emulsion}}{2L\sqrt{2rh_{emulsion} - h_{emulsion}^2}} \quad (3.2)$$

$$\frac{dh_{oil}}{dt} = \frac{F_{in} - F_{oil} - F_{emulsion} - F_{water}}{2L\sqrt{2rh_{oil} - h_{oil}^2}} \quad (3.3)$$

$$\frac{d\epsilon_{water}}{dt} = \frac{F_{down} + \epsilon_{emulsion}q_{down} - \epsilon_{water}F_{water} - \epsilon_{water}\frac{d}{dt}(V_{water})}{LA_c(h_{water})} \quad (3.4)$$

$$\frac{d\epsilon_{emulsion}}{dt} = \frac{\frac{d}{dt}(\epsilon_{emulsion}V_{emulsion}) - \epsilon_{emulsion}[\frac{d}{dt}(V_{emulsion} + V_{water}) - \frac{d}{dt}(V_{water})]}{L[A_c(h_{emulsion}) - A_c(h_{water})]} \quad (3.5)$$

$$\frac{d\epsilon_{oil}}{dt} = \frac{\frac{d}{dt}(\epsilon_{oil}V_{oil}) - \epsilon_{oil}[\frac{d}{dt}(V_{oil} + V_{emulsion} + V_{water}) - \frac{d}{dt}(V_{emulsion} + V_{water})]}{L[A_c(h_{oil}) - A_c(h_{emulsion})]} \quad (3.6)$$

Equations in (3.1), (3.2), (3.3), (3.4), (3.5) and (3.6) are the 6 state derivatives. The equations for transport terms  $q_{up}$  and  $q_{down}$  are as follows, where  $q_{up,para}$  and  $q_{down,para}$  are tuning parameters with unit [ $m^{-1}$ ].

$$q_{up} = q_{up,para} [A_{t,emulsion}v_{oil} (h_{emulsion} - h_{water})] \quad (3.7)$$

$$q_{down} = q_{down,para} [A_{t,water}v_{water} (h_{emulsion} - h_{water})] \quad (3.8)$$

The horizontal velocities of water stream  $v_{water}$  and of oil stream  $v_{oil}$  are:

$$v_{water} = \frac{F_{water}}{A_{c,water}}; v_{oil} = \frac{F_{oil}}{A_{c,oil} - \max(A_{c,emulsion}, A_{c,weir})} \quad (3.9)$$

The transport terms  $F_{down}$  and  $F_{up}$  are below, where  $F_{up,para}$  and  $F_{down,para}$  are tuning parameters. Inlet water droplet diameter is denoted by  $d$ , whereas  $t_{coalescence}$  represents droplet interface coalescence time for water droplets. 0.12 sec is chosen as  $t_{coalescence}$ , which if chosen incorrectly will be influenced by parameter  $F_{down,para}$ . The fluid properties are given by  $\mu_{oil}$ ,  $\rho_{oil}$  and  $\rho_{water}$  denoting oil viscosity, oil density and water density, respectively. For procedure to compute

the Reynold's number for sedimentation  $Re_s$  used in Equation (3.11), refer to (Henschke et al., 2002).

$$F_{down} = F_{down,para} \left[ \frac{2}{3} \frac{d}{t_{coalescence}} A_{t,water} \right] \quad (3.10)$$

$$F_{up} = F_{up,para} A_{t,emulsion} \frac{\mu_{oil} Re_s}{\rho_{oil} d} \quad (3.11)$$

$$F_{out} = \frac{2}{3} C_d l_{weir} \sqrt{2g} [\max(h_{oil} - h_{weir}, 0)]^{1.5} \quad (3.12)$$

$$F_{oil} = F_{out} \min \left( 1, \frac{(A_{c,oil} - A_{c,emulsion})}{(A_{c,oil} - A_{c,weir})} \right); F_{emulsion} = F_{out} - F_{oil} \quad (3.13)$$

The total outflow over weir  $F_{out}$  is given by the Bernoulli equation, with  $g$  as acceleration due to gravity and  $C_d$  as discharge constant chosen to be  $\frac{1}{\sqrt{3}}$ , which is a typical value for it.  $h_{weir}$  and  $l_{weir}$  are respectively, height and width of the weir. A possible emulsion flow over weir (if  $h_{emulsion} > h_{weir}$ ) is given by  $F_{emulsion}$ , whereas oil flow  $F_{oil}$  is scaled by respective areas. The model can be written as  $\dot{x} = f(x, u_{MV}, u_{DV}, p)$ ;  $y = Hx$ , with  $\dot{x}$  as state derivatives vector,  $x = [h_{water}, h_{emulsion}, h_{oil}, \varepsilon_{water}, \varepsilon_{emulsion}, \varepsilon_{oil}]^T$  as state vector,  $u_{MV} = F_{water}$  as control input,  $p = [q_{up,para}, q_{down,para}, F_{up,para}, F_{down,para}]^T$  as parameters,  $u_{DV} = [F_{in}, \varepsilon_{in}, d]^T$  as disturbances and  $y = x$  as measurement vector i.e.  $H = I_{6 \times 6}$ .

### 3.4 Estimator

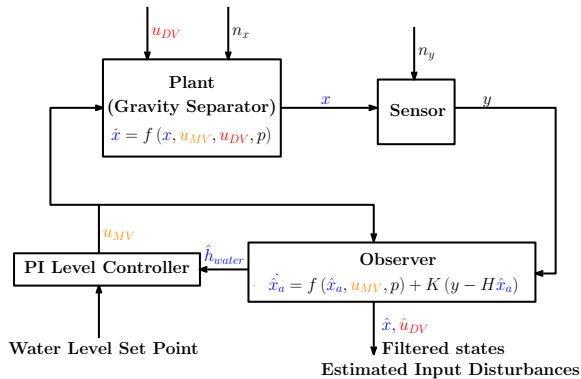


Figure 3.6: Control structure;  $K$  is Kalman gain and superscript  $\hat{\cdot}$  indicates estimated signals.

A continuous Extended Kalman Filter was designed based on the gravity separator model to estimate the unmeasured input disturbance vector  $u_{DV}$  and parameter vector  $p$ . For that purpose, the state vector was augmented to  $x_a = [x^T, u_{DV}^T]^T$ , with zero derivatives for the disturbance vector ( $\dot{u}_{DV} = 0$ ) considered in the corresponding function  $f_a$ , such that the augmented state derivatives are  $\dot{x}_a = f_a(x_a, u_{MV}, p)$ .

The observability matrix for the pair  $\left(\frac{\partial f_a}{\partial x_a}, H\right)$  evaluated at the operating points had full rank. The measurements contain measurement noise  $n_y$  i.e.  $y = x + n_y$  and the process is susceptible to unknown process noise  $n_x$ , i.e.  $\dot{x} = f(x, u_{MV}, u_{DV}, p) + n_x$ . It is assumed that these noises are zero mean Gaussian noises i.e.  $n_x \sim \mathcal{N}(0, Q_p)$  and  $n_y \sim \mathcal{N}(0, R)$ , where  $Q_p = 10^{-4} \times I_{6 \times 6}$  and  $R = 10^{-4} \times I_{6 \times 6}$ . The observer presented in Figure 3.6 filters out the noise from the measurements and provides estimates for the input disturbances. Apart from the noises, gross changes are imposed on the disturbances to examine estimator robustness.

### 3.5 Results and discussion

Table 3.1: Simulation parameters

$l_{weir}$	$h_{weir}$	$L$	$r$	$\rho_{water}$	$\rho_{oil}$	$\mu_{water}$	$\mu_{oil}$
3.46 m	3 m	10 m	2 m	1000 kg/m <sup>3</sup>	845 kg/m <sup>3</sup>	0.55 mPa.s	1.3 mPa.s

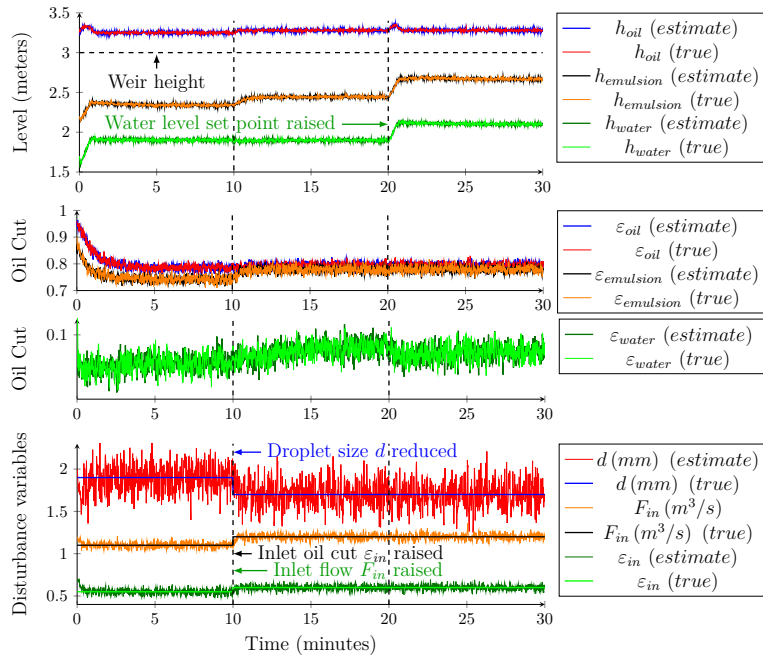


Figure 3.7: True and estimated states and disturbances.

Table 3.1 shows simulation parameters. For the estimator, we chose covariance matrix  $Q = 10^{-4} \times \text{diag}([1, 1, 1, 1, 1, 1, 10, 10, 250])$  and covariance matrix  $R = 10^{-4} \times I_{6 \times 6}$ . The PI controller was chosen of the form  $P + I/s$  with  $P = 4.196$  and  $I = 4.196/160$ . The water level estimate was filtered by a low pass filter with transfer function  $1/(5s + 1)$  before being fed into the PI controller.

The simulations were conducted in MATLAB Simulink using fixed step solver ode3 with  $\hat{x}_{a,0} = [1.7, 2.2, 3.3, 0.2, 0.9, 0.96, 1.2, 0.7, 2]^T$  as initial estimator state,  $p = [0.04, 0.03, 1.2, 0.8]^T$  as parameter vector, water level set point 1.9 *m* and  $x_0 = [1.56, 2.12, 3.22, 0.07, 0.87, 0.95]^T$  as initial plant state. The results in Figure 3.7 indicate that the unmeasured disturbances initiated with poor guesses are able to track their true values within one minute. At 10 mins, droplet size, inlet oil cut and inlet flow are changed from 1.9 to 1.7 *mm*, 0.55 to 0.60 and 1.1 to 1.2 *m*<sup>3</sup>/*s*, respectively; these changes were readily tracked by the estimator. These changes also affected the separation performance adversely, leading to a thicker emulsion layer, a poorer water quality, a slightly raised oil content in the oil layer and a change in the steady state. At 20 min, the water level set point was raised from 1.9 to 2.1 *m*, which resulted in a slightly improved water quality due to an increase in the residence time in the water layer.

## 3.6 Conclusion

We developed a gravity separator model with four tuning parameters, which could be estimated offline or online. The model was used for estimation of variables at the separator inlet. We reckon the heuristically derived equations (3.7) and (3.8) need further investigation.

## Acknowledgements

We acknowledge the financial support from SUBPRO, a Research-based Innovation Centre within Subsea production and processing.

## Chapter 4

# Pathfollowing approach for a sensitivity based moving horizon estimator

In moving horizon estimation (MHE), a computationally expensive nonlinear program (NLP) is solved at each sampling time to determine the current state of the system. To overcome the computational challenges, an advanced-step MHE (asMHE) framework has been proposed in the literature. asMHE consists of a computationally expensive offline part and a fast NLP sensitivity based online part. We propose a predictor-corrector pathfollowing method for the online part within asMHE. In this method, we solve a few quadratic programs sequentially in order to follow the optimal solution of the NLP for tracking a parameter change, which is the difference between a predicted measurement value and the real measurement value corresponding to the latest sample. This allows it to track the active set changes as they occur. To demonstrate the method, we performed simulations on a gas phase three component batch reaction model. We compare the solutions from the ideal-MHE and the pathfollowing based MHE. The results indicate that the pathfollowing based MHE is able to effectively trace the exact solution and the changes in active set in an efficient manner.

*Published in Proceedings for IEEE 56th Annual Conference on Decision and Control (CDC), 2017*

### 4.1 Introduction

In moving horizon estimation (MHE), estimates for states and parameters are found by minimizing an objective function, which is a summation of weighted least squares of process noises and measurement noises in a horizon consisting of several measurement samples from immediate past, subject to model equations, output equations and constraints. When a new measurement arrives, the new sample is included in the horizon while the oldest sample is discarded. Thus, the horizon keeps moving one sampling time forward with each sample, thereby limiting the computational expense. This optimization problem is discretized into a nonlinear program (NLP) if the model equations are nonlinear.

Although MHE has evolved in the past decade as a useful tool for estimation in constrained nonlinear systems, its large computational expense and the cost associated with model development have deterred its application for online estimation in large scale systems. Even for a relatively short horizon with few states, the optimization problem can take a non-negligible amount of time to solve. A delayed estimate leads to a delayed control action, which can deteriorate the closed loop performance and potentially lead to instability (Findeisen and Allgöwer, 2004). Two approaches have been developed in the literature to address the issue of computational burden associated with MHE problems. Both approaches include an offline phase (preparation phase) and an online phase (estimation phase).

The first approach is known as the real time iteration (RTI) scheme (Kühl et al., 2011). In RTI, the idea is to limit the computational expense of solving the NLP to one sequential quadratic programming (SQP) iteration i.e. one quadratic program (QP), which results in an efficient approximate solution. The preparation phase carries out the linearizations necessary to set up the Newton step for the KKT system, while the estimation phase embeds the final measurement as it arrives and computes the step to update the solution from the previous time step. Note that here the full NLP is never solved. In RTI, the gap between the approximate solution and the optimal solution can be narrowed by a better initial guess at each sample time by a procedure called warm-starting.

The other approach to handle computational expense of the MHE problem is to use the advanced step MHE (asMHE) (Zavala et al., 2008), wherein the full NLP is solved to a given optimality tolerance in the offline part, using a predicted value for the upcoming measurement in order to obtain an approximate solution. This solution is referred as *predicted solution* and the corresponding problem *predicted NLP*. In the online part, the predicted solution is updated using the measurement (as it arrives) and the optimal sensitivity of the predicted solution to a change in the final measurement.

In comparison to other estimation techniques, MHE offers a distinct advantage in terms of the ability to handle inequality constraints. This is especially important for applications in which the variables of interest tend to be very close to the bounds. Such applications include high purity separation processes, such as distillation or reactors in which one or more species is completely consumed. In the RTI scheme, handling of inequality constraints is natural due to its adoption of QPs as a tool to solve the optimization problems. In asMHE, however, changes in the active set (set of active inequality constraints) cause a change in the dimension of the KKT matrix. The KKT matrix structure is consequently changed in the online part by applying Schur complement techniques to the factorized KKT matrix obtained from the offline part (Zavala et al., 2008), which is somewhat heuristic. A rigorous approach to handle active set changes was presented within advanced step model predictive control framework in (Jäschke et al., 2014) and (Suwartadi et al., 2017), where the authors presented a pathfollowing based sensitivity update.

Inspired by (Jäschke et al., 2014) and (Suwartadi et al., 2017), we propose the pathfollowing advanced step MHE (pasMHE), in which we use a predictor-corrector pathfollowing method to compute a change of the predicted NLP solution in the online part. In our pathfollowing method, a series of QPs are solved to trace the NLP solution for a change in parameter, i.e. such that the latest measurement in

predicted NLP is corrected for the real measurement value.

The main contribution of this paper is to present a fast MHE method that ensures that the solution can effectively track the changes in active set as they occur while adapting the final measurement variable in the online part. This is achieved by including strongly active inequality constraints as equality constraints and weakly active ones as inequality constraints in the pathfollowing QPs.

This paper is structured in the following way. In section 4.2, we formulate the MHE problem. In section 4.3, we present the sensitivity properties of the associated NLP. In section 4.4, we discuss pathfollowing approaches for NLP. We present pathfollowing advanced step MHE algorithm in section 4.5. In section 4.6, the proposed algorithm is applied to a state estimation case study, for which the results can be found in section 4.7. We conclude the paper with a discussion and final remarks in section 4.8.

## 4.2 Moving horizon estimation problem formulation

### 4.2.1 A general Moving Horizon Estimation framework

We consider NLP formulation (4.1) for MHE with discrete time dynamics spanning a horizon length of  $N$  finite elements, such that at time instant  $i$ ,  $x_i$  and  $y_i$  represent the state and the output, respectively and  $u_i$  represents piecewise constant input between time instants  $i$  and  $i + 1$ .  $f: \mathbb{R}^{n_x} \times \mathbb{R}^{n_u} \rightarrow \mathbb{R}^{n_x}$  represents discretized state dynamics, whereas  $h: \mathbb{R}^{n_x} \rightarrow \mathbb{R}^{n_y}$  represents state to output mapping. The MHE objective function spans over two time segments:  $t_{past} = \{i \mid 0 \leq i < k - N\}$  and  $t_{horizon} = \{i \mid k - N \leq i \leq k\}$ , where  $k$  represents the current time step and the horizon consists of latest  $N + 1$  measurement samples. The contribution to the objective function from  $t_{past}$  is summarized in the arrival cost, whereas that from  $t_{horizon}$  in the stage costs.

$$\begin{aligned}
 & \underbrace{\{\hat{x}_{k-N|k}, \hat{v}_{k-N|k}, \hat{w}_{k-N|k}, \dots, \hat{w}_{k-1|k}, \hat{x}_{k|k}, \hat{v}_{k|k}\}}_{\text{Stage costs}} = \\
 & \arg \min_{\{X_{k-N}^k, V_{k-N}^k, W_{k-N}^{k-1}\}} \underbrace{\left[ \sum_{i=k-N}^{k-1} w_i^T Q^{-1} w_i + \sum_{i=k-N}^k v_i^T R^{-1} v_i \right]}_{\text{Arrival cost}} \\
 & + \underbrace{\|x_{k-N} - \hat{x}_{k-N|k-1}\|_{\Pi_{k-N|k-1}^{-1}}^2 - \|\mathcal{Y} - \mathcal{O}x_{k-N}\|_{\mathcal{W}^{-1}}^2}_{\text{Arrival cost}} \\
 & \text{s.t. } x_{i+1} = f(x_i, u_i) + w_i \\
 & \quad y_i = h(x_i) + v_i \\
 & \quad x_{lb} \leq x_i \leq x_{ub}
 \end{aligned} \tag{4.1}$$

We consider additive Gaussian noises denoted by  $w_i \sim \mathcal{N}(0, Q)$  for process noise and  $v_i \sim \mathcal{N}(0, R)$  for measurement noise. The decision variables in (4.1) are the sequence of states  $X_{k-N}^k = \{x_{k-N}, \dots, x_k\}$ , process noises  $W_{k-N}^{k-1} = \{w_{k-N}, \dots, w_{k-1}\}$  and measurement noises  $V_{k-N}^k = \{v_{k-N}, \dots, v_k\}$  in  $t_{horizon}$  denoted by  $\{X_{k-N}^k, V_{k-N}^k, W_{k-N}^{k-1}\}$ .

The smoothed and filtered estimates of the states and the noises in  $t_{horizon}$  conditioned on measurement data from  $t_{horizon}$  are obtained by solving the optimization problem (4.1) and are denoted as  $\{\hat{x}_{k-N|k}, \hat{v}_{k-N|k}, \hat{w}_{k-N|k}, \dots, \hat{w}_{k-1|k}, \hat{x}_{k|k}, \hat{v}_{k|k}\}$ , where,  $\hat{x}_{k|k}$  represents the state estimate of  $x_k$  given all the measurement information until time point  $k$ . Bound constraints on the states are included in the optimization problem as inequality constraints, whereas the discretized model equations and output equations appear as equality constraints. The lower and upper bounds on the states are denoted by  $x_{lb}$  and  $x_{ub}$ , respectively. Note that in (4.1) the weighted 2-norm  $\|z\|_Z^2$  expands as  $z^T Z z$ .

We consider a smoothed arrival cost approximation in our NLP formulation (4.1) for MHE (Lopez Negrete de la Fuente, 2011), assuming a normally distributed probability density function for  $x_{k-N|k-1} \sim \mathcal{N}(\hat{x}_{k-N|k-1}, \Pi_{k-N|k-1})$ . In the arrival cost, the first term represents a penalty on the deviation of the first state  $x_{k-N}$  from the smoothed estimate  $\hat{x}_{k-N|k-1}$  obtained from the NLP solved at time instant  $k-1$ . The covariance matrix  $\Pi_{k-N|k-1}$  is extracted from the reduced Hessian of the Lagrangian of the NLP for time instant  $k-1$  as in (López-Negrete and Biegler, 2012). The second term in the arrival cost is a correction to the first term, such that the measurement data  $Y_{k-N}^{k-1}$  are not counted twice in the arrival cost.

Matrices  $\mathcal{Y}, \mathcal{O}$  and  $\mathcal{W}$  used in (4.1) are below (López-Negrete and Biegler, 2012), where  $H$  denotes  $\frac{\partial h}{\partial x}$ ,  $J$  denotes the Jacobian of the state derivatives with respect to states and  $\omega$  and  $v$  represent respectively the estimates of process and measurement noises obtained from the previous horizon MHE problem.

$$\begin{aligned}
 \mathcal{Y} &= \mathcal{O} x_{k-N|k-1} + \mathcal{M} \omega + v \\
 \mathcal{W} &= \mathcal{O} \Pi_{k-N|k-1} \mathcal{O}^T + \mathcal{M} \mathcal{Q} \mathcal{M}^T + \mathcal{R} \\
 \mathcal{O} &= \begin{bmatrix} H_{k-N} \\ H_{k-N+1} J_{k-N} \\ \vdots \\ H_{k-1} J_{k-2} J_{k-3} \cdots J_{k-N} \end{bmatrix}; \quad \omega = \begin{bmatrix} w_{k-N} \\ \vdots \\ w_{k-1} \end{bmatrix}; \quad v = \begin{bmatrix} v_{k-N} \\ \vdots \\ v_{k-1} \end{bmatrix} \\
 \mathcal{M} &= \begin{bmatrix} 0 & 0 & 0 & 0 \\ H_{k-N+1} & H_{k-N+2} & 0 & 0 \\ \vdots & \vdots & \ddots & \vdots \\ H_{k-1} J_{k-2} J_{k-3} \cdots J_{k-N+1} & H_{k-1} J_{k-2} J_{k-3} \cdots J_{k-N+2} & \cdots & H_{k-1} \end{bmatrix} \\
 \mathcal{Q} &= \underbrace{diag(Q, \dots, Q)}_{N-1 \text{ times}}; \quad \mathcal{R} = \underbrace{diag(R, \dots, R)}_{N \text{ times}}
 \end{aligned}$$

#### 4.2.2 Ideal Moving Horizon Estimation

Ideal moving horizon estimation (ideal MHE) are MHE problems that are solved at each sampling times  $k$  with the measurement sequence and arrival cost updated at each sampling time. As soon as the new measurement arrives, the NLP is assumed to be solved with no time delay.

### 4.2.3 Advanced step Moving Horizon Estimation framework

In reality, the MHE problem is impossible to be solved with no time delay. To reduce the time delay between receiving the new measurement value and having the new state available, the advanced step moving horizon estimation (asMHE) was proposed (Zavala et al., 2008). It involves the following two steps:

1. Offline step: In this step, the MHE is solved based on a prediction of the newest measurement, rendering an approximate solution together with the corresponding NLP sensitivity of the solution to a change in the parameter i.e. the final measurement.
2. Online step: In this step, the approximate solution from the offline step is updated (or corrected) using the real measurement and the NLP sensitivity.

## 4.3 Sensitivity in parametric nonlinear programming

The MHE problems solved in the offline step can be framed as a parametric NLP as follows:

$$\begin{aligned} & \min_{\mathbf{X}} F(\mathbf{X}) \\ & \text{s.t. } C(\mathbf{X}, \mathbf{p}) = 0 \\ & \quad G(\mathbf{X}, \mathbf{p}) \leq 0 \end{aligned} \tag{4.2}$$

Here,  $\mathbf{X} \in \mathbb{R}^{n_x}$  is a vector of decision variables (primal variables) containing state sequence and the process and measurement noise sequences in the horizon window.  $\mathbf{p} \in \mathbb{R}^{n_y}$  is a parameter vector corresponding to the final measurement.  $F: \mathbb{R}^{n_x} \rightarrow \mathbb{R}$  is the scalar objective function,  $C: \mathbb{R}^{n_x} \times \mathbb{R}^{n_y} \rightarrow \mathbb{R}^{n_c}$  denotes the equality constraints corresponding to the model equations and  $G: \mathbb{R}^{n_x} \times \mathbb{R}^{n_y} \rightarrow \mathbb{R}^{n_g}$  denotes the inequality constraints corresponding to the constraints on states.

The Lagrangian function of (4.2) is defined below, where  $\boldsymbol{\lambda}$  and  $\boldsymbol{\mu}$  represent the vectors of Lagrange multipliers (dual variables) for equality constraints and inequality constraints, respectively.

$$\mathcal{L}(\mathbf{X}, \mathbf{p}, \boldsymbol{\lambda}, \boldsymbol{\mu}) = F(\mathbf{X}) + \boldsymbol{\lambda}^T C(\mathbf{X}, \mathbf{p}) + \boldsymbol{\mu}^T G(\mathbf{X}, \mathbf{p})$$

The Karush-Kuhn-Tucker (KKT) conditions for (4.2) are:

$$\begin{aligned} \nabla_{\mathbf{X}} \mathcal{L}(\mathbf{X}, \mathbf{p}, \boldsymbol{\lambda}, \boldsymbol{\mu}) &= 0 \\ C(\mathbf{X}, \mathbf{p}) &= 0 \\ G(\mathbf{X}, \mathbf{p}) &\leq 0 \\ \boldsymbol{\mu}^T G(\mathbf{X}, \mathbf{p}) &= 0 \\ \boldsymbol{\mu} &\geq 0 \end{aligned} \tag{4.3}$$

A point  $(\mathbf{X}^*, \boldsymbol{\lambda}^*, \boldsymbol{\mu}^*)$  that satisfies (4.3) for a given parameter vector  $\mathbf{p}^*$  is called a KKT point.

**Definition 4.1.** (*Active set*) For problem (4.2) at a KKT point  $\mathbf{X}$  and parameter vector  $\mathbf{p}$ , the *active set*  $\mathbb{A}$  refers to the set  $\{j \in (1, \dots, n_g) \mid G_j(\mathbf{X}, \mathbf{p}) = 0\}$ ,

and the corresponding vector of active constraints denoted by  $G_{\mathbb{A}}(\mathbf{X}, \mathbf{p})$  is given by  $\{G_j(\mathbf{X}, \mathbf{p}) \mid j \in \mathbb{A}\}$ . The complement of set  $\mathbb{A}$  is *inactive set*  $\mathbb{A}^-$ , where  $\mathbb{A}^- = \{j \in (1, \dots, n_G) \mid G_j(\mathbf{X}, \mathbf{p}) < 0\}$ .

**Definition 4.2.** (Strongly active set) The *strongly active set* is a subset of set  $\mathbb{A}$  given by  $\mathbb{K}_+ = \{j \in \mathbb{A} \mid \mu_j > 0\}$  and the corresponding vector of active constraints in set  $\mathbb{K}_+$  is denoted by  $G_{\mathbb{K}_+}(\mathbf{X}, \mathbf{p})$ . The *weakly active set* is a subset of set  $\mathbb{A}$  given by  $\mathbb{K}_W = \{j \in \mathbb{A} \mid \mu_j = 0\}$ . Set  $\mathbb{K}_0$  is given by  $\mathbb{K}_0 = \mathbb{A}^- \cup \mathbb{K}_W$ . The corresponding vector of inequality constraints in the index set  $\mathbb{K}_0$  is denoted by  $G_{\mathbb{K}_0}(\mathbf{X}, \mathbf{p})$ .

**Definition 4.3.** (LICQ) For a parameter vector  $\mathbf{p}$  and vector  $\mathbf{X}$ , the *linear independence constraint qualification* holds if the vectors in  $\{\{\nabla_{\mathbf{X}} C_i(\mathbf{X}, \mathbf{p})\}_{i \in \{1, \dots, n_C\}} \cup \{\nabla_{\mathbf{X}} G_i(\mathbf{X}, \mathbf{p})\}_{i \in \mathbb{A}}\}$  are linearly independent.

LICQ warrants that the Lagrange multipliers  $\boldsymbol{\lambda}$  and  $\boldsymbol{\mu}$  corresponding to a KKT point are unique.

**Definition 4.4.** (SSOSC) The *strong second order sufficient condition* holds at a KKT point  $(\mathbf{X}^*, \boldsymbol{\lambda}^*, \boldsymbol{\mu}^*)$  for all non-zero directions  $d$  if  $d^T \nabla_{\mathbf{X}\mathbf{X}}^2 \mathcal{L}(\mathbf{X}^*, \mathbf{p}^*, \boldsymbol{\lambda}^*, \boldsymbol{\mu}^*) d > 0$  such that  $\nabla_{\mathbf{X}} G_{\mathbb{K}_+}(\mathbf{X}^*, \mathbf{p}^*)^T d = 0$  and  $\nabla_{\mathbf{X}} C(\mathbf{X}^*, \mathbf{p}^*)^T d = 0$ .

In conjunction with LICQ, SSOSC guarantees that a KKT point is a unique local minimum.

**Definition 4.5.** (SC) *Strict complementarity* holds if for a given parameter vector  $\mathbf{p}^*$  the KKT point  $(\mathbf{X}^*, \boldsymbol{\lambda}^*, \boldsymbol{\mu}^*)$  satisfies  $\boldsymbol{\mu}_i^* - G_i(\mathbf{X}^*, \mathbf{p}) > 0$  for each  $i = 1, \dots, n_G$ .

**Theorem 4.1.** *Let  $\mathbf{X}^*$  satisfy KKT conditions (4.3) for a given parameter vector  $\mathbf{p}_0$ , and LICQ, SSOSC, and SC hold at  $\mathbf{X}^*(\mathbf{p}_0)$ . Further, let  $F, C$ , and  $G$  be  $k + 1$  times differentiable in  $\mathbf{X}$  and  $k$  times differentiable in  $\mathbf{p}$ . Then*

- $\mathbf{X}^*$  is an isolated minimizer and its corresponding Lagrange multipliers  $\boldsymbol{\lambda}^*$  and  $\boldsymbol{\mu}^*$  are unique.
- For  $\mathbf{p}$  in the neighborhood of  $\mathbf{p}_0$ , the set  $\mathbb{A}$  does not change.
- There exists a  $k$  times differentiable function  $\sigma(\mathbf{p}) = [\mathbf{X}^*(\mathbf{p})^T \ \boldsymbol{\lambda}^*(\mathbf{p})^T \ \boldsymbol{\mu}^*(\mathbf{p})^T]^T$  of  $\mathbf{p}$  in the neighborhood of  $\mathbf{p}_0$ , where  $\sigma(\mathbf{p})$  corresponds to a unique local minimum for (2).

*Proof.* Refer to Fiacco (Fiacco, 1983). □

Based on this result, we can compute the sensitivities  $\nabla_{\mathbf{p}} \mathbf{X}$ ,  $\nabla_{\mathbf{p}} \boldsymbol{\lambda}$ ,  $\nabla_{\mathbf{p}} \boldsymbol{\mu}$  of the optimal solution  $\mathbf{X}^*$ ,  $\boldsymbol{\lambda}^*$ ,  $\boldsymbol{\mu}^*$  to changes in the parameter vector  $\mathbf{p}$  by solving the system of linear equations resulting from the application of the implicit function theorem to KKT conditions (4.3):

$$K \begin{bmatrix} \nabla_{\mathbf{p}} \mathbf{X} \\ \nabla_{\mathbf{p}} \boldsymbol{\lambda} \\ \nabla_{\mathbf{p}} \boldsymbol{\mu} \end{bmatrix} = - \begin{bmatrix} \nabla_{\mathbf{p}\mathbf{X}}^2 \mathcal{L}(\mathbf{X}^*, \mathbf{p}_0, \boldsymbol{\lambda}^*, \boldsymbol{\mu}^*) \\ \nabla_{\mathbf{p}} C(\mathbf{X}^*, \mathbf{p}_0) \\ \nabla_{\mathbf{p}} G_{\mathbb{A}}(\mathbf{X}^*, \mathbf{p}_0) \end{bmatrix} \quad (4.4)$$

where

$$K = \begin{bmatrix} \nabla_{\mathbf{X}\mathbf{X}}^2 \mathcal{L}(\mathbf{X}^*, \mathbf{p}_0, \lambda^*, \mu^*) & \nabla_{\mathbf{X}} C(\mathbf{X}^*, \mathbf{p}_0) & \nabla_{\mathbf{X}} G_{\mathbb{A}}(\mathbf{X}^*, \mathbf{p}_0) \\ \nabla_{\mathbf{X}} C(\mathbf{X}^*, \mathbf{p}_0)^T & 0 & 0 \\ \nabla_{\mathbf{X}} G_{\mathbb{A}}(\mathbf{X}^*, \mathbf{p}_0)^T & 0 & 0 \end{bmatrix} \quad (4.5)$$

Using the optimal solution and the sensitivities computed in (4.4), the solution manifold in the neighborhood of  $\mathbf{p}_0$  can be estimated using the following equations.

$$\begin{bmatrix} \mathbf{X}(\mathbf{p}_0 + \Delta \mathbf{p}) \\ \lambda(\mathbf{p}_0 + \Delta \mathbf{p}) \\ \mu(\mathbf{p}_0 + \Delta \mathbf{p}) \end{bmatrix} = \begin{bmatrix} \mathbf{X}^*(\mathbf{p}_0) \\ \lambda^*(\mathbf{p}_0) \\ \mu^*(\mathbf{p}_0) \end{bmatrix} + \begin{bmatrix} \nabla_{\mathbf{p}} \mathbf{X} \\ \nabla_{\mathbf{p}} \lambda \\ \nabla_{\mathbf{p}} \mu \end{bmatrix} \Delta \mathbf{p} \quad (4.6)$$

Within the advanced step MHE framework (Zavala et al., 2008), the online step executes the above mentioned sensitivity update, wherein the upcoming measurement is treated as parameter, making the MHE problem (4.1) a parametric NLP (4.2).

Note that if SC does not hold at  $\mathbf{p}_0$ , above mentioned sensitivity updates by solving (4.4) will not follow the optimal solution manifold as a step  $\Delta \mathbf{p}$  can induce changes in set  $\mathbb{A}$ . Hence, we propose pathfollowing as an alternative, in which we take multiple smaller steps that are fractions of  $\Delta \mathbf{p}$  using quadratic programs. This ensures closer tracking of the optimal solution.

#### 4.4 Sensitivity using pathfollowing

In the more general case where SC does not hold the NLP sensitivity can be obtained from a quadratic program (QP) that gives the change in solution vector  $\Delta \mathbf{X}$  given a change in the parameter vector  $\Delta \mathbf{p}$ .

**Theorem 4.2.** *Let LICQ and SSOSC hold at point  $\mathbf{X}^*(\mathbf{p}_0)$  for a parameter vector  $\mathbf{p}_0$ . Let  $F, C$ , and  $G$  be twice continuously differentiable both in  $\mathbf{X}$  and  $\mathbf{p}$  near point  $(\mathbf{X}^*, \mathbf{p}_0)$ . Then*

- *The solution function  $(\mathbf{X}^*(\mathbf{p}), \lambda^*(\mathbf{p}), \mu^*(\mathbf{p}))$  is Lipschitz continuous in the neighborhood of  $(\mathbf{X}^*, \mathbf{p}_0, \lambda^*, \mu^*)$ .*
- *The directional derivative of solution path  $(\mathbf{X}^*(\mathbf{p}), \lambda^*(\mathbf{p}), \mu^*(\mathbf{p}))$  exists and is uniquely given by the solution of the following QP.*

$$\begin{aligned} \min_{\Delta \mathbf{X}} \quad & \frac{1}{2} \Delta \mathbf{X}^T \nabla_{\mathbf{X}\mathbf{X}}^2 \mathcal{L}(\mathbf{X}^*, \mathbf{p}_0, \lambda^*, \mu^*) \Delta \mathbf{X} \\ & + \Delta \mathbf{p}^T \nabla_{\mathbf{p}\mathbf{X}}^2 \mathcal{L}(\mathbf{X}^*, \mathbf{p}_0, \lambda^*, \mu^*) \Delta \mathbf{X} \\ \text{s.t.} \quad & \nabla_{\mathbf{X}} C(\mathbf{X}^*, \mathbf{p}_0)^T \Delta \mathbf{X} + \nabla_{\mathbf{p}} C(\mathbf{X}^*, \mathbf{p}_0)^T \Delta \mathbf{p} = 0 \\ & \nabla_{\mathbf{X}} G_{\mathbb{K}_+}(\mathbf{X}^*, \mathbf{p}_0)^T \Delta \mathbf{X} + \nabla_{\mathbf{p}} G_{\mathbb{K}_+}(\mathbf{X}^*, \mathbf{p}_0)^T \Delta \mathbf{p} = 0 \\ & \nabla_{\mathbf{X}} G_{\mathbb{K}_W}(\mathbf{X}^*, \mathbf{p}_0)^T \Delta \mathbf{X} + \nabla_{\mathbf{p}} G_{\mathbb{K}_W}(\mathbf{X}^*, \mathbf{p}_0)^T \Delta \mathbf{p} \leq 0 \end{aligned} \quad (4.7)$$

*Proof.* Refer to (Jittorntrum, 1984). □

**Remark 4.1.** The solution of QP (4.7) is a solution step  $\Delta \mathbf{X}$  for a given parameter change  $\Delta \mathbf{p}$  in the tangential direction at point  $\mathbf{X}^*(\mathbf{p}_0)$ . The step  $\Delta \mathbf{X}$  is a predictor step. To this end, the QP (4.7) is referred as pure-predictor QP (Jäschke et al., 2014). The KKT conditions for QP (4.7) under limit  $\Delta \mathbf{p} \rightarrow 0$  leads to (4.4), whenever SC holds.

**Remark 4.2.** Since a QP allows inequality constraints in problem definition, QP (4.7) provides the flexibility of closely tracking the correct solution manifold under changes in the set  $\mathbb{A}$  induced by large parameter perturbations. This property is absent in (4.4) and (4.6).

Iteratively applying a pure-predictor pathfollowing QP resembles an Euler scheme of integration. To further improve the approximation accuracy, we can include some corrector elements in the optimization problem as shown in e.g. (Kungurtsev and Diehl, 2014). Formulating (4.2) as a QP by linearizing the constraints at point  $(\mathbf{X}^*, \mathbf{p}_0, \lambda^*, \mu^*)$  leads to several terms in the objective function of the QP vanishing as the parameter  $\mathbf{p}$  enters linearly into the constraints of (4.2), leaving us with (4.8). Here, note that we retain the classification of inequality constraints in sets  $\mathbb{K}_+$  and  $\mathbb{K}_0$ .

$$\begin{aligned}
 \min_{\Delta \mathbf{X}} \quad & \frac{1}{2} \Delta \mathbf{X}^T \nabla_{\mathbf{X}\mathbf{X}}^2 \mathcal{L}(\mathbf{X}^*, \mathbf{p}_0, \lambda^*, \mu^*) \Delta \mathbf{X} + \nabla_{\mathbf{X}} F(\mathbf{X}^*)^T \Delta \mathbf{X} \\
 \text{s.t.} \quad & \nabla_{\mathbf{p}} C(\mathbf{X}^*, \mathbf{p}_0) \Delta \mathbf{p} + \nabla_{\mathbf{X}} C(\mathbf{X}^*, \mathbf{p}_0)^T \Delta \mathbf{X} = 0 \\
 & \nabla_{\mathbf{p}} G_{\mathbb{K}_+}(\mathbf{X}^*, \mathbf{p}_0) \Delta \mathbf{p} + \nabla_{\mathbf{X}} G_{\mathbb{K}_+}(\mathbf{X}^*, \mathbf{p}_0)^T \Delta \mathbf{X} = 0 \\
 & G_{\mathbb{K}_0}(\mathbf{X}^*, \mathbf{p}_0) + \nabla_{\mathbf{p}} G_{\mathbb{K}_0}(\mathbf{X}^*, \mathbf{p}_0) \Delta \mathbf{p} + \nabla_{\mathbf{X}} G_{\mathbb{K}_0}(\mathbf{X}^*, \mathbf{p}_0)^T \Delta \mathbf{X} \leq 0
 \end{aligned} \tag{4.8}$$

Since the parameter  $\mathbf{p}$  enters the constraints in (4.2) linearly,  $\nabla_{\mathbf{p}} C(\mathbf{X}^*, \mathbf{p}_0) \Delta \mathbf{p}$  can be replaced by  $C(\mathbf{X}^*, \mathbf{p}_f) - C(\mathbf{X}^*, \mathbf{p}_0)$ , where  $C(\mathbf{X}^*, \mathbf{p}_0) = 0$ . Similar substitutions can be made for  $\nabla_{\mathbf{p}} G_{\mathbb{K}_+}(\mathbf{X}^*, \mathbf{p}_0) \Delta \mathbf{p}$  and  $\nabla_{\mathbf{p}} G_{\mathbb{K}_0}(\mathbf{X}^*, \mathbf{p}_0) \Delta \mathbf{p}$  to arrive at formulation (4.9). Here, note that  $\nabla_{\mathbf{X}}$  or  $\nabla_{\mathbf{X}\mathbf{X}}^2$  terms are free of parameter  $\mathbf{p}$ , which means we can replace  $\mathbf{p}_0$  with  $\mathbf{p}_f$  without any change.

$$\begin{aligned}
 \min_{\Delta \mathbf{X}} \quad & \frac{1}{2} \Delta \mathbf{X}^T \nabla_{\mathbf{X}\mathbf{X}}^2 \mathcal{L}(\mathbf{X}^*, \mathbf{p}_f, \lambda^*, \mu^*) \Delta \mathbf{X} + \nabla_{\mathbf{X}} F(\mathbf{X}^*)^T \Delta \mathbf{X} \\
 \text{s.t.} \quad & C(\mathbf{X}^*, \mathbf{p}_f) + \nabla_{\mathbf{X}} C(\mathbf{X}^*, \mathbf{p}_f)^T \Delta \mathbf{X} = 0 \\
 & G_{\mathbb{K}_+}(\mathbf{X}^*, \mathbf{p}_f) + \nabla_{\mathbf{X}} G_{\mathbb{K}_+}(\mathbf{X}^*, \mathbf{p}_f)^T \Delta \mathbf{X} = 0 \\
 & G_{\mathbb{K}_0}(\mathbf{X}^*, \mathbf{p}_f) + \nabla_{\mathbf{X}} G_{\mathbb{K}_0}(\mathbf{X}^*, \mathbf{p}_f)^T \Delta \mathbf{X} \leq 0
 \end{aligned} \tag{4.9}$$

We call problem (4.9) predictor-corrector QP. However, we can give an alternative form of (4.9) in which  $\Delta \mathbf{p}$  appears in the formulation and we enforce it to be equal to some value  $\epsilon$ . This is necessary if we do not want to take a full step  $(\mathbf{p}_f - \mathbf{p}_0)$ , instead multiple smaller steps  $\epsilon = (\mathbf{p}_f - \mathbf{p}_0) / m$ , where  $(m - 1) \in \mathbb{N}$  and

iteratively update the solution.

$$\begin{aligned}
 & \min_{\Delta \mathbf{X}} \frac{1}{2} \Delta \mathbf{X}^T \nabla_{\mathbf{X}\mathbf{X}}^2 \mathcal{L}(\mathbf{X}^*, \mathbf{p}_0 + \Delta \mathbf{p}, \boldsymbol{\lambda}^*, \boldsymbol{\mu}^*) \Delta \mathbf{X} + \nabla_{\mathbf{X}} F(\mathbf{X}^*)^T \Delta \mathbf{X} \\
 & \text{s.t. } \quad C(\mathbf{X}^*, \mathbf{p}_0 + \Delta \mathbf{p}) + \nabla_{\mathbf{X}} C(\mathbf{X}^*, \mathbf{p}_0 + \Delta \mathbf{p})^T \Delta \mathbf{X} = 0 \\
 & \quad G_{\mathbb{K}_+}(\mathbf{X}^*, \mathbf{p}_0 + \Delta \mathbf{p}) + \nabla_{\mathbf{X}} G_{\mathbb{K}_+}(\mathbf{X}^*, \mathbf{p}_0 + \Delta \mathbf{p})^T \Delta \mathbf{X} = 0 \\
 & \quad G_{\mathbb{K}_0}(\mathbf{X}^*, \mathbf{p}_0 + \Delta \mathbf{p}) + \nabla_{\mathbf{X}} G_{\mathbb{K}_0}(\mathbf{X}^*, \mathbf{p}_0 + \Delta \mathbf{p})^T \Delta \mathbf{X} \leq 0
 \end{aligned} \tag{4.10}$$

## 4.5 Pathfollowing advanced step moving horizon estimation

Based on the developments above, we propose the pathfollowing advanced step MHE (pasMHE) algorithm in Algorithm 1, which includes both the offline and the online parts. We start with the solution from the predicted NLP  $\mathbf{X}^*(\mathbf{p}_0)$  as the initial point for the pathfollowing algorithm. To initiate the pathfollowing algorithm, we provide the number of steps  $m$  and the real final measurement  $y_k$ , which is used to compute the parameter step length  $\epsilon$ , as shown in Algorithm 1, where  $N$  represents the number of finite elements. (4.10) is solved  $m$  times and after each solution, the pathfollowing solution is updated by adding the optimal change  $\Delta \mathbf{X}$  to the previous solution. Likewise, the initial parameter  $\mathbf{p}_0$  and the Lagrange multipliers are updated. Note that the Lagrange multipliers of (4.10) are approximations of the NLP Lagrange multipliers themselves and not their change.

---

### Algorithm 1: pasMHE algorithm

---

**input** : Initiate the estimator with  $\mathbf{X}^*(\mathbf{p}_0)$ ,  $m$  and  $y_k$   
**output**: State estimate  $\hat{x}_{k|k}^{pf}$  and  $\Pi_{k|k}^{pf}$  for each  $k$

- 1 **while**  $k \geq N$  **do**
- 2     **Offline**: solve predicted NLP
- 3      $\mathbf{p}_0 \leftarrow$  predicted measurement
- 4      $\mathbf{X}^{pf}(\mathbf{p}_0) \leftarrow$  predicted NLP solution  $\mathbf{X}^*(\mathbf{p}_0)$
- 5      $\mathbf{p}_f \leftarrow y_k$  as measurement  $y_k$  becomes available
- 6      $\Delta \mathbf{p} \leftarrow (\mathbf{p}_f - \mathbf{p}_0) / m$
- 7      $\epsilon \leftarrow \Delta \mathbf{p}$
- 8     **for**  $i \leftarrow 1$  **to**  $m$  **do**
- 9         **Online**: solve (10) using  $\Delta \mathbf{p}$  to get  $\Delta \mathbf{X}$
- 10          $\mathbf{X}^{pf}(\mathbf{p}_0 + \Delta \mathbf{p}) \leftarrow \mathbf{X}^{pf}(\mathbf{p}_0) + \Delta \mathbf{X}$
- 11          $\boldsymbol{\lambda}(\mathbf{p}_0 + \Delta \mathbf{p}) \leftarrow$  Lagrange multiplier of (10)
- 12          $\boldsymbol{\mu}(\mathbf{p}_0 + \Delta \mathbf{p}) \leftarrow$  Lagrange multiplier of (10)
- 13          $\mathbf{p}_0 \leftarrow \mathbf{p}_0 + \Delta \mathbf{p}$
- 14     **end**
- 15      $\hat{x}_{k|k}^{pf} \leftarrow \mathbf{X}^{pf}(\mathbf{p}_f)$  pathfollowing solution
- 16      $\Pi_{k|k}^{pf} \leftarrow$  Extracted reduced Hessian at  $\mathbf{X}^{pf}(\mathbf{p}_f)$
- 17 **end**

---

**Remark 4.3.** In the pasMHE algorithm, if the QP is infeasible,  $\epsilon$  should be reduced until it becomes feasible again. After every QP solution in pathfollowing, the algorithm checks for active set changes by monitoring the Lagrange multipliers. If an active set change is observed, sets  $\mathbb{K}_+$  and  $\mathbb{K}_0$  are updated in the next QP.

## 4.6 Case study

We consider a batch reaction system in gas phase with three components given by  $i \in \{A, B, C\}$  undergoing the following two reactions, where  $k_j, j \in \{1, 2, 3, 4\}$  denotes reaction rate constant (Haseltine and Rawlings, 2005).



The stoichiometry matrix  $\nu$  and reaction rate matrix  $r$  for (4.11) are as follows:

$$\nu = \begin{bmatrix} -1 & 1 & 1 \\ 0 & -2 & 1 \end{bmatrix}, \quad r = \begin{bmatrix} k_1 c_A - k_2 c_B c_C \\ k_3 c_B^2 - k_4 c_C \end{bmatrix} \quad (4.12)$$

The state vector  $c$  is a vector of concentrations (in *Molar*) of the components  $c_i$  such that  $c = [c_A \ c_B \ c_C]^T$ . We consider pressure in the reaction vessel as the only measurement given by  $P = (\sum c_i) R_g T$ , where pressure is in *bar*,  $R_g = 0.08314 \frac{\text{bar}}{\text{Molar.K}}$  is the universal gas constant and  $T$  denotes reaction temperature in the vessel in *K*. The pressure sensor has a standard deviation of 0.1 *bar*. Hence, the measurement noise covariance is  $R = 0.01$ . Further, we assume that the reaction temperature is controlled at 400 *K*. The reaction rate constants  $k_j$  used in the simulation are given below:

$k_1$	$k_2$	$k_3$	$k_4$
0.5	0.05	0.2	0.01

The model equations are  $\frac{dc}{dt} = \nu^T r$  with  $c_i \geq 0$ , since concentrations cannot be negative. The process noise affects the states directly such that in the plant model we have  $\frac{dc}{dt} = \nu^T r + w$ , where  $w$  is zero mean Gaussian random noise of the form  $w \sim \mathcal{N}([0 \ 0 \ 0]^T, 10^{-4} \times [2.5 \ 1 \ 1]^T)$ , hence, the process noise covariance matrix is  $Q = 10^{-4} \times [2.5 \ 1 \ 1]^T$ .

The plant simulations were performed in MATLAB Simulink using a fixed step solver ode3 with a step size of 0.1 *min* and initial condition  $[0.5 \ 0.05 \ 0]^T$  to generate the data for true states and the pressure measurement. The pressure measurement data were used within the estimator to estimate the three states. For the estimator, an initial estimate of  $x_{0|0} = [0.7 \ 0.5 \ 0.1]^T$  with an initial estimate error covariance  $\Pi_{0|0} = 10^{-3} \times \text{diag}([10 \ 2.5 \ 1])$  was provided. The moving horizon estimator was set up considering 5 measurements in the horizon. The MHE was formulated as a NLP by discretizing the continuous time dynamics using direct collocation method. The discretization was performed using an algorithmic differentiation tool CasADi (version 3.0.0) (Andersson et al., 2012). The formulated NLPs for predicted MHE and the ideal MHE were solved using interior point solver IPOPT (Wächter and Biegler, 2006). For pasMHE, we chose  $m = 2$  and used the MATLAB QP solver quadprog.

Note that in our MHE problems, we consider that the start up phase includes increasing horizon full information estimation (FIE) problems as described in Figure 4.1. Hence, the first horizon in the start up phase includes only two measurements. The correction terms in the arrival cost were only implemented in the post start up phase. We also implemented a continuous-discrete Extended Kalman Filter (EKF) (Simon, 2006) to see if it gives infeasible estimates.

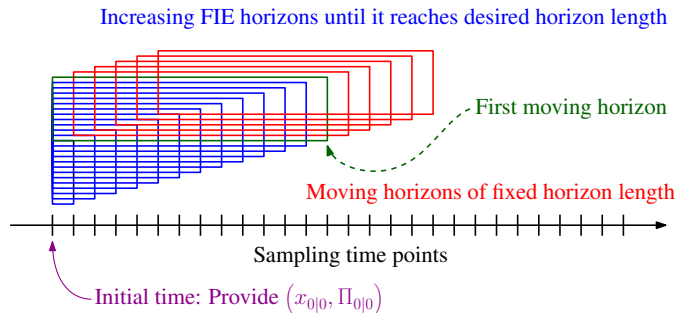


Figure 4.1: MHE initialization with increasing horizon FIE problems ( $x_{0|0}$  is the initial estimate and  $\Pi_{0|0}$  is the initial estimate error covariance matrix).

## 4.7 Results

### 4.7.1 Results from Ideal MHE, predicted MHE and EKF

Firstly, we compare the state estimates obtained from the ideal MHE and EKF to the true values of the three states in the figure below.

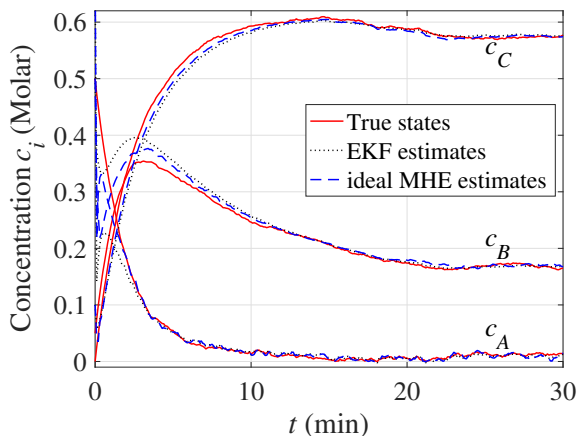


Figure 4.2: True states, EKF estimates and ideal MHE estimates.

We notice that the rapidly changing concentrations are tracked reasonably well by estimators. We obtained a sum of squared error (SSE) between the estimated

states and the true states of 0.5795 for the ideal MHE estimates, of 0.7367 for the predicted MHE estimates and of 1.1957 for EKF estimates. While using the EKF, we obtained infeasible estimates for  $c_A$  at the following time points.

Time (min)	17.9	18.0	18.1	21.2	22.5
$c_A$ (Molar)	-0.0004	-0.0008	-0.0024	-0.0024	-0.0001

### 4.7.2 Results from pasMHE

Here, we compare the pasMHE estimates to the ideal MHE estimates because pasMHE is proposed as an alternative to the ideal MHE problem. We computed the SSE between the ideal MHE estimates and the pasMHE estimates, which was  $6.6743 \times 10^{-7}$  for 300 sample points. Hence, we conclude that pasMHE is a suitable alternative to the ideal MHE because pasMHE solution closely tracks the ideal MHE solution.

Lastly, the pasMHE method was proposed to show that this method can accurately track the active set changes happening in the ideal MHE solution. We noticed that in the ideal MHE solution, the estimate  $c_A$  was active (i.e. equal to 0) at the following time points in minutes: {15.2, 17.9, 18.0, 18.1, 21.1, 21.2}. Hence, in Figure 4.3 we show the error between the pasMHE solution and the ideal MHE solution obtained for  $c_A$  for the sample times between 15 and 22 minutes. We notice fairly small errors, hence, active set changes are also very closely tracked by the pasMHE solution. We further notice that at points where  $c_A \geq 0$  is active, the error is non-negative, indicating that pasMHE solution is not violating the constraints.

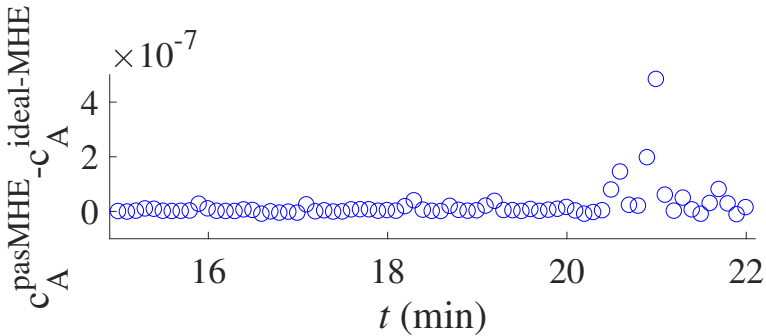


Figure 4.3: Error between pasMHE solution and ideal MHE solution for  $c_A$ .

## 4.8 Conclusion and discussion

In this paper, we presented a predictor-corrector based pathfollowing approach within advanced step moving horizon estimation framework. The key motivation is to track the solution of the original NLP as closely as possible by making the strongly active constraints as equality constraints and weakly active constraints as inequality constraints. This procedure ensures that the changes in active set within the online part of the algorithm are tracked accurately, which is important for

applications, such as distillation and reaction systems, in which estimated variables tend to be very close to their bounds.

pasMHE and RTI based MHE (RTI-MHE) (Kühl et al., 2011) are similar methods because both solve QPs, however, the real difference between them is two fold. Firstly, pasMHE solves full NLP, whereas RTI does not. Secondly, in pasMHE, the strongly active constraints and the weakly active constraints are treated differently, ensuring that the QPs solved are always strongly convex even if the Hessian of the Lagrangian is not positive definite. This property, which warrants fast convergence at a minor overhead of identifying active constraints outside QP, is missing in reported RTI schemes. The effect of not enforcing strongly active constraints has been demonstrated in Section 3.3 in (Suwartadi et al., 2017). In NLP for MHE problems, nonlinear constraints arising from the model can potentially make the Hessian of the Lagrangian indefinite.

Computationally, pasMHE is more costly than RTI-MHE because the NLP is solved at each sample time. However, as long as the NLP can be solved in between two samples, the computational delay will be the time needed to solve the pathfollowing problems, which typically are a few QP iterations.

## Acknowledgements

We acknowledge the financial support from SUBPRO, a Research-based Innovation Centre within Subsea production and processing.



## Part III

# Models for control of separators and separation system



## Chapter 5

# Modeling and control of an inline deoiling hydrocyclone

In subsea oil and gas production and processing, automatic control of operation is of significant importance. Typically, processing in subsea fields involves separation of hydrocarbons from water and rejection of water in an environmentally friendly way. Separators such as deoiling hydrocyclones help achieve these objectives. However, control strategy for hydrocyclones is not yet well established in the literature due to a lack of control oriented models for hydrocyclone. In this work we present a model for hydrocyclone based on mass balance equations. Subsequently, we propose a PI controller for controlling the water quality.

*Published in Proceedings for the 3rd IFAC Automatic Control in Offshore Oil and Gas Production (OOGP) conference, 2018*

### 5.1 Introduction

In oil and gas processing fields, to reduce the oil content in the produced water a common separation system is used, which caters to streams from various wells. The separation system usually consists of bulk separators, such as first and second stage separators and high purity separators, such as hydrocyclone and compact flotation unit (Ruud et al., 2015). The bulk separators perform a crude separation of oil from the produced water. However, the water from these separators is not suitable for discharge in the sea because the oil content in this water is much higher than that allowed for discharge in the sea. Permissible emission limits on water discharge are in the range of 20 – 30 *ppm* oil in water (OSPAR, 2001). Hence, in order to further reduce the oil content, the produced water is processed in hydrocyclones. The inline hydrocyclones (HC) employ cyclonic forces to achieve g-forces much higher than gravity by virtue of a swirl element in the flow direction close to the feed. Typically, hydrocyclones bring down the oil content in water to a range of 100 – 200 *ppm*, which is further reduced to a range of 20 – 30 *ppm* using a compact flotation unit.

The emission limits on discharged water has reinforced the need for automatic control of HC operation. Automatic control of processes requires dynamic models.

In the literature for HC modeling, first principles based models have attracted less focus in comparison to data driven approaches (Durdevic et al., 2015). However, it has been reported that data driven models often fail to cover a wide range of operating conditions (Durdevic et al., 2017). In real operating fields, HCs can be subjected to a wide variety of feeds with different inlet water qualities, especially in oil and gas fields in which a common separation system handles a network of wells and tie-in wells.

In this work we focus on developing a control oriented first principles based model for a deoiling inline hydrocyclone in order to alleviate some of the challenges faced by data driven models. An inline deoiling HC is shown in Figure 5.1, in which all the flows are co-current.

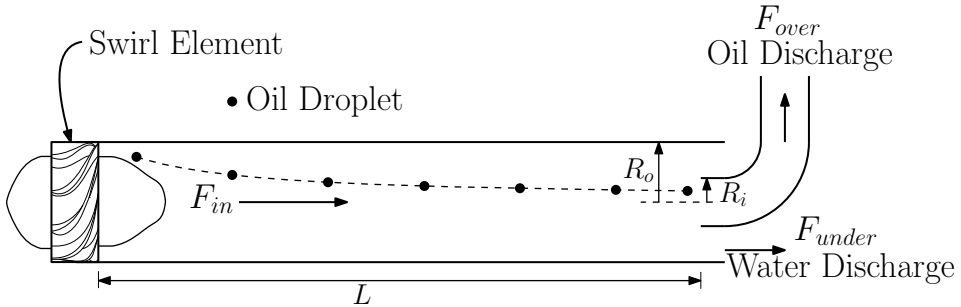


Figure 5.1: Schematic of an inline deoiling Hydrocyclone.

The inflow  $F_{in}$  containing oil and water enters the separator and passes a swirl element. The separated water is removed in the underflow  $F_{under}$ , and the oily concentrate is taken out in the overflow  $F_{over}$ . We derive our dynamic model based on mass balance for oil droplets. We extend the previously developed steady state model by (Das et al., 2016) to include dynamic behavior. In our model, the separation of the oil droplets is governed by the radial and axial velocities. We calculate the oil cut in  $F_{under}$  based on a spatial profile of the oil droplets in the separator. This spatial profile changes temporally under transient conditions.

In this work, we use the dynamic model as plant to propose a control loop from Oil in Water in processed water flow  $F_{under}$  to oily discharge flow  $F_{over}$ . The rest of the paper is organized in the following way: In section 5.2, we describe the process. Section 5.3 presents the model equations. Section 5.4 describes the details of the controller used to control water quality. Results are presented in the section 5.5. The paper is concluded in the section 5.6.

## 5.2 Process Description

In inline hydrocyclones, swirl elements are used to create cyclonic effects. A typical swirl element is shown in Figure 5.2. The swirling effect is a function of the angle of the blades  $\theta$ . This element is placed at the start of the hydrocyclone near feed as shown in Figure 5.1. This puts the flow in a swirl motion, which lets the fluids have an angular velocity as well as an axial velocity. Along the length of the separator

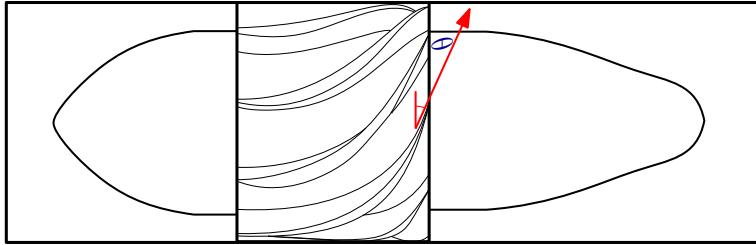


Figure 5.2: Swirl element (Adapted from (van Campen, 2014)).

towards the outlet the swirl decays. The density difference between oil and water propels dispersed oil droplets radially towards the center of the separator as the fluids move axially to the exit (shown in Figure 5.1).

### 5.3 HC modeling

We model the HC assuming that the overflow  $F_{over}$ , the inlet total flow  $F_{in}$  and inlet oil cut  $\epsilon_{in}$  are known. Because of the cyclonic forces and different axial flows in the two coaxial sections, the oil droplets have specific radial and axial velocities, which are functions of their size, their radial and axial positions inside the separator and the total flow rate. The droplets are assumed to immediately achieve terminal velocities in the radial direction. These velocities have a very spatially local validity, hence it is necessary to solve for the hydrodynamics in a spatial way.

It is assumed that based on the design given by radii  $R_i$  and  $R_o$ , the separator volume is segmented into two volumes, one inner cylindrical and one outer annular. The flows  $F_{over}$  and  $F_{under}$  flow in the inner and the outer volumes, respectively. Droplets, under the influence of the cyclonic forces, will travel radially inwards towards the center. The droplets crossing the common interface between these two volumes are going to switch from one outlet to the other. The cyclonic force is proportional to the square of the droplet size, hence the larger the droplets, the higher the possibility of them exiting in the oily discharge. The cyclonic effect produced by the swirl element is proportional to the  $F_{in}$ , however, this effect also causes droplets to break leading to several smaller droplets. Hence, the overall effect of increasing  $F_{in}$  on the achieved separation is given by a trade-off between the effects mentioned earlier.

For the model, some equations have been written as partial differential equations (PDE), which are discretized in radial and axial directions to obtain a series of ordinary differential equations. Other model equations have been written directly for the discretized control volumes as presented below.

#### 5.3.1 Model equations (PDEs)

The coordinate system used for developing the model is shown in Figure 5.3. The  $r$ -coordinate starts at the center of the separator and ends at the separator wall i.e.  $r = R_o$ .

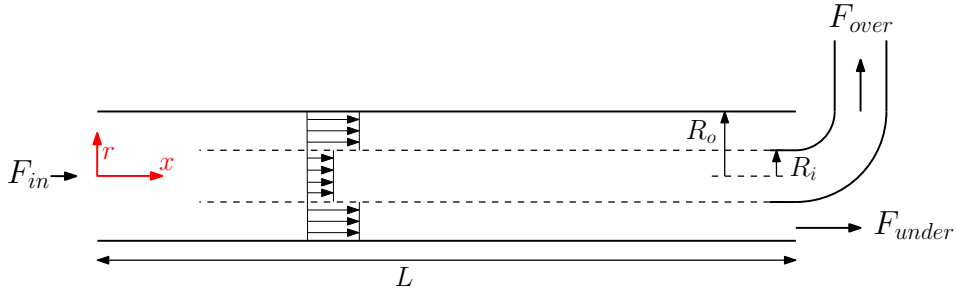


Figure 5.3: Coordinate system and axial velocity profiles.

The velocity of oil droplets in radial direction is denoted by  $v_r^d$  and in the axial direction is denoted by  $v_x^d$ . The axial velocity  $v_x^d$  is presented below as a function of  $r$ .

$$v_x^d(r) = \begin{cases} \frac{F_{over}}{\pi R_i^2} & \text{for } 0 \leq r \leq R_i \\ \frac{F_{under}}{\pi (R_o^2 - R_i^2)} & \text{for } R_i < r \leq R_o \end{cases} \quad (5.1)$$

The swirl number  $\Omega$  is associated with the swirling effect the swirl element will produce.  $\Omega$  is dependent on the  $\theta$  in Figure 5.2. Values of  $\Omega$  are between 2.5 and 7.5. We simulated our model for  $\Omega = 2.5$ , however other values could also be used. Here, we denote the maximum possible tangential velocity  $v_\theta^{max}$  as a function of  $\Omega$  and the bulk axial velocity  $v_{x,b}$ .

$$v_\theta^{max} = \Omega v_{x,b} \quad (5.2)$$

$$v_{x,b} = \frac{F_{in}}{\pi R_o^2} \quad (5.3)$$

The tangential velocities near  $x = 0$  i.e. just downstream of the swirl element are dependent on the radial position as given below. The assumption of this velocity profile has been taken from (Tyvold, 2015). Here,  $R_c$  is the radius of the inner core with a solid body rotation.  $R_c/R_o$  is set to 0.25.

$$v_\theta^0(r) = \begin{cases} \frac{v_\theta^{max} r}{R_c} & \text{for } 0 \leq r \leq R_c \\ v_\theta^{max} & \text{for } R_c < r \leq R_o \end{cases} \quad (5.4)$$

However, we expect the swirling effect to decline in strength along the length of the separator. Hence, the tangential velocity  $v_\theta$  shall decay exponentially with an exponent of  $C_{decay}$  along the length of the separator, thereby leading to the following steady state solution, as presented in (Najafi et al., 2011; Slot, 2013).

$$v_\theta(r, x) = v_\theta^0(r) \exp\left(-\frac{C_{decay} x}{2R_o}\right) \quad (5.5)$$

The above equation is empirical in nature. A possible unsteady extension of (5.5) is below, though this equation needs experimental validation.

$$\frac{\partial v_\theta}{\partial t} + v_x \frac{\partial v_\theta}{\partial x} = -\frac{C_{decay}}{2R_o} v_\theta v_x \quad (5.6)$$

Here, (5.4) acts as the boundary condition for (5.6). The tangential velocity is going to give rise to a radial acceleration  $g_r$ , which is derived using centripetal acceleration. This radial acceleration can be used to derive the expression for local radial terminal velocity  $v_r$  the droplets will achieve. The expression comes from application of Stokes' law<sup>1</sup>.

$$g_r(r, x) = \frac{(v_\theta(r, x))^2}{r} \quad (5.7)$$

$$v_r^d(r, x, d_d) = \frac{g_r(r, x) d_d^2 (\rho_w - \rho_o)}{18\mu_w} \quad (5.8)$$

Here,  $\rho_w$ ,  $\rho_o$  and  $\mu_w$  denote water density, oil density and water viscosity. The droplet diameter  $d_d$  is a function of the maximum possible tangential velocity  $v_\theta^{max}$  as given below, which (Tyvold, 2015) provided using experimental data points found in (van Campen, 2014).

$$d_d(v_\theta^{max}) [\mu m] = \begin{cases} (600 - 107v_\theta^{max}) & \text{for } 0 \leq v_\theta^{max} \leq 4.45 \\ (160 - 8v_\theta^{max}) & \text{for } 4.45 < v_\theta^{max} \leq 20 \end{cases} \quad (5.9)$$

Since,  $v_\theta^{max}$  is a function of the inflow  $F_{in}$ ,  $F_{in}$  affects the droplet size and thereby also affects the  $v_r^d$ . Since, the model is spatial in nature, we do not expect the droplets throughout the separator to change size immediately when the flow changes. Hence, we consider a partial differential equation for the transit of droplet sizes through the separator.

$$\frac{\partial d_d}{\partial t} + v_x \frac{\partial d_d}{\partial x} = 0 \quad (5.10)$$

(5.10) shall result in the same evolution of average droplet diameter along the length of the separator as if solved for using population balances of different droplet classes, albeit with a much simpler equation. Here, (5.9) acts as boundary condition for (5.10) at  $x = 0$ .

### 5.3.2 Discretization and equations for discretized volumes

In order to solve the model, we chose to discretize the separator volume in several control volumes. We consider  $n_x = 12$  equally discretized volumes in the axial

<sup>1</sup>For the nominal inflow into the hydrocyclone considered in this work, the droplet sizes computed using (5.9) are fairly high. This leads to violation of the Stokes' drag law and invalidity of (5.8), which requires the droplet Reynold's number to be below 1. Nonetheless, we used (5.8) as we did not have an alternative relation; this is common practice in literature (van Campen, 2014). For a specific application, the criterion of droplet Reynold's number below 1 needs to be verified before using (5.8).

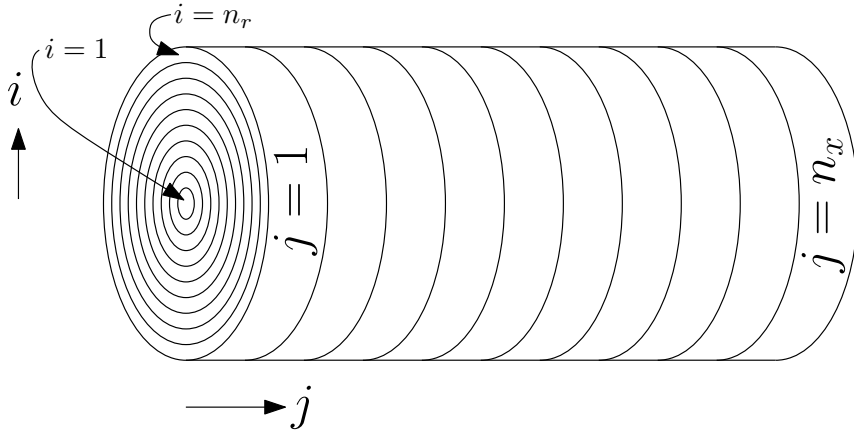


Figure 5.4: Discretizations.

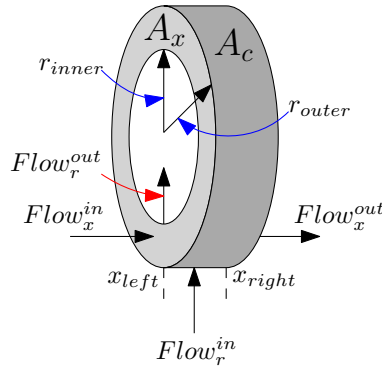


Figure 5.5: Schematic of a single control volume.

direction. Each of this axially discretized volume is further discretized into  $n_r = 12$  radial discretizations, with each control volume having the same volume. This resulted in a total of 144 control volumes as shown in Figure 5.4, where  $j$  denotes index in  $x$  direction and  $i$  denotes index in  $r$  direction starting from  $r = 0$  and ending at  $r = R_o$ . Figure 5.5 shows one such ring element with the corresponding notation. Based on the control volume denoted by  $(i, j)$ , the radial and axial boundaries of the control volumes are calculated as below.

$$r_{inner} = R_o \sqrt{\frac{i-1}{n_r}} \quad (5.11)$$

$$r_{outer} = R_o \sqrt{\frac{i}{n_r}} \quad (5.12)$$

$$x_{left}(i) = (j-1) \frac{L}{n_x} \quad (5.13)$$

$$x_{right}(i) = \frac{L}{n_x} j \quad (5.14)$$

Equations (5.6) and (5.10) have been discretized using the finite volume method assuming  $d_d$  and  $v_\theta$  are piecewise constant in each control volume. Further, it is assumed that the oil volume fractions are piecewise constant in each control volume. The droplets enter from the left boundary ( $x_{left}$ ) and the radially outer boundary ( $r_{outer}$ ) and leave from the right boundary ( $x_{right}$ ) and the radially inner boundary ( $r_{inner}$ ) as shown in Figure 5.5. The balance on oil volume for an arbitrary control volume ( $i, j$ ) is written in the discretized form as below (We do not provide partial differential equations for these ones).

$$\underbrace{\frac{d}{dt} (\epsilon_d A_x \Delta x)}_{\text{Accumulation}} = \underbrace{(A_c v_r^d \epsilon_d)|_{r_{outer}}}_{\text{Flow}_r^{in}} - \underbrace{(A_c v_r^d \epsilon_d)|_{r_{inner}}}_{\text{Flow}_r^{out}} + \underbrace{(A_x v_x^d \epsilon_d)|_{x_{left}}}_{\text{Flow}_x^{in}} - \underbrace{(A_x v_x^d \epsilon_d)|_{x_{right}}}_{\text{Flow}_x^{out}} \quad (5.15)$$

Here,  $\epsilon_d$  represents the local volume fraction of oil.  $A_x$  and  $A_c$  are shown in Figure 5.5, where  $A_x$  denotes the annular area of each control volume, given by  $\pi R_o^2/n_r$  (All control volumes have same  $A_x$  as per discretization) and  $A_c$  the curved area given by  $A_c(r) = 2\pi r \Delta x$ , where  $\Delta x = L/n_x$ . Since the control volume doesn't change size, we can rearrange equation (5.15) to get the following equation.

$$\frac{d\epsilon_d}{dt} = \frac{(A_c v_r^d \epsilon_d)|_{r_{outer}} - (A_c v_r^d \epsilon_d)|_{r_{inner}}}{A_x \Delta x} + \frac{(v_x^d \epsilon_d)|_{x_{left}} - (v_x^d n \epsilon_d)|_{x_{right}}}{\Delta x} \quad (5.16)$$

The boundary conditions for the  $x$  coordinate are related to the inlet conditions and therefore, they have been embedded in the control volumes at the left edge near the inlet, i.e.  $\{(i, j) : j = 1, i = 2, \dots, (n_r - 1)\}$  as follows:

$$\frac{d\epsilon_d(i, j)}{dt} = \frac{v_x^d(x_{left})\epsilon_{in} - v_x^d(x_{right})\epsilon_d(i, j)}{\Delta x} + \frac{(A_c v_r^d)|_{r_{outer}}\epsilon_d(i+1, j)}{A_x \Delta x} - \frac{(A_c v_r^d)|_{r_{inner}}\epsilon_d(i, j)}{A_x \Delta x} \quad (5.17)$$

$\epsilon_{in}$  is inlet produced water oil cut. For the control volume  $(i, j) = (n_r, 1)$ , there is no radial flow in, hence, the following equation holds.

$$\frac{d\epsilon_d(i, j)}{dt} = \frac{-(A_c v_r^d)|_{r_{inner}}\epsilon_d(i, j)}{A_x \Delta x} + \frac{v_x^d(x_{left})\epsilon_{in} - v_x^d(x_{right})\epsilon_d(i, j)}{\Delta x} \quad (5.18)$$

For the control volume  $(i, j) = (1, 1)$ , there is no radial flow out, hence, the following equation holds.

$$\frac{d\epsilon_d(i, j)}{dt} = \frac{(A_c v_r^d)|_{r_{outer}}\epsilon_d(i+1, j)}{A_x \Delta x} + \frac{v_x^d(x_{left})\epsilon_{in} - v_x^d(x_{right})\epsilon_d(i, j)}{\Delta x} \quad (5.19)$$

For the control volumes  $\{(i, j) : i = n_r, j = 2, \dots, n_x\}$ , there is also no radial flow in. Hence, the following equations hold.

$$\frac{d\epsilon_d(i, j)}{dt} = -\frac{(A_c v_r^d)|_{r_{inner}}\epsilon_d(i, j)}{A_x \Delta x} + \frac{v_x^d(x_{left})\epsilon_d(i, j-1)}{\Delta x} - \frac{v_x^d(x_{right})\epsilon_d(i, j)}{\Delta x} \quad (5.20)$$

For the control volumes  $\{(i, j) : i = 1, j = 2, \dots, n_x\}$ , there is also no radial flow out. Hence, the following equations hold.

$$\frac{d\epsilon_d(i, j)}{dt} = \frac{(A_c v_r^d)|_{r_{outer}} \epsilon_d(i+1, j)}{A_x \Delta x} + \frac{v_x^d(x_{left}) \epsilon_d(i, j-1)}{\Delta x} - \frac{v_x^d(x_{right}) \epsilon_d(i, j)}{\Delta x} \quad (5.21)$$

The rest of the equations can be written for the control volumes  $\{(i, j) : j = 2, \dots, n_x, i = 2, \dots, (n_r - 1)\}$  as follows:

$$\begin{aligned} \frac{d\epsilon_d(i, j)}{dt} = & \frac{v_x^d(x_{left}) \epsilon_d(i, j-1)}{\Delta x} - \frac{v_x^d(x_{right}) \epsilon_d(i, j)}{\Delta x} \\ & \frac{(A_c v_r^d)|_{r_{outer}} \epsilon_d(i+1, j)}{A_x \Delta x} - \frac{(A_c v_r^d)|_{r_{inner}} \epsilon_d(i, j)}{A_x \Delta x} \end{aligned} \quad (5.22)$$

Note that in the above equations for computing the radial velocities at the interface between two radial control volumes, a volumetric averaging was performed.

### 5.3.3 Re-entrainment equations

The model presented so far is governed by two velocities, the  $v_r^d$  and  $v_x^d$ , where  $v_r^d$  has dependency on  $v_x^d$ . If we raise  $F_{in}$ ,  $v_x^d$  will increase and therefore, also  $v_r^d$  will increase.  $d_d$  goes down for higher  $F_{in}$ , which reduces the  $v_r^d$ . The overall effect of  $F_{in}$  on separation is, therefore, a trade-off between the two effects mentioned earlier. We reckon that the separation performance will be affected by the magnitude of  $F_{in}$  as well as the difference between  $F_{over}$  and  $F_{under}$ . In this model,  $F_{over}$  is much lower than  $F_{under}$ . We made an oversimplified assumption of two plug flows based on these two flows. Two flows next to each other with very different velocities will have a tendency to intermix due to radial pressure gradients. It is expected that part of the impure  $F_{over}$  flow will exit with the underflow, which will cause worsening of the achieved separation in  $F_{under}$ . Hence, we expect an re-entrainment flow  $q_{re-en}$  as a function of the difference between the axial velocities achieved in the two flows as shown below.

$$q_{re-en} = k_{re-en} \left( \frac{F_{under}}{\pi(R_o^2 - R_i^2)} - \frac{F_{over}}{\pi R_i^2} \right) \quad (5.23)$$

$k_{re-en}$  is a re-entrainment constant, which is chosen as  $1 \cdot 10^{-6} m^2$ . Intuitively, larger the difference between overflow plug velocity and underflow plug velocity, larger the possibility of re-entrainment of one flow in the other. The above equation captures that effect. We assume here that the overflow is usually controlled to a flow of  $F_{over}$  using a flow controller. Hence, it follows that the loss of flow in overflow due to re-entrainment will be compensated by an equal amount of flow  $q_{re-en}$  from underflow to overflow.

### 5.3.4 Calculation of water quality

The model produces the oil volume fraction in the all the control volumes. These fractions can be used to compute the water quality of the outgoing  $F_{under}$  and  $F_{over}$  streams. To produce an estimate of the oil content, we employ the following equations.

$$\epsilon_{under}^{ideal} = \frac{A_x \sum_{i=4}^{n_r} v_x^d(r) \epsilon_d(i, n_x)}{F_{under}} \quad (5.24)$$

$\epsilon_{under}^{ideal}$  is an estimate of the water quality in the underflow if no re-entrainment was happening. This variable is computed by summing up all the oil outflows that will exit in the radial section ( $R_i < r \leq R_o$ ) for the control volumes on the rightmost edge ( $j = n_x$ ) and dividing it by the underflow  $F_{under}$ . Since the radially outer edge of the control volume ( $3, n_x$ ) is at  $r = R_i$ , we account for underflow from the control volume ( $4, n_x$ ) to ( $n_r, n_x$ ) and for overflow from ( $1, n_x$ ) to control volume ( $3, n_x$ ). Hence, we obtain the following expression for the  $\epsilon_{over}^{ideal}$ .

$$\epsilon_{over}^{ideal} = \frac{A_x \sum_{i=1}^3 v_x^d(r) \epsilon_d(i, n_x)}{F_{over}} \quad (5.25)$$

To compute the real water quality of the underflow, which will be affected by the re-entrainment of the oil rich overflow into the underflow near the exit, we employ the following equation.

$$\epsilon_{under}^{real} = \frac{(F_{under} - q_{re-en}) \epsilon_{under}^{ideal} + (q_{re-en}) \epsilon_{over}^{ideal}}{F_{under}} \quad (5.26)$$

The hydrocyclone model is developed assuming that  $F_{over}/F_{in} > \epsilon_{in}$ , which is most often the case. If, however,  $F_{over}/F_{in} < \epsilon_{in}$ , model could produce  $\epsilon_{over}^{ideal} > 1$ , which is physically not possible. This happens because the model has not been corrected for these special unrealistic scenarios. The correction would mean that the flows out of a donor control volume to a receiver control volume is dependent on the oil hold up of the receiver control volume. If the receiver control volume has an oil hold up close to 1, oil flows into the control volume will approach zero. This modification makes the model severely nonlinear. Hence, for simplicity we do not consider this effect.

### 5.3.5 Model parameters

The model parameters are presented in Table 5.1:

Table 5.1: Model parameters

Parameter	Value	Unit
Outer radius, $R_o$	0.05	$m$
Inner radius, $R_i$	0.025	$m$
Inner core radius, $R_c$	0.0125	$m$
Separator length, $L$	1.7	$m$
Nominal inlet oil cut, $\epsilon_{in}$	1500	$ppm$
Nominal inlet flow, $F_{in}$	100/3600	$m^3/s$
Nominal overflow, $F_{over}$	0.7/3600	$m^3/s$
Swirl number, $\Omega$	2.5	-
Swirl decay coefficient, $C_{decay}$	0.04	-
Oil density, $\rho_o$	881	$kg/m^3$
Water density, $\rho_w$	1064	$kg/m^3$
Viscosity of brine, $\mu$	$10^{-3}$	$Pa \cdot s$
Re-entrainment constant, $k_{re-en}$	$1 \cdot 10^{-6}$	$m^2$
Number of axial discretizations, $n_x$	12	-
Number of radial discretizations, $n_r$	12	-

## 5.4 Control structure

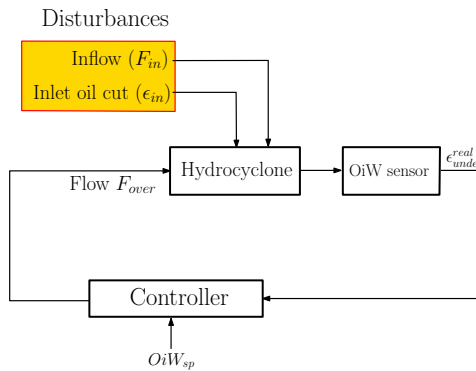


Figure 5.6: HC control using OiW controller.

The model described previously has been considered as a plant for conducting dynamic simulations. Further, we used the model to test a simple PI control law for controlling the processed water oil cut given by  $\epsilon_{under}^{real}$ . The control structure is shown in Figure 5.6, in which we consider inlet flow  $F_{in}$  and incoming oil cut  $\epsilon_{in}$  as disturbances.

The PI controller ( $C(s)$ ) used for computing  $F_{over}$  from  $\epsilon_{under}^{real}$  measurement and its set point  $OiW_{sp}$  is the following. The controller tunings have been derived using

SIMC rules (Skogestad, 2003). Note that the controller takes values for  $\epsilon_{under}^{real}$  in ppm.

$$C(s) = -4.8 \cdot 10^{-6} \left( 1 + \frac{0.25}{s} \right) \quad (5.27)$$

## 5.5 Results

The simulations were performed in MATLAB/Simulink. For finding the steady state, we used the fsolve solver in MATLAB, whereas for the dynamic simulations we used Simulink. The dynamic model was solved using the ode15s solver. The results will be presented in three segments. Firstly, we will present the steady state solution of the oil volume fractions over axial and radial positions for the nominal case using parameter values presented in subsection 5.3.5. In the next segment we will present the dynamic open loop results showing the effect of the disturbances,  $F_{in}$  and  $\epsilon_{in}$  and the manipulated variable  $F_{over}$  on the oil cut  $\epsilon_{under}^{real}$  in underflow. In the last segment, we will present the dynamic closed loop results.

### 5.5.1 Steady state result

The steady state oil volume fractions are shown below.

Table 5.2: Steady state oil fractions

Oil frac. [ $\times 10^{-2}$ ]	$j = 1$	$j = 4$	$j = 8$	$j = 12$
$i = 1$	12.1366	38.0792	53.7138	59.3166
$i = 3$	0.1475	0.1171	0.0666	0.0374
$i = 4$	0.1475	0.1169	0.0663	0.0372
$i = 8$	0.1345	0.0619	0.0174	0.0059
$i = 12$	0.0548	0.0040	0.0003	0.0000

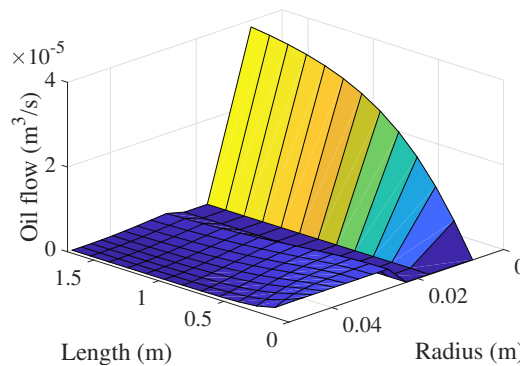


Figure 5.7: Steady state spatial profile of oil flow.

Table 5.2 clearly shows that the oil droplets are gradually moving towards the center ( $i = 1$ ) as they proceed towards the exit ( $j = 12$ ). Next, we present the oil flows out of different control volumes. This result is presented in terms of absolute volumetric flow rate of oil since the densities are considered to be constant.

We see the radially inwards movement of oil in Figure 5.7 as it travels along the length of the separator. At each point in the length, the oil flows out of all radial discretizations add up to  $0.4167 \times 10^{-4} \text{ m}^3/\text{s}$ . For the obtained steady state, the  $\epsilon_{\text{under}}^{\text{ideal}} = 114.1 \text{ ppm}$ ,  $\epsilon_{\text{under}}^{\text{real}} = 147.0 \text{ ppm}$  and  $\epsilon_{\text{over}}^{\text{ideal}} = 0.1981$ .

### 5.5.2 Open-loop results

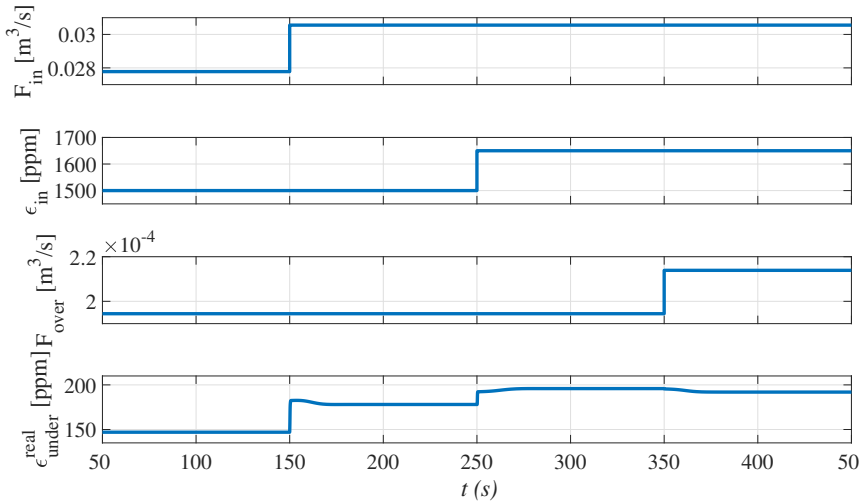


Figure 5.8: Open loop behavior of the hydrocyclone model.

Open-loop results are presented in order to identify the response of changing disturbances, viz.  $F_{in}$  and  $\epsilon_{in}$  on the underflow water quality  $\epsilon_{\text{under}}^{\text{real}}$  in manual mode. We further present also the effect of changing the manipulated variable, the overflow  $F_{\text{over}}$  on the water quality. The open loop results can be seen in the Figure 5.8. When changing the  $F_{in}$ , three effects are in play, namely, reduction in residence time of the water inside the separator, increase in the tangential velocity and reduction in the droplet size. Of these effects, the droplet size reduction has the strongest effect. Reduced droplet size causes a reduction in radial velocity for the oil droplets. Hence, fewer droplets reach the overflow. Therefore, we see in Figure 5.8 that the oil content in the underflow rises. An increase in inlet oil content  $\epsilon_{in}$  results in an increased oil content in the underflow, which is as expected. An increase in overflow  $F_{\text{over}}$  reduces the the oil content of the produced water. Hence, overflow is considered as a suitable manipulated variable for control design for controlling the water quality.

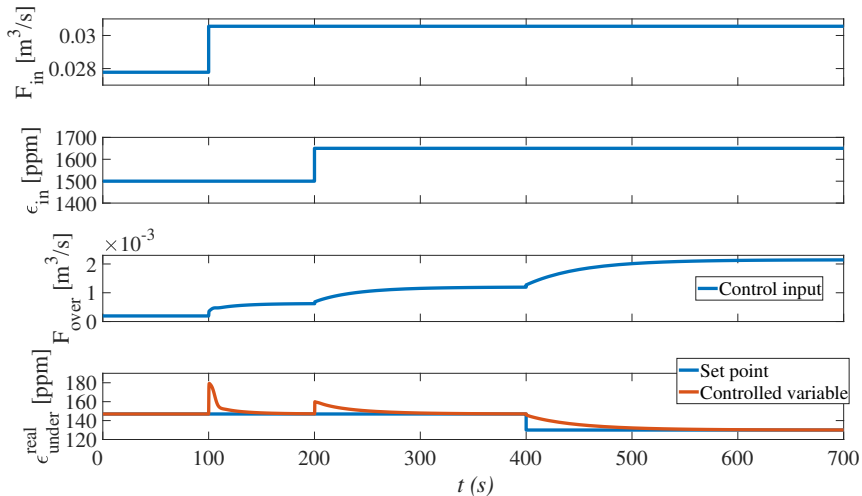


Figure 5.9: Closed loop behavior of the hydrocyclone model.

### 5.5.3 Closed-loop results

Based on the previous analysis, we chose  $F_{over}$  as our control input to control the underflow water quality  $\epsilon_{under}^{real}$ . Here, we subject the system to disturbances, such as changes in inlet oil content and inflow and we try to maintain the controlled variable to a set point of 147 *ppm*. For the closed loop performance, see Figure 5.9. The controller acts quite rapidly when the inflow is raised by 10%. It takes around 50 seconds before the controlled variable is brought back to the set point. A similar behavior is noticed when inlet oil content is raised by 10%, in which water quality is off-spec for just around 50 seconds. Finally, we test the closed loop performance subject to a change in the set point from 147 to 130 *ppm*. The response time has been noted to be in the range of 100 seconds.

## 5.6 Conclusion

In this work, we developed a simplified dynamic model for an inline deoiling hydrocyclone. The model has been derived as a distributed parameter system to dynamically capture the oil content in the processed water. The model is able to study the impact of the disturbances and the control input. However, note that (5.6) is empirical and needs further investigation to ensure validity. Further, a control scheme has been prescribed for controlling the processed water quality using the overflow. The controller tunings have been derived using the SIMC rules. The open loop behavior of the model is according to expectation. The performance of the control structure is satisfactory with response time for disturbance rejection in the range of 50 seconds, while that for a change in set point in the range of 100 seconds.

The modeling work has been conducted as an approach to control the processed water oil quality. A similar approach of modeling can be used to develop dynamic

models for many other separators in which the separation is physically driven such as by gravity or cyclonic forces. For this model, we assume that the oil content can be measured online. The control structure that we designed will heavily depend on the reliability, accuracy and the response time of the Oil in Water sensors. For that, the results shown in (Durdevic et al., 2016) on the evaluation of Oil in Water sensors for control seem promising.

## **Acknowledgements**

We acknowledge the discussions that we had with Prof. Hugo Atle Jakobsen for this paper. We also acknowledge the financial support from SUBPRO, a Research-based Innovation Centre within Subsea production and processing.

## Chapter 6

# A simplified first-principles model of a compact flotation unit for use in optimization and control

In this paper, we develop a simplified control-oriented model of a compact flotation unit (CFU), which removes residual oil from produced water in oil and gas production systems. CFU is a class of separators that exploits the synergy between separation effects of a swirling flow and the effect of flotation, in which small gas bubbles attach to the oil droplets, and float to the top of the separator, where they are removed. The purified water flows downwards, and is removed from the bottom. Our CFU model consists of a simplified initial swirl separation part, and a flotation part, in which populations of oil droplets, gas bubbles without oil droplet, and gas bubbles with oil droplet attached are tracked spatially. After analyzing the model, we use it as a basis for designing a control structure that operates the separation system optimally.

*Revised version submitted for publication in Industrial & Engineering Chemistry Research, 2018*

### 6.1 Introduction

In oil and gas production, besides hydrocarbons a significant amount of water is produced from the reservoirs. Such water is called produced water, and it must be cleaned from hydrocarbons before it can be discharged into the environment or re-injected into a reservoir. For an overview of the different technologies available for produced water treatment within oil and gas industry, we refer to (Fakhru'l-Razi et al., 2009). The amount of dispersed oil in produced water that can be discharged to the sea is maximally 30 mg/l ( $\approx 30$  ppm) as per OSPAR Recommendation 2001/1 (OSPAR is the convention for the Protection of the Marine Environment of the North-East Atlantic) (OSPAR, 2001). Also for water re-injection into the reservoir, it is important that the water has very low oil content, as well as is low on other

metrics, such as turbidity or volatile suspended solids (VSS), otherwise there is a risk of clogging of the pores of the reservoir (Pavelic et al., 2007).

Traditionally, the separation of oil and water has been performed in topside facilities or onshore in large vessels, but in recent years there has been an interest in developing compact separation systems that can be placed on the seabed or on small unmanned platforms. The oil industry has, therefore, been especially interested in compact technologies not only for bulk separation but also for high purity separation, such as hydrocyclones and compact flotation units (CFU), in order to obtain the desired oil content in water. The term compact flotation unit does not denote a single technology, but rather a range of technologies that combine the separation effect of swirling flows with a flotation mechanism. Many different designs have been developed by industrial vendors, of which the more complex designs involve a combination of induced and dissolved gas flotation, as well as several swirl and flotation stages.

Due to a low residence time in compact separation equipment and due to several degrees of freedom in operation, these compact systems, in comparison to conventional separation technologies, are more difficult to operate, and require more advanced control strategies (Arvoh et al., 2012a; Asdahl and Rabe, 2013). Control of CFUs has been studied experimentally by (Asdahl and Rabe, 2013; Arvoh et al., 2012b,a), who analyze the effect of changing the reject valve position and CFU pressure on gas and liquid reject flow rates. These relationships helped them to develop a control system for CFU that optimizes separation efficiency and reject flow rate, and minimizes flotation gas usage using an automatic empirical approach (Asdahl and Rabe, 2013). However, to the authors' knowledge, there has been no analysis of CFU operation based on models - a gap we fill in this paper.

The first contribution of this paper is a control-oriented model of a CFU that is based on physical insight, and that is suitable for use in modern control, optimization and estimation algorithms. This model can be used to describe the effect of important disturbances, such as inlet water flow rate, and inlet oil concentration on processed water quality. Besides, it also captures the response of oil content in water outlet and the separation efficiency to changes in flotation gas rate. The second contribution of this paper is the development of a control structure based on this model, together with a thorough study of the performance of this control structure under various disturbances.

## 6.2 CFU technology

### 6.2.1 Concept of flotation

A flotation device is shown schematically in Figure 6.1. The main concept of flotation is that the produced water containing small droplets of oil is fed into a vessel, and flows downwards towards the bottom of the device. Flotation gas is injected into the separator and forms tiny bubbles. These bubbles travel upwards, and along the way attach to oil droplets and drag them to the top, where the oil and gas is removed in the reject stream. The reject typically also contains some water while rest of the water gets cleaner and cleaner as it travels downwards. Finally, the purified water is removed from the bottom.

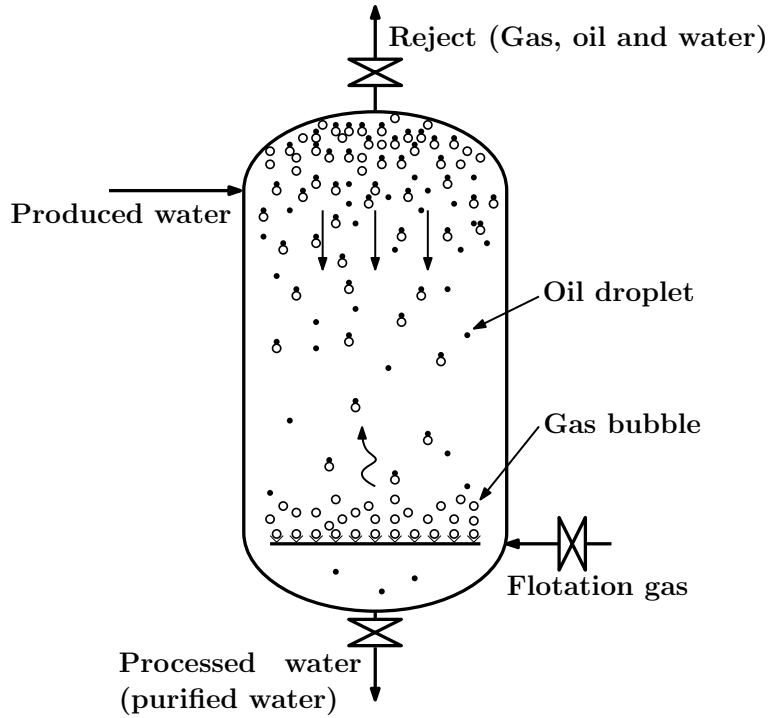


Figure 6.1: Schematic of a flotation device. The figure shows how gas bubbles of the flotation gas attach to oil droplets as they rise upwards. The gas bubbles, either loaded with oil or free, get accumulated at the top and are removed via the reject stream. The purified water is removed at the bottom.

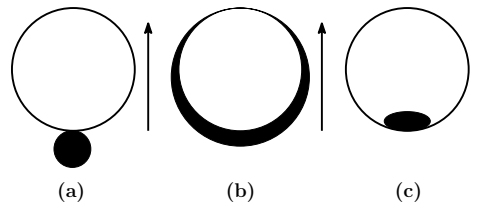


Figure 6.2: Scenarios after collision between droplets and bubbles: (a) Point attachment, (b) Oil film and (c) Oil lens (adapted from (Rawlins and Ly, 2012)).

Mechanisms affecting the flotation process in produced water treatment have been described e.g. by (Frankiewicz et al., 2005). According to them, a low contact angle between the oil droplet and the gas bubble facilitates either oil coating the gas bubbles or oil sticking to the gas bubbles, both of which lead to oil floating to the top with the gas bubbles. A third scenario in which oil forms a lens near the inner bottom edge of the bubble is also possible (Rawlins and Ly, 2012). The three scenarios are shown in Figure 6.2.

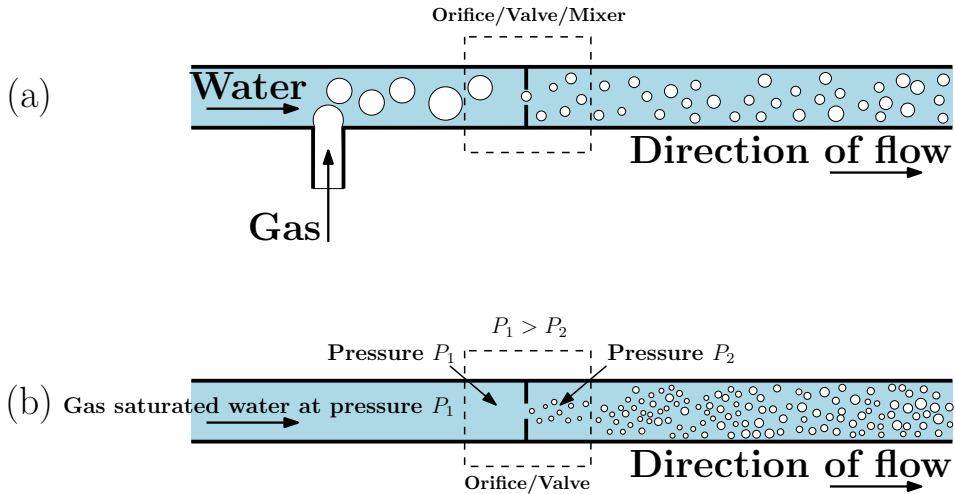


Figure 6.3: Gas flotation methods: (a) Induced gas flotation and (b) Dissolved gas flotation (adapted from (Shannon, 2016)).

For effective separation, the conditions in the separator must enable a good contact between the gas bubbles and the oil droplets. This means that the number density of the droplets and the bubbles should be sufficiently large to ensure a high collision frequency between these two populations. From this perspective, many small bubbles are better than few large bubbles, as a high number density results in a higher probability of collision (Frankiewicz et al., 2005).

Gas flotation can be realized by two different techniques - induced gas flotation (IGF) and dissolved gas flotation (DGF). In induced gas flotation, illustrated in Figure 6.3 top, the injected gas directly forms bubbles of diameters in the range of  $100\text{-}1000\ \mu\text{m}$ . As IGF results in relatively large bubbles, the bubbles have a high rising velocity, which makes it suitable to inject the gas at the bottom of the separator. In dissolved gas flotation, as shown in Figure 6.3 bottom, the gas enters the separator saturated in a liquid at high pressure. When the pressure is reduced, bubbles of gas form. This technique yields smaller bubbles in the range of  $10\text{--}100\ \mu\text{m}$  in diameter (Moosai and Dawe, 2002). Modern CFU designs combine the two flotation methods as there are disadvantages of using only one. In DGF systems, oil droplets larger than  $100\ \mu\text{m}$  cannot be floated, because the volume of the gas bubbles is not high enough to ensure that they attach to the oil droplets and successfully rise to the top of the separator. On the other hand, in IGF systems, oil droplets with sizes much smaller than  $100\ \mu\text{m}$  may escape flotation, as small oil droplets do not attach well to large gas bubbles.

### 6.2.2 A compact flotation unit design with induced gas flotation

As mentioned above, there are several CFU designs, many of which have resulted due to a continuous improvement over previous designs (Bhatnagar and Sverdrup, 2014; Maelum and Rabe, 2015; Hayatdavoudi et al., 2011). In this paper we consider

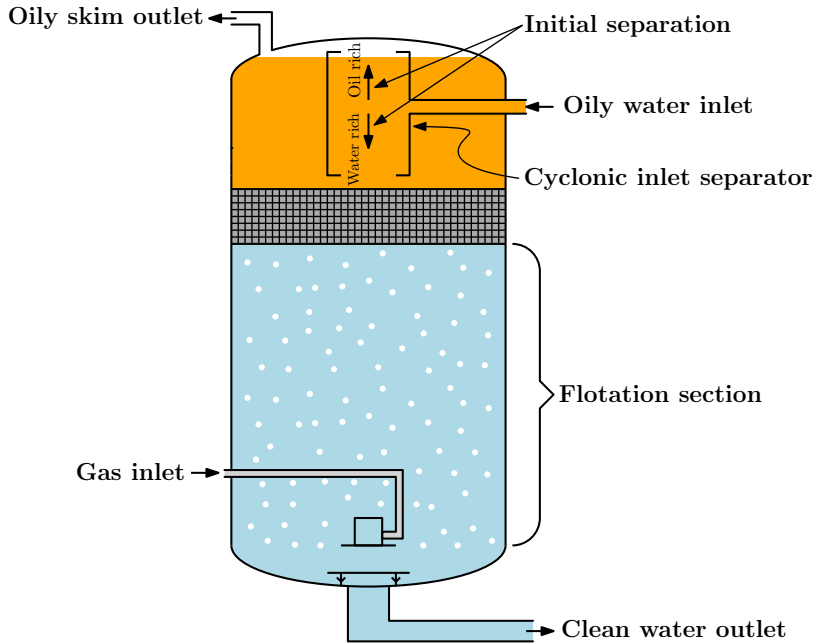


Figure 6.4: Simple CFU design considered in this paper.

a simple CFU design that uses IGF with flotation gas fed at the bottom, as shown in Figure 6.4. A similar design has been proposed by e.g. the *NATCO Group Inc* (Frankiewicz et al., 2005). A feed of oily water enters at the top of the separator and undergoes a swirling motion at the start, which causes some of the oil droplets to separate at the top, while the rest of the oily water flows downwards. A swarm of gas bubbles is injected continuously at the bottom of the separator. These bubbles stick to or get coated with the oil droplets in the water, and carry them to the top. The flotation gas flow is typically 10% (volume/volume) of the incoming water flow (Eftekhardadkhah et al., 2015). At the top of the CFU, the collected oil and gas along with some water is removed through the reject stream. The liquid flow in the reject stream at the top is typically maintained at around 1% of the incoming water flow (Asdahl and Rabe, 2013) and the purified water typically has an oil concentration below 30 ppm.

## 6.3 Control-oriented CFU model

### 6.3.1 Modeling concept and assumptions

The schematic of our CFU model is given in Figure 6.5. The feed enters first into the swirl part, where an initial separation of part of the oil takes place. Then, the water with the remaining oil enters the flotation section. The model of the flotation section is based on mass balances for three entities: free gas bubbles, free oil droplets and loaded bubbles. A loaded bubble results from a merger of one oil

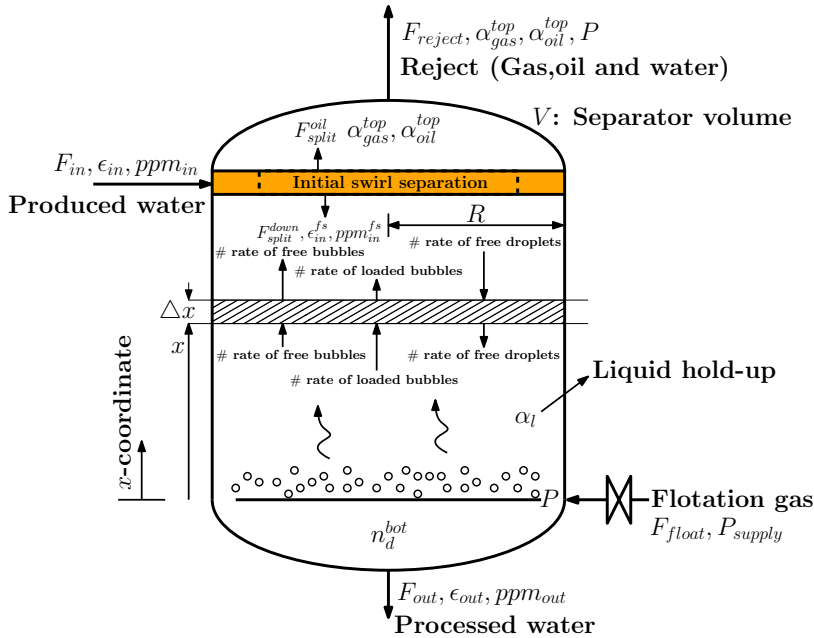


Figure 6.5: Schematic view of the CFU model. All the important variables used in the model are indicated.

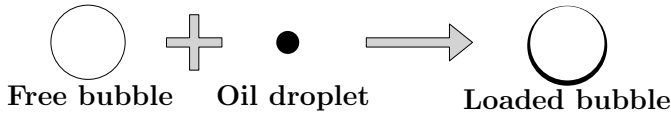


Figure 6.6: Representation of loading process as a combination of an oil droplet and a free bubble.

droplet and one gas bubble as shown in Figure 6.6. The free gas bubbles and the loaded bubbles move upwards, whereas the oil droplets move downwards. The free bubbles and the loaded bubbles leave the CFU through the reject stream at the top. Other major assumptions made are as follows:

1. All liquid is assumed incompressible.
2. Gas is modeled by ideal gas law.
3. The swirl effect is dependent on the inflow and is captured in the initial swirl separation part. In the flotation model, the swirl effect is assumed to be negligible<sup>1</sup>.
4. After the initial swirl separation, the water continuum (bulk phase) is uniformly distributed and moves down at a constant velocity as a plug flow.

<sup>1</sup>As we will see later, this assumption can be relaxed somewhat by adapting the collision efficiency in the flotation part.

5. All oil droplets are assumed spherical, have the same representative diameter, and are uniformly distributed in the horizontal cross section of the vessel. As oil droplets go through swirling effect in initial separation of CFU as shown in Figure 6.5, they coalesce and then represent a sharp distribution with majority of droplets having similar size.
6. The oil droplets, the loaded bubbles and the free bubbles assume terminal velocities relative to the continuous water phase given by the Stokes' law. The free and the loaded bubbles rise while the oil droplets move downwards with the bulk.
7. All bubbles - loaded and free - are of spherical shape.
8. All gas bubbles are assumed to have the same diameter and each gas bubble can float at most one oil droplet. The device used to produce gas bubbles in the CFU is designed to deliver bubbles of a fixed standard size.
9. The size of the bubbles (free as well as loaded) is assumed to be not affected by the pressure gradient along the height of the separator because the pressure difference between top and bottom of the separator does not affect the bubble sizes significantly.
10. The volume of a loaded bubble is the sum of the droplet volume and the bubble volume.
11. The amount of oil and gas dissolved in the water is negligible.

### 6.3.2 Simplified initial swirl separation model

The initial separation due to swirling effect causes oil droplets to travel towards the center radially due to cyclonic forces, which leads to small droplets coalescing to become larger droplets. Also, the turbulent flow enables a higher collision frequency between the droplets, and therefore, facilitates coalescence. The larger droplets have a higher rise velocity, such that they move upwards to enter the top part of the swirl separator and get separated. We assume that this phenomenon happens relatively fast. Hence, we model it as a static split called swirl split. In particular, the swirl split of the initial separator is defined as  $\epsilon_{in}^{fs}/\epsilon_{in}$ , that is the ratio of the oil cut  $\epsilon_{in}^{fs}$  of water entering the flotation section, to the feed concentration  $\epsilon_{in}$ . We propose to model the effect of the swirl separator as a function of swirl intensity  $S$ , which is a measure of the strength of the swirl effect, such that

$$\frac{\epsilon_{in}^{fs}}{\epsilon_{in}} = A(S - B)^2 + C, \quad (6.1)$$

where, the parameters are swirl split pre-factor  $A$ , optimum swirl intensity  $B$  and optimum swirl split  $C$ . The swirl intensity  $S$  is assumed to be linearly dependent on inflow  $F_{in}$  as

$$S = DF_{in}, \quad (6.2)$$

where,  $D$  denotes swirl intensity pre-factor. This assumption is an extension of the linear dependence of the maximum tangential velocity to inflow that is used in equation (3.5) in work of (Tyvold, 2015).

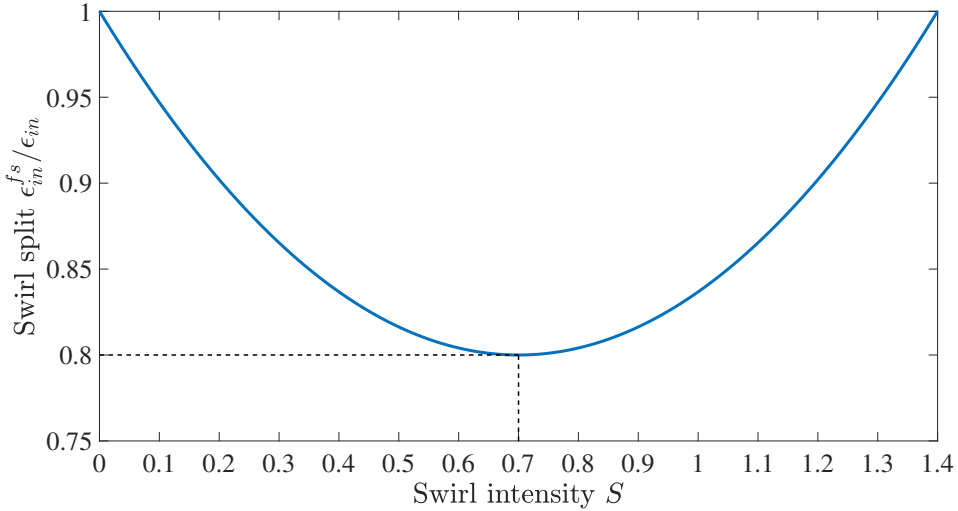


Figure 6.7: Swirl split as a function of swirl intensity  $S$  presented with optimum swirl intensity  $B = 0.7$ , optimum swirl split  $C = 0.8$ . Pre-factor  $A$  is chosen 0.4082 such that for zero inflow, which also means zero swirl intensity, i.e.  $S = 0$ , swirl split is 1, indicating no initial separation.

The swirl split from (6.1) is shown for a chosen set of parameters in Figure 6.7. It reflects the fact that the swirling effect improves separation only up to a certain optimal swirl intensity, which is assumed to be of value  $B$  here. Beyond the optimal swirl intensity, breakage of droplets due to the momentum of the swirl dominates over the coalescence effects, and the separation efficiency of the initial swirl separation deteriorates. In the proposed relationship in (6.1) the swirl split assumes the lowest value of  $C$  at an optimum swirl intensity  $B$ . For all other values of swirl intensity,  $\epsilon_{in}^{fs} / \epsilon_{in}$  will be higher than  $B$ , indicating poorer initial separation.

### 6.3.3 Flotation model

#### Bubble loading model

The separation dynamics in the flotation model are governed by a specific bubble loading rate, which is related to the rate of “successful” collisions between bubbles and oil droplets. A successful collision is defined as one in which attachment between the droplet and the bubble happens. The collision efficiency  $E_c$  is defined analogous to that in a reaction rate for a reactive system as (Oliveira et al., 1999)

$$L_R = E_c n_{fb} n_d, \quad (6.3)$$

where,  $L_R$  is the loading rate, and  $n_{fb}$  and  $n_d$  represent the local number density (volumetric) of free bubbles and droplets, respectively. The collision efficiency  $E_c$

is a function of droplet and bubble sizes as given by (Oliveira et al., 1999)

$$E_c = k \left( \frac{d_d}{d_b} \right)^2, \quad (6.4)$$

where,  $d_b$  and  $d_d$  are bubble and droplet diameters, respectively, and  $k$  is a tuning parameter that governs the kinetics of the loading phenomenon.

**Remark 6.1.** We have assumed perfect plug flow and no swirl in the flotation section. If, however, the swirl effect, or other turbulent and non-ideal effects need to be considered in the flotation section, they can be absorbed into the parameter  $k$ . For example, one may use operational data to fit a function  $k = f(F_{in})$ , and then use this instead of a constant value.

### Mass Balances

The feed  $F_{in}$  containing oil and water is fed into the initial swirl separation and splits into two flows - the separated oil flow  $F_{split}^{oil}$  that enters the top section, and the rest flow  $F_{split}^{down}$  with oil concentration  $\epsilon_{in}^{fs}$  that enters the flotation section from the top, while the flotation gas is injected between the flotation section and the bottom section, see Figure 6.8.

In our model we use the following notation (see also Figure 6.5):  $F_{in}$  for the oily water inflow rate,  $\epsilon_{in}$  for inlet oil in water content (volume/volume) in water feed, which in *ppm* terms is denoted as  $ppm_{in}$ ,  $F_{split}^{oil}$  for oil flow that is separated due to initial separation and travels upwards,  $F_{split}^{down}$  for the part of inflow  $F_{in}$  that travels downwards containing an oil concentration of  $\epsilon_{in}^{fs}$ , which in *ppm* terms is denoted as  $ppm_{in}^{fs}$ ,  $F_{out}$  for water outflow rate,  $\epsilon_{out}$  for outlet oil in water content (volume/volume) in water outflow, which in *ppm* terms is denoted as  $ppm_{out}$ ,  $F_{float}$  for flotation gas rate,  $F_{reject}$  for the total multiphase reject flow rate and  $\alpha_{gas}^{top}$  and  $\alpha_{oil}^{top}$  for volume fractions of gas and oil, respectively in the reject stream as well as in the top section. The model implements a mass balance on each of the entities - free bubbles, loaded bubbles and oil droplets - over several control volumes. Since the bubbles and droplets are assumed to be of a single representative size each throughout the separator, writing a balance on the number of these entities is equivalent to writing mass balances. The control volumes are segments of the CFU, with each control volume of the shape of a flat cylinder as shown in Figure 6.8. Hence, we present a number balance for each entity in one control volume of length  $\Delta L$  and cross section area  $\pi R^2$ , with  $\Delta V$  as the section volume,

$$\Delta V = \pi R^2 \Delta L. \quad (6.5)$$

We divide the flotation section of the CFU into 3 sections (see Figure 6.8) - a top section, from which oil, gas and some water is removed, a flotation section, where the flotation is taking place, and a bottom section, where the purified water is removed. We consider a total of  $(N + 2)$  control volumes, of which the middle  $N$  (in light-gray) are in the flotation section. The dark-gray colored control volume corresponds to the top (outlet) section, whereas the blue colored control volume

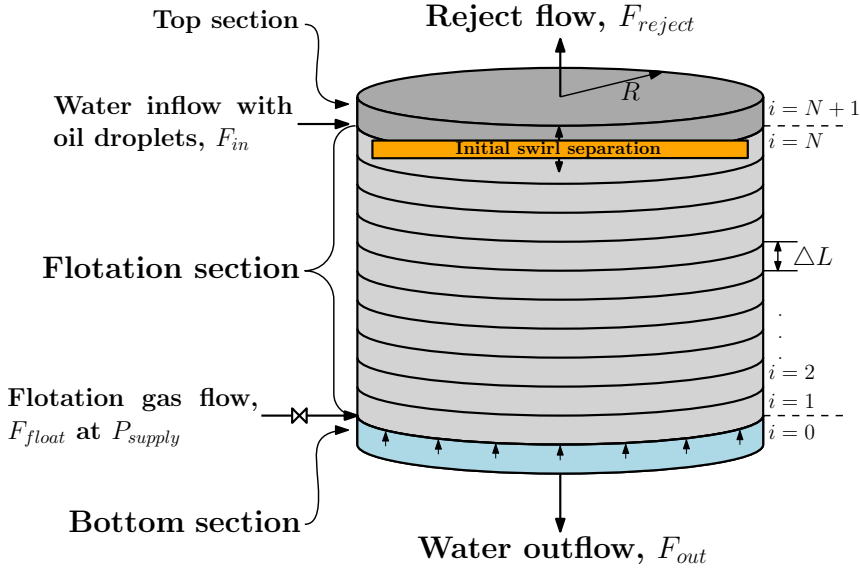


Figure 6.8: Control volumes. The top section, the bottom section and the flotation section are indicated with the location of introduction of water inflow, reject flow, water outflow and flotation gas inflow. The indices for the control volumes are also shown.

corresponds to the bottom (outlet) section. All the control volumes have the same volumes and we assume that the water outflow from the initial swirl separator enters the flotation section right below the top section, see Figure 6.8.

First we address the light-gray colored flotation section control volumes and thereafter the blue colored (bottom section) and dark-gray colored (top section).

### Flotation section

The control volumes in flotation section are indexed from  $i = 1$  to  $N$ . We treat the balances on the control volumes differently, depending on if the control volume is at the boundary or in the interior.

**Inner control volumes:**  $i = 2$  to  $N - 1$ , the balance equation for free bubbles is:

$$\underbrace{\frac{d}{dt} (n_{fb}(i)\Delta V)}_{\text{Accumulation rate}} = \underbrace{n_{fb}(i-1)v_{fb}\pi R^2}_{\text{Inflow rate}} - \underbrace{n_{fb}(i)v_{fb}\pi R^2}_{\text{Outflow rate}} - \underbrace{L_R \Delta V}_{\text{Consumption rate}} \quad . \quad (6.6)$$

After rearrangement, we obtain

$$\frac{dn_{fb}(i)}{dt} = v_{fb} \frac{n_{fb}(i-1) - n_{fb}(i)}{\Delta L} - k \left( \frac{d_d}{d_b} \right)^2 n_{fb}(i)n_d(i). \quad (6.7)$$

Similar expressions for  $n_d$  and  $n_{lb}$  results in the following equations

$$\frac{dn_d(i)}{dt} = v_d \frac{n_d(i+1) - n_d(i)}{\Delta L} - k \left( \frac{d_d}{d_b} \right)^2 n_{fb}(i) n_d(i). \quad (6.8)$$

$$\frac{dn_{lb}(i)}{dt} = v_{lb} \frac{n_{lb}(i-1) - n_{lb}(i)}{\Delta L} + k \left( \frac{d_d}{d_b} \right)^2 n_{fb}(i) n_d(i). \quad (6.9)$$

The velocity  $v_{fb}$  is the absolute velocity of free bubble in the upward direction. The velocity  $v_d$  is the absolute velocity of oil droplet in the downward direction. The velocity  $v_{lb}$  is the absolute velocity of loaded bubble in the upward direction. A diagrammatic representation of the velocities for the three entities is shown in Figure 6.9.

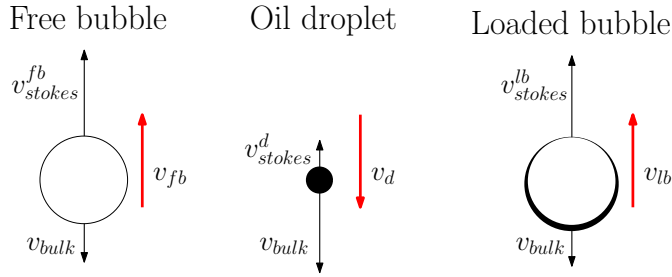


Figure 6.9: Schematic of velocities. The red arrows indicate the net effect, which is the superposition of the effects indicated by black arrows.

The velocities used in the equations above are derived using Stokes' law.

$$v_{fb} = \frac{\overbrace{(\rho_w - \rho_g) g d_b^2}^{v_{stokes}^{fb}}}{18\mu_w} - v_{bulk} \quad (6.10)$$

$$v_d = v_{bulk} - \frac{\overbrace{(\rho_w - \rho_o) g d_d^2}^{v_{stokes}^d}}{18\mu_w} \quad (6.11)$$

$$v_{lb} = \frac{\overbrace{((\rho_w - \rho_g) V_{fb} + (\rho_w - \rho_o) V_d) g}^{v_{stokes}^{lb}}}{3\pi\mu_w(d_b^3 + d_d^3)^{1/3}} - v_{bulk} \quad (6.12)$$

$$v_{bulk} = \frac{F_{out}}{(\pi R^2) \alpha_l} \quad (6.13)$$

Here,  $v_{bulk}$  represents continuum velocity in the downward direction.  $F_{out}$  is volumetric outflow rate of the processed water from the bottom of the separator.

$\alpha_l$  is the liquid hold-up inside the separator. The gas density  $\rho_g$  is computed using ideal gas law as

$$\rho_g = \frac{PM_g}{R_g T}, \quad (6.14)$$

where  $P, M_g, R_g$  and  $T$  are separator pressure, molecular weight of gas, universal gas constant and temperature, respectively.

**Control volumes on the boundary in flotation section:**

For control volume  $i = 1$ , situated right above the flotation gas inlet, the equations are different from the equations presented for the inner control volumes earlier because of the boundary conditions arising from the inflow of flotation gas and that there is no source term for the loaded bubbles at this control volume. For the free bubbles, the mass balance yields

$$\frac{dn_{fb}(1)}{dt} = \frac{1}{\Delta L} \left( \frac{F_{float} (P_{supply}/P)}{V_{fb} (\pi R^2)} - v_{fb} n_{fb}(1) \right) - k \left( \frac{d_d}{d_b} \right)^2 n_{fb}(1) n_d(1). \quad (6.15)$$

Similarly, for  $n_d$  and  $n_{lb}$  we obtain

$$\frac{dn_d(1)}{dt} = v_d \frac{n_d(2) - n_d(1)}{\Delta L} - k \left( \frac{d_d}{d_b} \right)^2 n_{fb}(1) n_d(1) \quad (6.16)$$

and

$$\frac{dn_{lb}(1)}{dt} = -v_{lb} \frac{n_{lb}(1)}{\Delta L} + k \left( \frac{d_d}{d_b} \right)^2 n_{fb}(1) n_d(1). \quad (6.17)$$

Here,  $F_{float}$  is flotation gas flow rate supplied at pressure  $P_{supply}$ , and  $V_{fb}$  is the volume of a free bubble at the separator pressure.

For control volume  $i = N$ , below the water feed, the following equations hold. They are different from the inner control volumes because of the boundary conditions arising from the feed of water containing dispersed oil.

$$\frac{dn_{fb}(N)}{dt} = \frac{v_{fb}}{\Delta L} (n_{fb}(N-1) - n_{fb}(N)) - k \left( \frac{d_d}{d_b} \right)^2 n_{fb}(N) n_d(N) \quad (6.18)$$

Similar expressions for  $n_d$  and  $n_{lb}$  result

$$\frac{dn_d(N)}{dt} = \frac{1}{\Delta L} \left( \frac{F_{split}^{down} \epsilon_{in}^{fs}}{V_d (\pi R^2)} - v_d n_d(N) \right) - k \left( \frac{d_d}{d_b} \right)^2 n_{fb}(N) n_d(N), \quad (6.19)$$

where,  $V_d$  is the volume of an oil droplet and  $F_{split}^{down}$  is obtained using a mass balance on water as

$$F_{split}^{down} = \frac{F_{in}(1 - \epsilon_{in})}{(1 - \epsilon_{in}^{fs})}, \quad (6.20)$$

and

$$\frac{dn_{lb}(N)}{dt} = v_{lb} \frac{n_{lb}(N-1) - n_{lb}(N)}{\Delta L} + k \left( \frac{d_d}{d_b} \right)^2 n_{fb}(N) n_d(N). \quad (6.21)$$

### Bottom section

We assume that no free bubble and no loaded bubble manage to reach this section, see Assumption 6. Hence, we do not need to account for their number densities in the bottom section. We only need an equation for the number density of droplets.

$$\frac{dn_d^{bot}}{dt} = \frac{1}{\Delta L} \left( v_d n_d(1) - \frac{F_{out}}{\pi R^2} n_d^{bot} \right). \quad (6.22)$$

The oil in water at water outlet is computed in *ppm* terms by

$$ppm_{out} = n_d^{bot} V_d \cdot 10^6 \quad (6.23)$$

Before we present the balance equations for the top section, we need to present the balance for the gas hold-up.

### Gas balance

Since there is no chemical reaction, the mass balance of gas is expressed in terms of a molar balance, and the total number of moles of gas in the CFU  $w_{gas}$  follows the conservation law

$$\frac{dw_{gas}}{dt} = \dot{w}_{gas,in} - \dot{w}_{gas,out}. \quad (6.24)$$

Here,  $\dot{w}_{gas,in}$  is the molar flow rate of the flotation gas entering the vessel and  $\dot{w}_{gas,out}$  is the molar flow rate of the gas removed from the vessel with the reject flow. Using ideal gas law, we reformulate (6.24) to

$$\frac{d}{dt} \left( \frac{PV_g}{R_g T} \right) = \left( \frac{P_{supply} F_{float}}{R_g T} \right) - \left( \frac{P F_{reject}^{gas}}{R_g T} \right). \quad (6.25)$$

Here,  $P$  denotes the CFU pressure,  $F_{reject}^{gas}$  the gas flow rate in the reject stream and  $V_g$  the gas volume inside the separator. Multiplying by  $R_g T$  and expanding the left hand side yields

$$V_g \frac{dP}{dt} + P \frac{dV_g}{dt} = \left( P_{supply} F_{float} - P F_{reject}^{gas} \right). \quad (6.26)$$

Since total CFU volume is fixed, we have  $V = V_g + V_l$ , where  $V_l$  is liquid volume in CFU, differentiating which, we get

$$\frac{dV_g}{dt} = -\frac{dV_l}{dt}. \quad (6.27)$$

Using (6.27), (6.26) is further expressed as

$$V_g \frac{dP}{dt} = P \frac{dV_l}{dt} + \left( P_{supply} F_{float} - P F_{reject}^{gas} \right). \quad (6.28)$$

Using

$$V_g = V - V_l, \quad (6.29)$$

we can write the pressure equation as

$$\frac{dP}{dt} = \frac{P(dV_l/dt) + (P_{supply}F_{float} - PF_{reject}^{gas})}{V - V_l}. \quad (6.30)$$

The term  $\frac{dV_l}{dt}$  can be obtained from the balance on liquid volume  $V_l$  as below taking Assumption 1 (incompressibility of liquids) into account

$$\frac{dV_l}{dt} = F_{in} - F_{out} - (F_{reject} - F_{reject}^{gas}). \quad (6.31)$$

The equation can be reformulated in terms of the liquid hold-up  $\alpha_l = \left(\frac{V_l}{V}\right)$  as

$$\frac{d\alpha_l}{dt} = \frac{F_{in} - F_{out} - (F_{reject} - F_{reject}^{gas})}{V}, \quad (6.32)$$

where  $F_{reject}^{gas}$  can be computed by the equation

$$F_{reject}^{gas} = \alpha_{gas}^{top} F_{reject}. \quad (6.33)$$

The equation for the hold up of gas in the top section of the CFU  $\alpha_{gas}^{top}$  can be found below.

### Top section

Based on our assumptions, free bubbles, loaded bubbles and oil droplets separated through initial swirl separation manage to reach this section. The equation for gas hold up in top section  $\alpha_{gas}^{top}$  is

$$\frac{d\alpha_{gas}^{top}}{dt} = \frac{1}{\Delta L} \left( V_{fb} v_{fb} n_{fb}(N) + v_{lb} n_{lb}(N) - \frac{\alpha_{gas}^{top} F_{reject}}{\pi R^2} \right), \quad (6.34)$$

and that for oil hold up in top section  $\alpha_{oil}^{top}$  is

$$\frac{d\alpha_{oil}^{top}}{dt} = \frac{1}{\Delta L} \left( V_d v_{lb} n_{lb}(N) + \frac{F_{split}^{oil} - F_{reject}^{oil}}{\pi R^2} \right), \quad (6.35)$$

where, the oil separated at the initial separation that enters the top section directly is

$$F_{split}^{oil} = F_{in} \epsilon_{in} - F_{split}^{down} \epsilon_{in}^{fs} \quad (6.36)$$

The amount of oil removed through the reject flow  $F_{reject}$  is

$$F_{reject}^{oil} = \alpha_{oil}^{top} F_{reject}. \quad (6.37)$$

### Bubble injection model

The flotation gas is supplied at pressure  $P_{supply}$ , see Figure 6.5. When it enters the separator, which has a lower pressure, the volumetric flow rate at CFU pressure  $P$  becomes  $F_{float} (P_{supply}/P)$ . The bubbles generated are considered to be of uniform size  $d_b$ .

To obtain the flow of number of free bubbles entering between the bottom section and the flotation section, the adjusted flow is then divided by the volume of each bubble  $V_{fb}$ . This yields

$$\dot{n}_{fb}^{feed} = \frac{F_{float} (P_{supply}/P)}{V_{fb}}. \quad (6.38)$$

#### 6.3.4 Model summary

In summary, the model consists of the following dynamic states for the case demonstrated by  $N = 10$ :

- $n_{fb}(i)$ ,  $n_{lb}(i)$  and  $n_d(i)$  for all the control volumes indexed  $i = 1$  to  $N$ , results in  $3N$  states.
- $n_d^{bot}$ ,  $\alpha_{gas}^{top}$  and  $\alpha_{oil}^{top}$ .
- Liquid hold-up ( $\alpha_l$ ) and separator pressure ( $P$ )

These result in a total of  $(3N + 5)$  differential equations.

## 6.4 Case study

### 6.4.1 Model parameters

For our case study, we consider a CFU with the parameters given in Table 6.1. We consider a discretization with  $N = 10$ . This gives a reasonable trade-off between model size and the ability to demonstrate how the concentration profiles in the CFU behave. The tuning parameter  $k$  used in loading rate is considered constant. In operation, the adjustable inputs are the flotation gas feed rate  $F_{float}$ , the reject flow rate  $F_{reject}$ , and the water outflow  $F_{out}$ . The oily water feed flow rate  $F_{in}$  is assumed to be given from an upstream process. We assume that the CFU can be monitored using the measurement vector  $y = [P, \alpha_l, ppm_{out}, \alpha_{oil}^{top}, \alpha_{gas}^{top}]^T$ . An estimate of  $\alpha_l$  can be calculated using differential pressure measurement  $\Delta P = (P_{bottom} - P)$  between top and bottom of the separator and assuming that the gas density is negligible in comparison to that of the liquid. Alternatively, the CFU could be weighed to estimate the liquid content. We assume a measurement delay of 1 second, 2 seconds and 30 seconds for the measurements of pressure  $P$ , liquid hold-up  $\alpha_l$  and water quality  $ppm_{out}$ , respectively.

### 6.4.2 Dynamic model analysis (only stabilizing loop closed)

We analyze the dynamic performance of the model with only one stabilizing control loop closed as shown in Figure 6.10. We close the stabilizing pressure loop in order to control the gas inventory in the separator. The results for operation with the

Table 6.1: Model parameters

Parameter	Value
CFU volume, $V$ [ $m^3$ ]	3.2
CFU diameter, $2R$ [ $m$ ]	1.26
CFU height, $L$ [ $m$ ]	2.56
Density of water, $\rho_w$ [ $kg/m^3$ ]	1000
Density of oil, $\rho_o$ [ $kg/m^3$ ]	900
Molecular weight of flotation gas, $M_g$ [ $g/mol$ ]	16
CFU temperature, $T$ [ $K$ ]	300
Universal gas constant, $R_g$ [ $J/molK$ ]	8.314
Bubble diameter at pressure $P$ , $d_b$ [ $\mu m$ ]	200
Gas supply pressure, $P_{supply}$ [ $bar$ ]	2
Droplet diameter, $d_d$ [ $\mu m$ ]	25
Viscosity of water, $\mu_w$ [ $Pa\cdot s$ ]	$8.9 \times 10^{-4}$
Nominal inlet flow rate, $F_{in}$ [ $m^3/h$ ]	70
Expected range of inlet flow rate, $F_{in}$ [ $m^3/h$ ]	65 – 80
Nominal inlet oil in water, $\epsilon_{in}$ [ $ppm$ ]	150
Expected range of inlet oil in water, $\epsilon_{in}$ [ $ppm$ ]	125 – 175
Tuning parameter in loading rate, $k$ [ $m^3/s$ ]	$4 \times 10^{-11}$
Swirl split pre-factor, $A$ [-]	0.4082
Optimum swirl intensity, $B$ [-]	0.7
Optimum swirl split, $C$ [-]	0.8
Swirl intensity pre-factor, $D$ [-]	0.01
Number of discretizations in flotation section, $N$ [-]	10

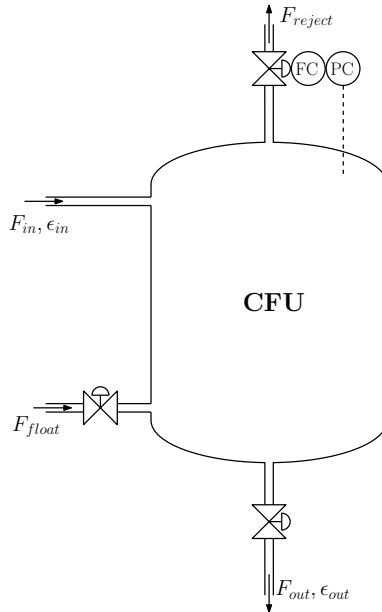


Figure 6.10: Control loop for CFU with only stabilizing pressure loop closed.

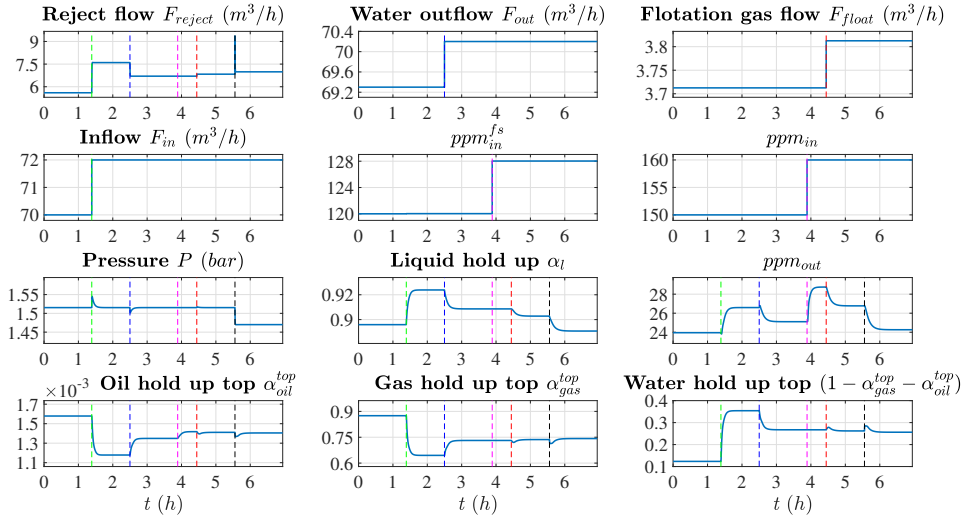


Figure 6.11: Simulation responses of the CFU model with only a stabilizing pressure control loop closed. The first row of plots are manipulated variables, the second row of plots are disturbance variables, the third row plots are controlled variables and the fourth row of plots are other variables.

pressure control loop closed are in Figure 6.11, where, we present the effect of the disturbances ( $F_{in}, ppm_{in}$ ) and the other control inputs ( $F_{float}, F_{out}$ ) on the outputs. A discussion of the responses is given below.

- When inflow is raised at 1.39 h:** The liquid hold up increases and settles at a new higher steady state, whereas some additional water escapes through the reject stream. To maintain the pressure, which spikes up because the liquid hold up rises leaving less space for the gas, the reject flow increases due to the pressure control loop. Since more of the water escapes the reject stream, the hold up of oil and gas reduces and that of water increases in the reject stream.  $ppm_{out}$  increases because the residence time for separation is reduced leading to worse separation performance.
- When water outflow is raised at 2.5 h:** The liquid hold up reduces and settles at a new lower steady state, whereas less water escapes through the reject stream. To maintain the pressure, which spikes downwards because the liquid hold up reduces leaving more space for the gas, the reject flow reduces automatically. Since less of the water escapes the reject stream, the hold up of oil and gas increases and that of water reduces in the reject stream. Since the bulk velocity  $v_{bulk}$  rises due to a higher water outflow and a lower liquid hold up, velocities of bubbles  $v_{fb}$  and  $v_{lb}$  drop. This leads to a higher gas hold up in the system and a higher residence time for bubbles to attach to droplets, which results in an improved separation. Hence,  $ppm_{out}$  reduces.
- When  $ppm_{in}$  is raised at 3.89 h:** The oil concentration  $ppm_{in}^{fs}$  that enters the flotation section rises. The  $ppm_{out}$  goes up because no additional flotation

gas is injected to counteract the additional separation load. Due to additional oil in the system, more of the oil escapes the reject stream causing the oil hold up at the top to increase.

- **When flotation gas flow rate is raised at 4.44 h:** The  $ppm_{out}$  goes down because additional flotation gas improves the separation performance. Due to additional gas in the system, the pressure spikes, but since the pressure is regulated, the reject flow rate increases to take the additional gas out of the system. The additional gas in the system also causes the liquid hold up to drop and the gas hold up at the top to rise marginally, thereby reducing the oil hold up and water hold up at the top somewhat.
- **When pressure set point is reduced at 5.56 h:** The reject flow rises because lower pressure implies higher gas volume inflow at the separator pressure and reject flow is the only stream that takes gas out of the system. Because of the reduced pressure, the gas occupies more volume, which causes the liquid hold up to drop and the gas hold up at the top to rise. At a lower pressure, the volumetric gas inflow at separator pressure into the bottom of the CFU will be higher for the same gas mass inflow, which means more bubbles at the bottom, leading to higher number of droplet-bubble collisions. This directly increases collision efficiency and thereby, improves the separation performance. Hence,  $ppm_{out}$  reduces as gas is used more effectively at a lower pressure.

Quantitatively, the effects of the inputs and disturbances can be approximated by the gains

$$G^y = \frac{\Delta y}{\Delta u} = \begin{bmatrix} 0 & 0 \\ -0.0581 & -0.0170 \\ -19.8 & -1.6501 \\ 7.05 \times 10^{-5} & 1.89 \times 10^{-4} \\ 0.052 & 0.0962 \end{bmatrix}, \text{ and} \quad (6.39)$$

$$G^d = \frac{\Delta y}{\Delta d} = \begin{bmatrix} 0 & 0 \\ 0.014 & -2.93 \times 10^{-7} \\ 1.320 & 0.36 \\ -2 \times 10^{-4} & 6.88 \times 10^{-6} \\ -0.1151 & -2.93 \times 10^{-7} \end{bmatrix}, \quad (6.40)$$

where, we recall that  $y = [P, \alpha_l, ppm_{out}, \alpha_{oil}^{top}, \alpha_{gas}^{top}]^T$ ,  $u = [F_{float}, F_{out}]^T$  and  $d = [F_{in}, ppm_{in}]^T$ .

### 6.4.3 Optimal operation

#### Control structure design

To design the control structure, we follow loosely the top-down plant-wide control design procedure given by (Skogestad, 2004). We start by defining the operational objectives, that is the cost function and operational constraints. The objective of operation for the CFU is to minimize the flotation gas flow given by

$$J = F_{float}. \quad (6.41)$$

There are regulatory requirements of keeping the oil in water outlet below 30 *ppm*. The CFU pressure  $P$  is required to be between  $P_{min} = 1.4$  bar and  $P_{max} = 2$  bar as in our case study we consider a topside CFU, which should be operated slightly higher than ambient pressure to ensure outflow of water, and below the upper limit given by design pressure. For reliable operation, the liquid hold up  $\alpha_l$  is required to be above 0.85 to avoid gas loss from the bottom of the CFU.

The feed rate  $F_{in}$  and the feed composition  $\epsilon_{in}$  are assumed to be given from an upstream process unit. Their nominal values together with their ranges are given in Table 6.1. The process has three degrees of freedom that can be manipulated to optimize performance. These are the flotation gas flow rate  $F_{float}$ , the water outflow rate  $F_{out}$  and the pressure set point  $P^{set}$ . The resulting optimization problem is as follows:

$$\begin{aligned}
 & \min_{F_{float}, F_{out}, P^{set}} && F_{float} \\
 & s.t. && \text{model equations} \\
 & && ppm_{out} \leq 30 \text{ ppm} \\
 & && 1.4 \text{ bar} \leq P \leq 2 \text{ bar} \\
 & && 0.85 \leq \alpha_l \leq 1 \\
 & && n_d(i), n_{fb}(i), n_{lb}(i) \geq 0 \text{ for all control volumes } i
 \end{aligned} \tag{6.42}$$

The optimization problem is solved with the disturbances  $d = [F_{in}, ppm_{in}]$  being varied in the expected range around their nominal point  $[70 \text{ m}^3/\text{h}, 150 \text{ ppm}]$ . For solving the optimization problem we used the IPOPT solver in CasADi library (version 3.3.0) for MATLAB (Andersson, 2013). From the optimization solution, we find:

- The  $ppm_{out}$  constraint is active for all disturbance values. This is as expected because any purification below 30 *ppm* incurs extra cost (flotation gas) that is not necessary.
- The constraint on pressure  $P$  is active on the lower limit of 1.4 *bar*. The objective of minimizing the use of flotation gas implies that the flotation gas has to be used most efficiently. Keeping the pressure as low as possible produces most bubbles for a given gas mass flow rate, and maximizes the separation.
- The lower limit on the liquid hold-up  $\alpha_l$  is active at 0.85. The lower the liquid hold-up, the higher the gas hold up, which indicates more effective use of the flotation gas. A higher gas hold-up indicates a higher number density of the bubbles, which raises the loading rate according to (6.3).

At the optimum, therefore, all three degrees of freedom are used for controlling the active constraints. However, in practice we will keep a back-off from the constraint values such that even under disturbances and imperfect control we do not violate the constraints. Hence, we choose the constrained set points as

$$P^{set} = 1.47 \tag{6.43}$$

$$\alpha_l^{set} = 0.9 \tag{6.44}$$

$$ppm_{out}^{set} = 25 \tag{6.45}$$

As in the previous section, we choose to use the reject stream  $F_{reject}$  to stabilize the pressure  $P$  to set-point  $P^{set}$ . The remaining degrees of freedom  $F_{float}$  and  $F_{out}$  must be then used to control the liquid hold-up  $\alpha_l$  and the purity of the water  $ppm_{out}$  to their optimal constrained values. We suggest the following:

- $ppm_{out}$  is controlled by the flotation gas flow  $F_{float}$ . Flotation gas is the primary agent for separation and directly affects the  $ppm_{out}$ . This can be seen from the large value of the gain element  $-19.8 \text{ ppm}/\text{m}^3/\text{h}$  in (6.39).
- The liquid inventory reflected by liquid hold up  $\alpha_l$  needs to be controlled using a flow that has the most liquid content. Hence, water outflow  $F_{out}$  is a suitable candidate as an input to control  $\alpha_l$ , with a gain of  $-0.017 \text{ 1}/\text{m}^3/\text{h}$ .

Alongside feedback control to control  $ppm_{out}$ ,  $\alpha_l$  and  $P$  using  $F_{float}$ ,  $F_{out}$  and  $F_{reject}$ , respectively, the control structure should also be robust to changes in disturbances, especially when the measurement of  $ppm_{out}$  is affected by a delay. A possible solution is to implement a ratio controller that controls the ratio  $F_{float}/F_{in}$  to a set point  $(F_{float}/F_{in})^{SP}$  that is given by the feedback controller for  $ppm_{out}$ . Note that the pressure controller, the concentration controller and the hold-up controller are giving the set-points to flow controllers in cascade. See Figure 6.12 for the entire proposed control structure.

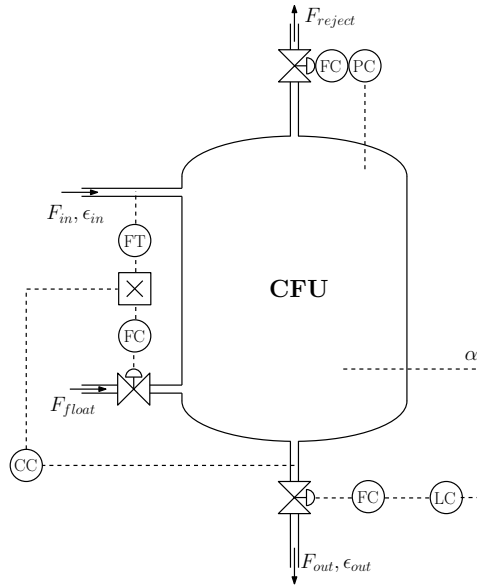


Figure 6.12: Control loops for CFU with ratio control for water quality.

### Steady state operation

From the steady state optimization results, we obtained the set points for the constrained variables  $(P, \alpha_l, ppm_{out}) = (1.47, 0.9, 25)$ ; the disturbances  $d$  are  $[F_{in}, \epsilon_{in}]$

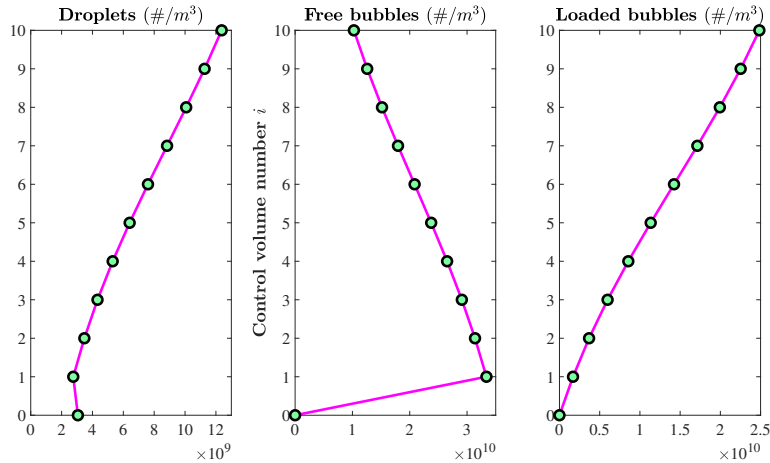


Figure 6.13: Optimal steady state result describing the number densities of free bubbles, oil droplets and loaded bubbles from the bottom section ( $i = 0$ ) to the section  $i = 10$  of CFU.

Table 6.2: Controller tunings

Control loop	$K_c$	$\tau_I$ [s]
$F_{reject} \rightarrow P$	-55.75	200
$F_{out} \rightarrow \alpha_I$	-318.19	204
$(F_{float}/F_{in})^{SP} \rightarrow ppm_{out}$	-0.0036	316

$= [70 \text{ m}^3/h, 150 \text{ ppm}]$ . The optimal number densities are shown in Figure 6.13. The flotation gas enters the control volume  $i = 1$  from the bottom and flows upwards. Hence,  $n_{fb}$  and  $n_{lb}$  are zero in the bottom section  $i = 0$  because bubbles cannot move downwards. It can be noticed that from bottom to top, the number density of free bubbles reduces as many of them are converted into loaded bubbles, which is also reflected in an increase in the number density of loaded bubbles from bottom to top. The number density of droplets reduce from top to bottom because some of the droplets get floated by bubbles and travel upwards.

### Closed loop dynamic simulation results

For the dynamic simulations, the controller parameters were obtained using the SIMC tuning rules by (Skogestad, 2003) and are given in Table 6.2 for PI controllers of the form  $K_c \left(1 + \frac{1}{\tau_I s}\right)$ . As mentioned previously, the optimal set points with back-off compensation are  $(P, \alpha_I, ppm_{out}) = (1.47, 0.9, 25)$ . To demonstrate our model, starting from suboptimal operation we step the set points one by one to their optimal values. For each of these set point changes, we notice a drop in the consumption of flotation gas. The results from the operation of the CFU are shown

in Figure 6.14 and are discussed below:

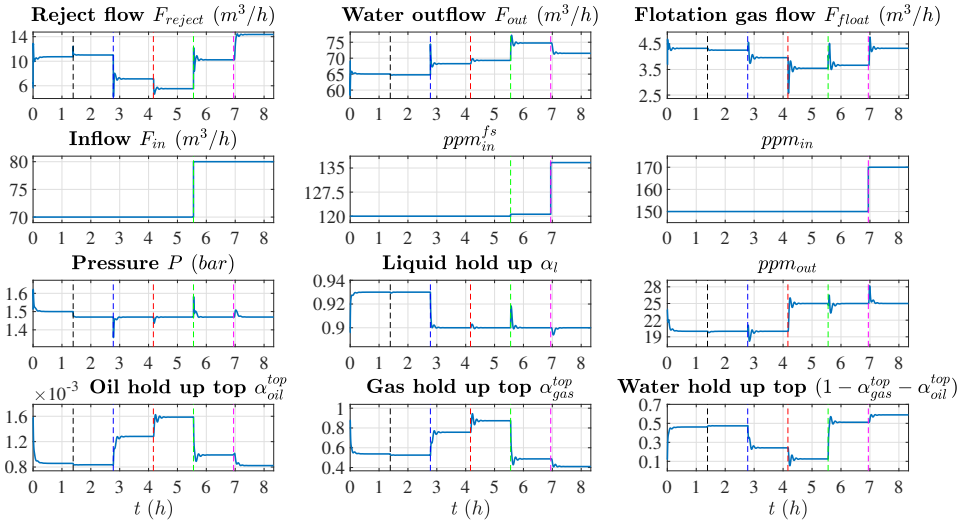


Figure 6.14: Operation of CFU with active constraint control. The first row of plots are manipulated variables, the second row of plots are disturbance variables, the third row plots are controlled variables and the fourth row of plots are other variables. The operation starts at  $t = 0$  with a sub-optimal operating point. The set-points for the controlled variables are changed to bring the system to optimal operation and the cost function - flotation gas flow - shows the benefits. The results also show the closed loop responses on the controlled variables and other important variables to changes in disturbance variables.

- **When pressure set point is reduced at 1.39 h:** The flotation gas is used more effectively as the volume of the flotation gas swells up at a reduced separator pressure according to (6.38). A reduced pressure results in more volumetric gas flow rate through the separator (for a given mass flow). As the bubble producing device produces bubbles with a fixed diameter, the increased flow rate will result in a higher free bubble number density and a better separation. The reject outflow is raised to purge the excess volume of the gas phase. As the reject flow carries additional water, the water outflow reduces in order to maintain the same liquid hold up in the separator. The additional water in the reject causes the oil and gas hold ups to reduce at the top.
- **When liquid hold up set point is reduced at 2.78 h:** The water outflow spikes up and settles at a higher value. A higher water outflow causes less water to exit the reject flow. A reduced liquid hold up provides excess space for the gas, leading to an intermittent drop in pressure, while a higher gas hold up in the system leads to an effective usage of flotation gas. Therefore, a reduced flotation gas inflow is necessary to meet the  $ppm_{out}$  set point. A higher gas hold up is also present in the top section, causing oil and water

hold ups at the top to drop. The reduction in flotation gas inflow causes an overall reduction in reject flow.

- **When  $ppm_{out}$  set point is raised at 4.17 h:** The flotation gas inflow reduces as the cleaning load is reduced. A reduced gas inflow causes pressure to drop transiently until it is recovered by the pressure controller. A higher  $ppm_{out}$  set point also causes a reduction in loss of water in the reject stream. Hence, at the top the hold up of water drops, while that of oil and gas rise. Overall, the reject flow reduces due to reduced water and gas flows in the reject stream.
- **Rejection of disturbance - inflow raised at 5.56 h:** The pressure spikes up causing the reject flow to be raised to maintain the pressure set point. A higher pressure in the transients make the gas occupy less volume, which results in liquid hold up rising transiently. The water outflow also rises to keep the liquid hold up at the set point as well as to compensate for the additional inflow. The oil concentration  $ppm_{in}^{fs}$  rises because at a higher flow, the swirl intensity increases causing an increase in the swirl split. In addition, because of a reduced residence time in CFU, keeping the  $ppm_{out}$  at the set point requires additional flotation gas. The ratio controller for  $ppm_{out}$  causes a quick rise in flotation gas proportional to the step in inflow, which results in a shorter spike in  $ppm_{out}$ . Because of an additional inflow, the water content in the reject increases, and at the same time the gas hold up and the oil hold up in the top fall.
- **Rejection of disturbance -  $ppm_{in}$  raised at 6.94 h:** The oil concentration  $ppm_{in}^{fs}$  rises. The  $ppm_{out}$  spikes up causing more flotation gas to be used due to automatic regulation of  $ppm_{out}$ . This also causes the pressure to spike up transiently, which is counteracted by an increase in reject flow. An increased reject flow causes a higher amount of water to escape through the reject stream. This leads to a higher water hold up at top causing the gas hold up and the oil hold up at the top to fall. Since the overall liquid hold up is regulated at a fixed set point, water outflow drops.

## 6.5 Discussion and future work

Several simplifying assumptions have been considered in this paper to develop a simplified CFU model. These assumptions are discussed below.

The bubble injection model assumes that the bubbles produced are of a specific uniform size, which depends on the design of the bubble producing device. Depending on the actual design, the bubble size will change with the pressure in the CFU, but we chose not to model this effect because we do not have any information about the details of such devices. Also, there will be a pressure gradient in the separator with higher pressure towards the bottom of the separator, which will cause the bubbles to slightly grow in size as they rise from the bottom of the separator. A larger bubble size may lead to a poorer separation efficiency as given by (6.4). The pressure difference between top and bottom of the separator is relatively small. Therefore, we have chosen not to include this effect in the model as its effect is relatively small in comparison to the effect that other modeling assumptions have.

We introduced a simple model - (6.1) - to describe the swirl effect in the CFU. For the parameters we have chosen, the swirl split has a minimum value of 0.8 at swirl intensity 0.7. These values can be considered tuning parameters, which can be adjusted to match operational data. Alternatively, if more information about a particular design were available, one could include a more detailed model of the swirl into the CFU model.

In the modeled CFU design, the inlet swirl separator is designed to promote separation and coalescence, such that the droplets exceeding a certain size will be separated and removed, while smaller droplets coalesce to form larger droplets that enter the flotation section. These two effects contribute to a narrow oil droplet size distribution that enters the flotation section. Based on this phenomenon, we chose to develop a model that assumes a single representative droplet size for all droplets. This representative droplet size need not necessarily be the mean of the true droplet size distribution, as it may be adjusted to match the model outlet purities to real data. This kind of approach is not uncommon for the design of systems with dispersed phases. Examples of such simplifications include the use of the Sauter mean diameter (Kowalczyk and Drzymala, 2016), or the use of mass median diameters, such as  $d_{50}$  (Neumann et al., 2003).

A distribution in oil droplet sizes as well as in bubble sizes could, however, be included in the model we have developed. For each additional droplet class, two additional equations for number densities - one for droplet and the other for loaded bubble - need to be considered for each control volume in the bottom section and the flotation section, whereas for each additional bubble class, two additional equations for number densities - one for free bubble and the other for loaded bubble - need to be considered for each control volume in flotation section. In the top section, the gas inflow from each free and loaded bubble class needs to be considered and oil inflow from each loaded bubble class needs to be considered. If distributions in both oil droplet and gas bubble sizes are considered, then the number of equations for number density of loaded bubbles will increase corresponding to each possible combination of individual droplet and individual bubble class. However, this would add significantly to the model complexity, and for the purposes of optimal operation and control (especially for finding active constraints), this is usually not necessary.

As mentioned above, the collision efficiency tuning parameter  $k$  can be used to describe the swirling turbulence effect that is not captured in the initial swirl separator model. It could also be adapted to account for un-modeled phenomena such as improved separation due to coalescence in the flotation section. By stacking several models of the type we have described, one can also describe more sophisticated designs, e.g. the ones by Schlumberger (Bhatnagar and Sverdrup, 2014; Maelum and Rabe, 2015), and by Siemens Water Technologies Corporation (Hayatdavoudi et al., 2011), where the flotation gas and the produced water enter the CFU together from the same inlet and the produced water goes through multiple stages of separation.

In this work, we did not have the possibility to validate the model against real data or a validated high-fidelity model. However, if operational data for a particular CFU design becomes available in future, this model can be used as a starting point and adapted to make it more representative of the real process. Also, it can be used in a design of experiments framework to determine good experiments that can be

used to either validate the model, or decide where it needs to be improved.

## 6.6 Conclusion

In this paper, a control oriented dynamic model for a compact flotation unit has been presented. To the authors' knowledge this is the first control-oriented model of a CFU that is available in the literature. The main motivation of the work is to understand the CFU flotation process from the point of view of control in order to develop a effective control scheme. An analysis of the model and its behavior under manual and automatic control has been presented. The model has been qualitatively verified for expected behavior. It has been shown that a simple PI based decentralized control structure can function well despite multi-variable couplings between the inputs and the outputs. Further, the model has been used to optimize the operating conditions. The optimal solution is found to lie at the boundary of the feasible region and has been implemented as active constraint control. Simulations have been performed starting at a suboptimal point and moving towards optimal operation. The changes in the disturbances were also handled effectively by the control structure, which ensured that the set points are maintained.

## Acknowledgements

The authors acknowledge funding from the [SUBPRO](#) (Subsea production and processing) center for research-based innovation and the Norwegian Research Council.



## Chapter 7

# Optimal operation of a subsea separation system consisting of a coalescence based gravity separator model and a produced water treatment

In this work, we develop a model for a gravity separator, and use it together with models from literature to study the control of a subsea separation system that separates oil, gas and water from well fluids in hydrocarbon production. Our separation system contains a gravity separator, hydrocyclones and compact flotation units. The main contributions of the paper are twofold. First, we present a coalescence based dynamic gravity separator model, which is able to predict oil concentration in water outlet and water concentration in oil outlet. Second, we study optimal operation of the overall separation system with an objective of maximizing water removal. We propose a simple control structure that operates the process close to optimally, by rejecting disturbances from upstream flows and maintaining a tight control of the quality of the purified water leaving the system.

*Revised version submitted for publication in Industrial & Engineering Chemistry Research, 2018*

### 7.1 Introduction

In the oil and gas industry, separation systems are used to separate hydrocarbons from undesirable components, such as water and sand, which are inevitably produced from wells along with the hydrocarbons. Poorly performing separation systems adversely affect the profitability of the hydrocarbon production system. Crude that contains a high water concentration sells at a lower price. Moreover, the transportation of a substandard crude with high water content through an

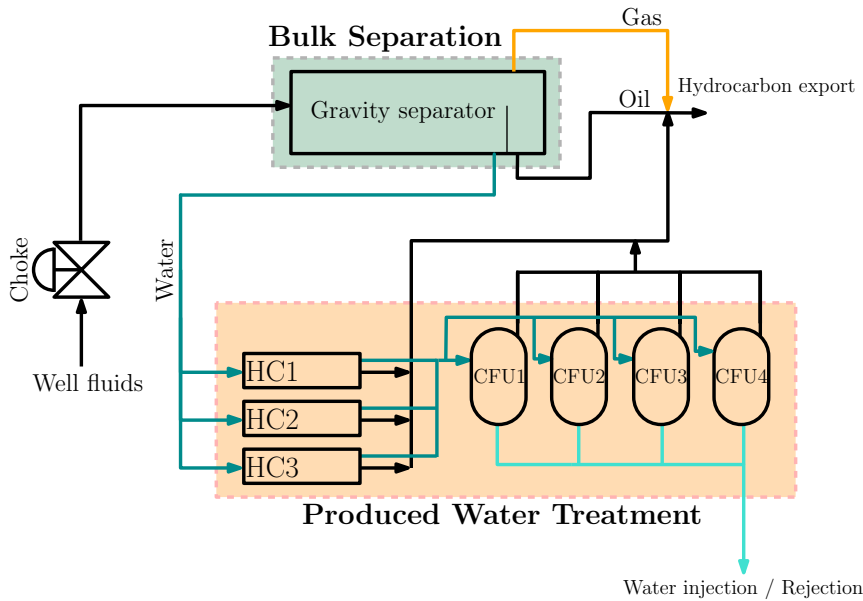


Figure 7.1: A subsea separation system composed of hydrocyclones (HC) and compact flotation units (CFU). The reject streams from HC and CFU are directed to hydrocarbon export line as slops or other facilities to process the rejects are typically not available subsea. In this figure, we do not show pumps for reject streams and for water injection.

export pipeline may lead to corrosion related damages to the pipeline (Brondelet et al., 1994). Water in the transport line may also give rise to issues with flow assurance in the riser, such as higher hydrostatic pressure drop and emulsion or hydrate formation.

Figure 7.1 shows a schematic of the separation system we will study further in this paper. This separation system consists of a bulk separation part, consisting of a gravity separator, and a produced water treatment part, consisting of three hydrocyclones (HC) and four compact flotation units (CFU). A real subsea separation system may follow a similar set-up, albeit with a different number of units, depending on the production rate, fluid properties and compositions (Orlowski et al., 2012). The main operational disturbances to a hydrocarbon separation system are changes in the inlet conditions to the bulk separation, such as pressure, and inflows and compositions of gas, oil and water. Any control structure that aims to operate the system optimally must handle these disturbances well, and consider the system as a whole, in order to account for the interactions between the different components.

Analyses of control of separation systems have often included the upstream processes. For example, (Yang et al., 2013, 2014, 2016) investigated plant-wide optimal control strategies to a real pilot scale separation system. Their system included a gravity separator and a deoiling hydrocyclone. In their work, they developed a con-

trol strategy to operate a combination of the two separators by controlling water level in the gravity separator and the pressure difference ratio (*PDR*) in the hydrocyclone to their reference values. The main contribution in terms of separation system operation was a unified way of tuning the two controllers so that they work together well.

(Ribeiro et al., 2016) implemented a model predictive controller (MPC) for set-point control of oil production rate, oil in water (OiW) outlet and water in oil (WiO) outlet from a gravity separator which receives feed from an upstream process of three gas-lifted wells and a riser. The case study is based on well data from Campos Basin field near Rio de Janeiro, Brazil, in which a real time optimization (RTO) layer finds optimal operating points, which are followed and further fine-tuned by the MPC layer. The model used to compute concentrations of oil in water and water in oil is based on polynomial correlations. The gas injection rates for the three wells and the separator water level were used as manipulated variables for the MPC. The results presented show that the controller reacts well to set-point changes and rejects disturbances effectively. The lowest level controllers are PID-controllers, which track the set-points given by the MPC layer.

To avoid the negative consequences of water in the transport system, it has been proposed to place separation systems close to the production site, and remove the water (Bringedal et al., 1999). This has resulted in several subsea separation facilities, where the separation equipment has been placed on the seabed; among them two facilities - Troll C (Baggs et al., 2000) and Tordis (Neuenkirchen, 2006; Gjerdseth et al., 2007) are in Norway. Besides water removal on the seabed, subsea separation has many other advantages. Some of them are increased production due to reduced backpressure on the reservoir, need for fewer flowlines/risers, reduced riser based slugging, reduced scaling and corrosion in flowlines and hydrate prevention (Bringedal et al., 1999).

In this paper, we study how to operate such a subsea separation system optimally. The two main contributions in this paper are: A dynamic model for a gravity separator that includes the droplet-droplet coalescence of droplets dispersed in the continuous phases in a simplified way, and a simple control structure that operates a separation system close to optimally using simple proportional-integral (PI) controllers. The proposed solution is easy to implement on the commonly used industrial control systems, and yields good performance in the presence of disturbances while adhering to important process constraints, such as on the water quality.

The problem of maximizing water removal in subsea separation systems has attracted very little attention in literature, especially using first principles models. Besides, in the literature for first-principles based gravity separator models, the phenomenon of droplet-droplet coalescence has either been neglected (Sayda and Taylor, 2007; Das et al., 2017; Backi and Skogestad, 2017) or modeled in an inadequate and complicated way (Backi et al., 2018). The droplet-droplet coalescence is an important phenomenon in the context of gravity separation (Frising et al., 2006) and the literature is lacking a simplified way to address it. In this paper, we fill these two gaps by presenting a control and optimization oriented model that includes coalescence inside the gravity separator, and using it together with other models from literature to study how to operate the overall system optimally.

This paper is organized as follows. The next section presents the coalescence driven gravity separator model that we developed. Thereafter, we present a section on optimal operation of our subsea separation system. Here we discuss a control structure design, and results from optimization and dynamic simulation of the system under disturbances. In the discussion section, we discuss our modeling assumptions and provide guidelines on how to include the effects that have been ignored in our work. In the final section, we conclude the paper with some final remarks.

## 7.2 Coalescence based gravity separator model

### 7.2.1 Process description

A schematic of a horizontal gravity separation process is shown in Figure 7.2, in which a horizontal cylindrical vessel is used to perform a bulk separation of well fluids into three phases - oil, gas and water. Gravity separators are quite large

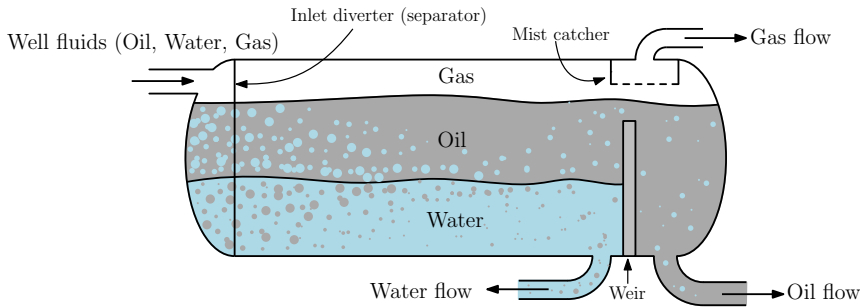


Figure 7.2: Schematic of a three phase gravity separator.

in size, such that they provide enough residence time for the phases to separate due to gravitational forces. At the inlet of the separator, a multiphase feed usually separates into two liquid layers - a continuous water layer at the bottom and a continuous oil layer above the water layer, and a gas phase on top. Within each layer, the difference in densities of the different phases causes the droplets of dispersed phase to sediment or rise. The oil dispersed in the continuous water phase rises and the water dispersed in continuous oil phase sediments. At the end of the separator, a weir plate separates the oil flow from the water flow. The water is removed from an outlet before the weir and the oil is removed from an outlet after the weir. The gas phase is removed from an outlet at the top, typically after a mist catcher.

Gravity separators are designed to facilitate the separation of the dispersed phase i.e. oil in water and water in oil from the respective continuous medium. Therefore, inside the separator, breakage of the dispersed droplets is sought to be minimized, while droplet-droplet coalescence, which makes droplets grow larger in size, is enhanced (Frising et al., 2006) because larger droplets rise or sediment faster than smaller ones. Once the droplets reach the oil-water interface, they merge

with their respective continuous medium. The nature of coalescence, either droplet-droplet or droplet-interface, is determined by the contact time between the coalescing entities and the rate of drainage of the thin film of the continuous phase in between the coalescing entities (Chesters, 1991; Liao and Lucas, 2010).

### Previous work in control-oriented gravity separator modeling

For the purpose of control, models that involve complex computational fluid dynamics (CFD) calculations (Hallanger et al., 1996; Hansen, 2001) are not useful because they are computationally too expensive. Likewise, models that describe the gravity separation phenomenon in a batch process (Jeelani and Hartland, 1985, 1993; Jeelani et al., 2005; Hartland and Jeelani, 1987) are not directly transferable to industrial-size separation system, such as the one studied in this paper.

There are a handful of works in control-oriented continuous gravity separator modeling. A simplified three phase separator model was developed by (Sayda and Taylor, 2007), in which they consider two lumped bulk liquid phases. Oil droplets of diameter  $500 \mu\text{m}$  are considered to be dispersed in the water phase at the start of the separator; these droplets separate from the water phase and move to the oil phase based on Stokes' law. The droplets that fail to move to the oil phase continue further into the water outflow. No dispersed water in the oil phase is considered. Vapor-liquid equilibrium is assumed at the oil surface using Raoult's law. Hence, the model can predict oil and gas fractions in the oil phase and oil, gas and water fractions in the water phase in a dynamic way.

(Backi and Skogestad, 2017) developed a dynamic gravity separator model considering a static distribution of droplet classes, ranging in size from  $50 \mu\text{m}$  to  $500 \mu\text{m}$ . These droplet classes are considered for the oil droplets dispersed in the water phase as well as the water droplets dispersed in the oil phase. All water droplets are considered to be located at the top edge of the oil phase whereas all oil droplets at the bottom edge of the water phase at the start of the separator. The oil and water phases are horizontally distributed into five control volumes. In order to calculate the droplet distribution out of each control volume, a comparison is made between horizontal residence time and vertical residence time of a droplet within the control volume, where the vertical residence time is calculated using Stokes' law. The vertical position of a droplet out of a control volume determines if the droplet merges with its continuous phase or proceeds further horizontally. No coalescence or breakage of the droplets is considered. The results show dynamic changes in the droplet distribution in the two continuous phases at the separator outlet under changes in water level set-point. This model was extended by (Backi et al., 2018) by considering population balance equations to determine the precise droplet distribution entering the separator. The population balances, which consider both the coalescence and the breakage phenomena, are implemented on only a small control volume just before the first of the five main control volumes, thereby ignoring the coalescence or the breakage phenomena in those five control volumes.

(Das et al., 2017) developed a simplified gravity separator model based on a three layer approximation, where an additional layer called dense-packed layer or emulsion layer is added in between the water and the oil layers (Arntzen, 2001). The other models discussed above do not consider this third layer. This layer exists

due to surface properties imparted by some of the chemicals, such as asphaltenes present in certain crude oils, which hinder the separation process (Spiecker et al., 2003; Kokal, 2005; Dudek et al., 2017). This model considers three lumped layers with no spacial distribution and can describe the oil fraction in all these layers dynamically.

None of the models described above considers coalescence of droplets inside the gravity separator. In this paper, we fill the gap of a simplified dynamic model for gravity separator that includes the important phenomenon of dispersed phase coalescence inside the gravity separator in a simplified way.

## 7.2.2 Model description

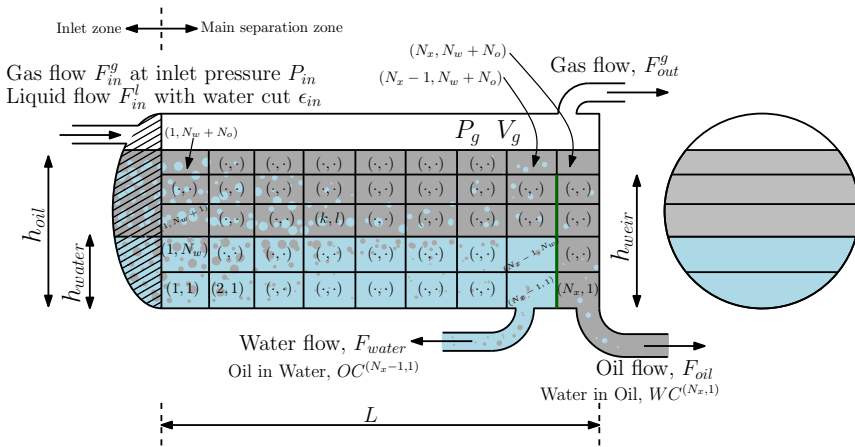


Figure 7.3: Three phase gravity separator divided into control volumes  $V^{k,l}$ . The control volumes are indexed by  $(k, l)$ , where  $k$  spans from  $k = 1$  to  $N_x$  traveling from left to right, while  $l$  spans from  $l = 1$  to  $(N_w + N_o)$ , traveling from bottom to top. In this figure, we have  $N_x = 9, N_w = 2$  and  $N_o = 3$ .

Figure 7.3 shows a schematic of our proposed model and its different elements. The model considers two zones - an inlet zone and a main separation zone. In the inlet zone, an initial separation of the fluids into two bulk layers happens, whereas in the main separation zone the sedimentation of the water droplets in the continuous oil layer and the creaming of the oil droplets in the continuous water layer happens. When the dispersed droplets reach the interface, they merge with their respective continuous phase by crossing the oil-water interface. At the end of the main separation zone, the water layer with the remaining oil dispersed in it adjacent to the weir exits the water outlet of the separator. The oil with remaining dispersed water above the interface and just left of weir goes over the weir and is collected from the oil outlet.

### Inlet zone

It is assumed that an initial instantaneous separation of the fully mixed multiphase flow happens in the inlet zone of the separator, shown by the area in rising tiling pattern in Figure 7.3. Due to the initial separation, a fraction  $\gamma_w$  of net water inflow to the separator enters the continuous water layer. Likewise, a fraction  $\gamma_o$  of net oil inflow to the separator enters the continuous oil layer, as is also assumed by (Backi and Skogestad, 2017). The rest of the oil remains dispersed in the water layer and enters the main separation zone. Similarly, the water that does not form the continuous water phase remains dispersed in the continuous oil layer and enters the main separation zone.

### Control volumes

To derive the model, the main separation zone is divided into several control volumes indexed by  $(k, l)$  as shown in Figure 7.3. The discretization we use ensures that the oil-water interface is not inside a control volume. The water layer, i.e. the volume of liquid below the oil-water interface is divided into  $(N_x - 1)$  equally spaced horizontal sections and  $N_w$  equally spaced vertical sections, leading to  $N_w(N_x - 1)$  control volumes. A part of the oil layer (the liquid volume above the oil-water interface) that is below the weir height, and left of the weir is divided into  $(N_x - 1)$  equally spaced horizontal sections and  $(N_o - 1)$  equally spaced vertical sections, leading to  $(N_o - 1)(N_x - 1)$  more control volumes. There is one vertical section and  $(N_x - 1)$  equally spaced horizontal sections for the part of the oil layer above the weir height and to the left of the weir plate, which lead to  $(N_x - 1)$  more control volumes. On the right side of weir, there is one horizontal section and  $(N_w + N_o)$  vertical sections. Therefore, we consider a total of  $N_x(N_w + N_o)$  control volumes in our model. The volume of control volume  $(k, l)$  is denoted by  $V^{(k, l)}$ .

Figure 7.3 also introduces some important notation:  $F_{in}^g$  denotes inlet gas flow,  $P_{in}$  inlet pressure,  $F_{in}^l$  inlet liquid flow,  $\epsilon_{in}$  inlet water cut in the liquid flow,  $F_{out}^g$  gas outflow,  $F_{oil}$  oil outflow right of weir,  $h_{oil}$  total liquid level,  $h_{water}$  water level,  $WC^{(N_x, 1)}$  water cut in oil outflow,  $F_{water}$  water outflow left of weir,  $OC^{(N_x - 1, 1)}$  oil cut in the water outflow,  $P_g$  separator pressure as well as the outlet gas pressure,  $V_g$  the volume available for gas phase above the liquid volume,  $h_{oil}$  oil level or total liquid level and  $h_{water}$  water level. The separator volume is assumed to be a perfect cylinder, and all water and oil cuts and fractions are volumetric, if not stated otherwise.

### Flows through control volume boundaries

We assume that the flows above and below the oil-water interface can be described as independent plug flows, largely given by the outflows  $F_{oil}$  and  $F_{water}$ , respectively. To obtain the horizontal flow out of the right edge of a control volume, the total flow out of the layer in which the control volume exists is scaled by the cross-sectional area of the control volume normal to the direction of horizontal flow. The horizontal flow out of the right edge of a control volume is then back propagated to find the inflow from the left edge of the same control volume such that the total inflow to the control volume equals the total outflow from the control volume. A

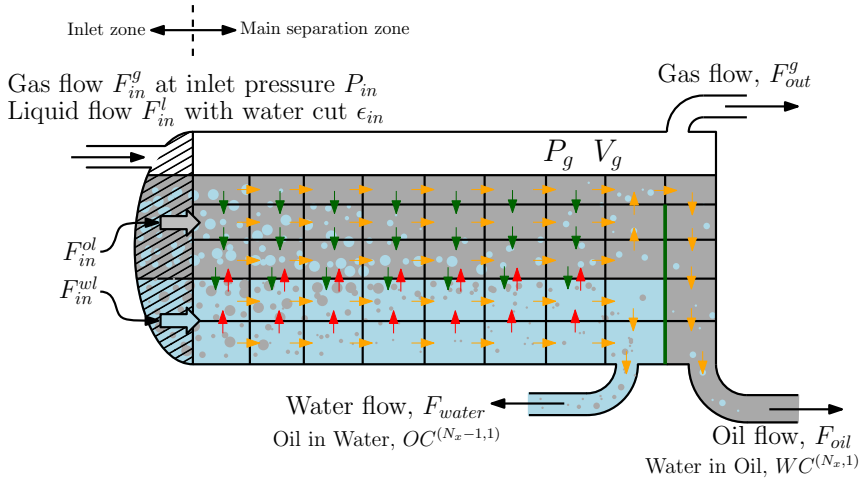


Figure 7.4: Flows for each control volume in the gravity separator model. Convective flows (due to bulk motion) are colored in orange. Non-convective (buoyancy-driven) water flows are colored in green. Non-convective (buoyancy-driven) oil flows are colored in red.

special scenario occurs when the oil outflow  $F_{oil}$  is lower than the downward flow through interface, this will lead to a flow in backward direction (or an outflow from the left side), also known in this work as back flow.

The modeled flows are illustrated in Figure 7.4. We denote convective flows as the mass transport due to the bulk movement, while the flows driven by buoyancy are referenced to as non-convective flows. For the control volumes  $(1, 1 \dots (N_w + N_o))$ , i.e the ones on the most left and adjacent to the inlet zone, the inflows from the left edge are decided by the liquid inflows to the separator. The flow entering the oil layer  $F_{in}^{ol}$  and the water layer  $F_{in}^{wl}$  are

$$F_{in}^{ol} = \gamma_o(1 - \epsilon_{in})F_{in}^l + (1 - \gamma_w)\epsilon_{in}F_{in}^l, \quad (7.1)$$

and

$$F_{in}^{wl} = \gamma_w\epsilon_{in}F_{in}^l + (1 - \gamma_o)(1 - \epsilon_{in})F_{in}^l. \quad (7.2)$$

These flows are scaled by the cross-sectional area of the control volumes normal to the direction of horizontal flow to obtain the inflows on the left edges of each of the control volumes  $(1, 1 \dots (N_w + N_o))$ . The convective flows out of the right edge of the control volumes just left of the weir are considered zero. The convective flows out of these control volumes are directed downwards if the fluid is below the oil-water interface and upwards otherwise.

The settling velocity of droplets in gravity separators is usually described by the Stokes' law, which gives the terminal velocity of the dispersed phase relative to the continuous phase in or away from the direction of gravity based on whether the dispersed phase is heavier or lighter than the continuous phase, respectively.

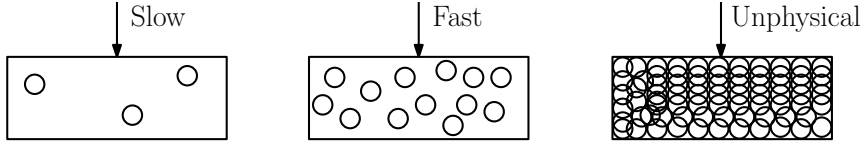


Figure 7.5: Scenarios faced by sedimenting water droplets while entering a control volume.

Terminal velocity  $v_s$  from Stokes' law is

$$v_s = \frac{\Delta\rho g d^2}{18\mu}, \quad (7.3)$$

where  $g$  denotes the acceleration due to gravity,  $d$  the diameter of the dispersed phase droplet,  $\Delta\rho$  the difference between the densities of the dispersed phase and the continuous phase and  $\mu$  the viscosity of the continuous phase. From this expression, it is clear that a higher  $\Delta\rho$ , a larger  $d$  and a smaller  $\mu$  are favorable for a fast separation. In particular, the diameter of the droplets significantly affects the velocity due to the quadratic term in (7.3), which makes the droplet-droplet coalescence an important phenomenon in a gravity separator. The terminal velocity given by Stokes' law (7.3) is valid for one single droplet in an infinite continuum, which is not the case in this model. There are often other dispersed phase droplets in the vicinity. Especially for a control volume in the oil layer at the interface, the flow of the water droplets crossing the top edge of the control volume downwards is given by the area of downward transfer multiplied by terminal velocity of dispersed water. If we consider a control volume in the oil layer near the oil-water interface, e.g.  $(k, N_w + 1)$  and the mass transfer of water through the interface is low or hindered and we use (7.3) to compute non-convective flow of water downwards at the top edge, it is possible that the water content in this control volume surpasses 1, which is unphysical (shown in Figure 7.5).

A similar situation can occur in the control volumes just below the oil-water interface, in which the oil content in those control volumes surpasses 1. To avoid these unphysical scenarios, we adapted the Stokes' equation as

$$v_a = \begin{cases} v^s \left( \frac{WC_p - WC_{receiver}}{WC_p} \right) & \text{for Water in Oil} \\ v^s \left( \frac{OC_p - OC_{receiver}}{OC_p} \right) & \text{for Oil in Water} \end{cases}, \quad (7.4)$$

where  $v_a$  denotes the adapted terminal velocity, and  $WC_{receiver}$  and  $OC_{receiver}$  water cut in a control volume in the oil layer and oil cut in a control volume in the water layer, respectively.  $WC_p$  denotes phase inversion point in terms of water cut and  $OC_p$  in terms of oil cut. The adapted terminal velocity  $v_a$  for droplets moving out of a control volume  $(k, l)$  is denoted by  $v_a^{(k, l)}$ . The key consideration in this adaptation is that a higher dispersed phase content in a control volume results in a lower non-convective flow entering that control volume. Thereby, a higher water cut in a control volume in the oil layer will have a lower non-convective flow of dispersed water droplets entering that control volume.

### Number densities of droplet classes

There are  $N_d$  droplet classes considered in the model. The droplet classes are identified by subscript  $i$ . These classes are chosen such that the droplet volume of these classes are integer multiples of the droplet volume of the smallest base class  $i = 1$ , which has a droplet diameter  $d_A$  and volume  $V_A = \left(\frac{\pi d_A^3}{6}\right)$ . This choice is governed by the idea that droplets coalesce with other droplets to become larger droplets that will have volumes in multiples of the volume of a droplet in the base class  $i = 1$ . The droplet class  $i$  indicates that the volume of a droplet in that class is  $iV_A$  and thereby, the diameter of droplets in that droplet class is  $d_A \sqrt[3]{i}$ . The dispersed phases entering control volumes  $(1, l)$  are assumed to consist of droplets of the smallest size  $d_A$  i.e. only of droplet class  $i = 1$  for both oil dispersed in water and water dispersed in oil.

To keep notation light, we use the subscript  $i$  to denote the droplet classes in both continuous phases, that is in the oil layer, the subscript  $i$  denotes droplet class for droplets of water, whereas in the water layer, it denotes the droplet class for droplets of oil. The total number of droplets of class  $i$  in control volume  $(k, l)$  is given by  $N_i^{(k, l)}$ . The corresponding number density of that droplet class in the control volume is calculated by dividing the densities of the droplets by the volume of the control volume as  $n_i^{(k, l)} = \frac{N_i^{(k, l)}}{V^{(k, l)}}$ . The partial density is defined as

$$\rho_i^{(k, l)} = \rho_d n_i^{(k, l)} (iV_A), \quad (7.5)$$

where  $\rho_d$  is the density of the dispersed phase, which is either pure water phase density  $\rho_w$  or pure oil phase density  $\rho_o$ . The total partial density of a dispersed phase in a control volume can be given as a summation of the partial densities for the  $N_d$  droplet classes by

$$\rho_d^{(k, l)} = \sum_{i=1}^{i=N_d} \rho_i^{(k, l)}, \quad (7.6)$$

where the subscript  $d$  denotes the dispersed phase, either water in the continuous oil layer or oil in the continuous water layer. The vector of stacked number densities for different droplet size classes starting from the smallest to the largest class is denoted by  $\bar{n}^{(k, l)}$  and the same for partial densities by  $\bar{\rho}^{(k, l)}$ . The volume fraction of the dispersed phase in a control volume is

$$\epsilon_d^{(k, l)} = \frac{\rho_d^{(k, l)}}{\rho_d}. \quad (7.7)$$

Hence, water cut in any control volume in the oil layer is given by

$$WC^{(k, l)} = \frac{\rho_w^{(k, l)}}{\rho_w}, \quad (7.8)$$

and oil cut in any control volume in the water layer is given by

$$OC^{(k, l)} = \frac{\rho_o^{(k, l)}}{\rho_o}. \quad (7.9)$$

### Droplet-droplet coalescence

The droplet-droplet coalescence is modeled using a set of  $N_{reaction}$  reactions in order to result in  $N_d$  droplet size classes. The reactions are shown below with each reaction being identified by a subscript  $j$ . The reactions can be expressed in a general form in volume terms with species expressed as multiples of  $V_A$  as



where,

$$\{\alpha, \beta : \alpha, \beta \in [1, \dots, (N_d - 1)], (\alpha + \beta) \leq N_d\} \quad (7.11)$$

The reaction rate  $r_j$  for reaction  $j$  is given by

$$r_j = k_d n_\alpha^{(k,l)} n_\beta^{(k,l)}, \quad (7.12)$$

where the unit of reaction rates is  $\left[\frac{1}{m^3 s}\right]$ ,  $\alpha$  and  $\beta$  both are one of the droplet classes. For simplicity, we assume that the droplet-droplet coalescence reaction rate constants  $k_d$  are same for all the reactions, irrespective of whether the dispersed phase is oil in water or water in oil, but this assumption can be relaxed if necessary. The parameter  $k_d$  has a unit of  $\left[\frac{m^3}{s}\right]$ . The rates for these  $N_{reaction}$  reactions stacked in a  $N_{reaction} \times 1$  vector of reaction rates is denoted by  $\bar{r}$ . The stoichiometry for the reactions of the  $N_d$  droplet classes is stored in a  $N_d \times N_{reaction}$  stoichiometric matrix  $S$  using (7.10).

### Droplet-Interface coalescence

The water droplets in the oil layer just above the oil-water interface can merge with the continuous water layer, whereas the oil droplets in the water layer just below the oil-water interface can merge with the continuous oil layer. We assume that there is no backmixing through the interface, i.e. once a water droplet has entered the continuous water phase, it remains there. Similarly, once an oil droplet enters the continuous oil phase, it stays there. Assuming incompressible liquids, we calculate the mass transfer (in volumetric terms) through the interface as

$$q_{w,int,\downarrow}^{(k,l)} = k_w^{int} A_{int}^{(k,l)} WC^{(k,l)}, \quad (7.13)$$

and

$$q_{o,int,\uparrow}^{(k,l)} = k_o^{int} A_{int}^{(k,l)} OC^{(k,l)}, \quad (7.14)$$

where,  $q_{w,int,\downarrow}^{(k,l)}$  denotes water flow from control volume  $(k,l)$  across the interface downwards into the continuous water layer. Similarly,  $q_{o,int,\uparrow}^{(k,l)}$  denotes oil flow from control volume  $(k,l)$  across the interface upwards into the continuous oil layer. The terms  $k_w^{int}$  and  $k_o^{int}$  denote mass transfer coefficients with units  $[m/s]$ , and  $A_{int}^{(k,l)}$  the interfacial area that is part of the oil-water interface associated with the control volume  $(k,l)$ . The net transfer of mass through the interface is  $\left(q_{w,int,\downarrow}^{(k,l)} - q_{o,int,\uparrow}^{(k,l)}\right)$  in the downward direction or  $\left(q_{o,int,\uparrow}^{(k,l)} - q_{w,int,\downarrow}^{(k,l)}\right)$  in the upward direction.

### Mass balances for dispersed phases

A mass balance for mass of droplets of a droplet class  $i$  in a control volume  $(k, l)$  is

$$\frac{dm_i^{(k,l)}}{dt} = \dot{m}_{i,in}^{(k,l)} - \dot{m}_{i,out}^{(k,l)} + \dot{m}_{i,gen}^{(k,l)} - \dot{m}_{i,cons}^{(k,l)}, \quad (7.15)$$

where,  $\dot{m}_{i,in}^{(k,l)}$  denotes the inflow of mass of droplets in class  $i$  into control volume  $(k, l)$ ,  $\dot{m}_{i,out}^{(k,l)}$  outflow of mass of droplets in class  $i$  from control volume  $(k, l)$ ,  $\dot{m}_{i,gen}^{(k,l)}$  rate of gain of mass due to generation of droplets in class  $i$  in control volume  $(k, l)$  and  $\dot{m}_{i,cons}^{(k,l)}$  rate of loss of mass due to consumption of droplets in class  $i$  in control volume  $(k, l)$ . The generation and the consumption terms are due to coalescence, whereas inflow and outflow terms appear due to convective flow in the horizontal or vertical direction and non-convective flow in the vertical direction due to Stokes' law. Combining (7.15) for all the droplet classes in a vector, we obtain the mass balance of the dispersed phase in control volume  $(k, l)$  as

$$\frac{d\bar{m}^{(k,l)}}{dt} = \dot{\bar{m}}_{in}^{(k,l)} - \dot{\bar{m}}_{out}^{(k,l)} + \dot{\bar{m}}_{gen}^{(k,l)} - \dot{\bar{m}}_{cons}^{(k,l)}, \quad (7.16)$$

### Partial densities of dispersed phase droplet classes

The left hand side of (7.16) can be rewritten as

$$\frac{d\bar{m}^{(k,l)}}{dt} = V^{(k,l)} \frac{d\bar{\rho}^{(k,l)}}{dt} + \bar{\rho}^{(k,l)} \frac{dV^{(k,l)}}{dt}, \quad (7.17)$$

which is used to rewrite (7.16) as

$$\frac{d\bar{\rho}^{(k,l)}}{dt} = \frac{1}{V^{(k,l)}} \left( \dot{\bar{m}}_{in}^{(k,l)} - \dot{\bar{m}}_{out}^{(k,l)} + \dot{\bar{m}}_{gen}^{(k,l)} - \dot{\bar{m}}_{cons}^{(k,l)} - \bar{\rho}^{(k,l)} \frac{dV^{(k,l)}}{dt} \right). \quad (7.18)$$

As inflow  $\dot{\bar{m}}_{in}^{(k,l)}$  and outflow  $\dot{\bar{m}}_{out}^{(k,l)}$  are both made up of convective and non-convective flows, we can expand the expressions for the net flows as

$$\dot{\bar{m}}_{in}^{(k,l)} - \dot{\bar{m}}_{out}^{(k,l)} = \left( \dot{\bar{m}}_{in,conv}^{(k,l)} + \dot{\bar{m}}_{in,non-conv}^{(k,l)} \right) - \left( \dot{\bar{m}}_{out,conv}^{(k,l)} + \dot{\bar{m}}_{out,non-conv}^{(k,l)} \right) \quad (7.19)$$

$$= \left( \dot{\bar{m}}_{in,conv}^{(k,l)} - \dot{\bar{m}}_{out,conv}^{(k,l)} \right) + \left( \dot{\bar{m}}_{in,non-conv}^{(k,l)} - \dot{\bar{m}}_{out,non-conv}^{(k,l)} \right) \quad (7.20)$$

$$= \Delta \dot{\bar{m}}_{conv}^{(k,l)} + \Delta \dot{\bar{m}}_{non-conv}^{(k,l)} \quad (7.21)$$

Similarly, the terms  $\dot{\bar{m}}_{gen}^{(k,l)}$  and  $\dot{\bar{m}}_{cons}^{(k,l)}$  can be related to the coalescence reaction rates as

$$\left( \dot{\bar{m}}_{gen}^{(k,l)} - \dot{\bar{m}}_{cons}^{(k,l)} \right) = (\rho_d V_A) \mathbb{1} \circ \left( S\bar{r}V^{(k,l)} \right) = R^{(k,l)}, \quad (7.22)$$

where  $R^{(k,l)}$  is the rate of gain of mass due to coalescence reactions in control volume  $(k, l)$  for all droplet classes stacked in a vector, and  $\mathbb{1} = [1, 2, \dots, N_d]^T$ . Here, the operator  $\circ$  denotes element wise multiplication of matrices.



For the bottom-most control volumes, the term

$$\Delta \dot{m}_{non-conv}^{(k,l)} = -\bar{\rho}^{(k,l)} v_a^{(k,l)} A_{top}^{(k,l)}, \quad (7.27)$$

where  $A_{top}^{(k,l)}$  denotes the area of the top surface of the control volume  $(k,l)$ . This surface is the surface through which the droplets of oil travel upwards. There is no positive contribution in  $\Delta \dot{m}_{non-conv}^{(k,l)}$  because the bottom surfaces of the control volumes are the separator bottom. For the control volumes that are not at the separator bottom, the term

$$\Delta \dot{m}_{non-conv}^{(k,l)} = \bar{\rho}^{(k,l-1)} v_a^{(k,l-1)} A_{top}^{(k,l-1)} - \bar{\rho}^{(k,l)} v_a^{(k,l)} A_{top}^{(k,l)}. \quad (7.28)$$

**For control volumes**  $(1 \dots (N_x - 2), N_w)$  (Region II in Figure 7.6):  $\Delta \dot{m}_{conv}^{(k,l)}$  is identical to that in (7.26), while the term

$$\Delta \dot{m}_{non-conv}^{(k,l)} = \bar{\rho}^{(k,l-1)} v_a^{(k,l-1)} A_{top}^{(k,l-1)} - \rho_o q_{o,int,\uparrow}^{(k,l)}. \quad (7.29)$$

**For control volumes**  $(1 \dots (N_x - 2), (N_w + 1))$  (Region III in Figure 7.6): The term

$$\Delta \dot{m}_{conv}^{(k,l)} = \bar{\rho}^{(k-1,l)} q_{x,left}^{(k,l)} - \bar{\rho}^{(k,l)} q_{x,right}^{(k,l)}, \quad (7.30)$$

where  $q_{x,left}^{(k,l)}$  for control volume  $(1, N_w + 1)$  is  $F_{in}^{ol}$  scaled to the area corresponding to the control volume. An adaptation similar to that in (7.26) is also valid for (7.30) to account for backflow in the oil layer. The term  $\bar{\rho}^{(k-1,l)}$  for control volume  $(1, N_w + 1)$  is the partial density vector in the feed. The feed flow to the oil layer has a water volume fraction of

$$\epsilon_{in}^{ol} = \frac{(1 - \gamma_w) \epsilon_{in} F_{in}^l}{\gamma_o (1 - \epsilon_{in}) F_{in}^l + (1 - \gamma_w) \epsilon_{in} F_{in}^l}. \quad (7.31)$$

The term

$$\Delta \dot{m}_{non-conv}^{(k,l)} = \bar{\rho}^{(k,l+1)} v_a^{(k,l+1)} A_{top}^{(k,l)} - \rho_w q_{w,int,\downarrow}^{(k,l)}. \quad (7.32)$$

**For control volumes**  $(1 \dots (N_x - 2), (N_w + 2) \dots (N_w + N_o - 1))$  (Region IV in Figure 7.6): The term  $\Delta \dot{m}_{conv}^{(k,l)}$  is identical to that in (7.30). The term

$$\Delta \dot{m}_{non-conv}^{(k,l)} = \bar{\rho}^{(k,l+1)} v_a^{(k,l+1)} A_{top}^{(k,l)} - \bar{\rho}^{(k,l)} v_a^{(k,l)} A_{top}^{(k,l-1)}. \quad (7.33)$$

**For control volumes**  $(1 \dots (N_x - 2), (N_w + N_o))$  (Region V in Figure 7.6): The term  $\Delta \dot{m}_{conv}^{(k,l)}$  is identical to that in (7.30). The term

$$\Delta \dot{m}_{non-conv}^{(k,l)} = -\bar{\rho}^{(k,l)} v_a^{(k,l)} A_{top}^{(k,l-1)}, \quad (7.34)$$

where there is no positive contribution in  $\Delta \dot{m}_{non-conv}^{(k,l)}$  because the top surfaces of the control volumes have no water droplets traveling downwards from the top.

**For control volumes**  $((N_x - 1), 1 \dots (N_w + N_o))$  (Region VI in Figure 7.6): All entries in  $\Delta \dot{m}_{non-conv}^{(k,l)}$  are assumed 0 as non-convective flows are negligible close to

the weir as fluids have much larger vertical convective flows in directions opposite to the non-convective flows. The term

$$\Delta \dot{m}_{conv}^{(N_x-1,l)} = \bar{\rho}^{(N_x-2,l)} q_{x,left}^{(N_x-1,l)} + \bar{\rho}^{(N_x-1,l+1)} q_{x,top}^{(N_x-1,l)} - \bar{\rho}^{(N_x-1,l)} q_{x,bottom}^{(N_x-1,l)}, \quad (7.35)$$

for all  $l \in [1 \dots (N_w - 1)]$ , where  $q_{x,top}^{(N_x-1,l)}$  and  $q_{x,bottom}^{(N_x-1,l)}$  denote top and bottom flows downwards, respectively. The term  $q_{x,bottom}^{(N_x-1,l)}$  for  $l = 1$  is  $F_{water}$ . The term

$$\Delta \dot{m}_{conv}^{(N_x-1,N_w)} = \bar{\rho}^{(N_x-2,N_w)} q_{x,left}^{(N_x-1,N_w)} - \bar{\rho}^{(N_x-1,N_w)} q_{x,bottom}^{(N_x-1,N_w)}. \quad (7.36)$$

In the oil layer,  $q_{x,top}^{(N_x-1,l)}$  and  $q_{x,bottom}^{(N_x-1,l)}$  flows are upwards. The terms

$$\Delta \dot{m}_{conv}^{(N_x-1,N_w+1)} = \bar{\rho}^{(N_x-2,N_w+1)} q_{x,left}^{(N_x-1,N_w+1)} - \bar{\rho}^{(N_x-1,N_w+1)} q_{x,top}^{(N_x-1,N_w+1)}, \quad (7.37)$$

$$\Delta \dot{m}_{conv}^{(N_x-1,l)} = \bar{\rho}^{(N_x-2,l)} q_{x,left}^{(N_x-1,l)} + \bar{\rho}^{(N_x-1,l-1)} q_{x,bottom}^{(N_x-1,l)} - \bar{\rho}^{(N_x-1,l)} q_{x,top}^{(N_x-1,l)}, \quad (7.38)$$

for all  $l \in [(N_w + 2) \dots (N_w + N_o - 1)]$ , and

$$\begin{aligned} \Delta \dot{m}_{conv}^{(N_x-1,N_w+N_o)} &= \bar{\rho}^{(N_x-2,N_w+N_o)} q_{x,left}^{(N_x-1,N_w+N_o)} + \bar{\rho}^{(N_x-1,N_w+N_o-1)} q_{x,bottom}^{(N_x-1,N_w+N_o)} \\ &\quad - \bar{\rho}^{(N_x-1,N_w+N_o)} F_{oil}. \end{aligned} \quad (7.39)$$

**For control volumes**  $(N_x, 1 \dots (N_w + N_o))$  (Region VII in Figure 7.6): All entries in  $\Delta \dot{m}_{non-conv}^{(k,l)}$  are 0. For control volume  $(N_x, N_w + N_o)$ , the term

$$\Delta \dot{m}_{conv}^{(k,l)} = \bar{\rho}^{(k-1,l)} F_{oil} - \bar{\rho}^{(k,l)} F_{oil}, \quad (7.40)$$

and for control volume  $(N_x, 1 \dots (N_w + N_o - 1))$ , the term

$$\Delta \dot{m}_{conv}^{(k,l)} = \bar{\rho}^{(k,l+1)} F_{oil} - \bar{\rho}^{(k,l)} F_{oil}. \quad (7.41)$$

### Oil level

For the oil level equation, we write a mass balance for the total liquids in the separator. Since we consider the liquids incompressible i.e. liquid volume is conserved, a mass balance equation can be replaced by an equation for rate of change of liquid volume  $V_l$  as

$$\frac{dV_l}{dt} = F_{in}^l - F_{water} - F_{oil}. \quad (7.42)$$

Using trigonometric relations for the cylindrical geometry of the separator, a relationship between the liquid volume and the oil level can be established as

$$\frac{dh_{oil}}{dt} = \frac{1}{2L\sqrt{h_{oil}(2r - h_{oil})}} \frac{dV_l}{dt} = \frac{F_{in}^l - F_{water} - F_{oil}}{2L\sqrt{h_{oil}(2r - h_{oil})}}, \quad (7.43)$$

where  $r$  denotes the radius of the separator and  $L$  the length of the separator.

### Water level

An approach similar to that for the oil level equation can be applied to obtain the water level equation. The rate of change of water layer volume  $V_w$  is expressed as

$$\frac{dV_w}{dt} = F_{in}^{wl} - F_{water} + \left( q_{w,int,\downarrow}^{(k,l)} - q_{o,int,\uparrow}^{(k,l)} \right), \quad (7.44)$$

which can be reformulated as

$$\frac{dh_{water}}{dt} = \frac{F_{in}^{wl} - F_{water} + q_{w,int,\downarrow}^{(k,l)} - q_{o,int,\uparrow}^{(k,l)}}{2L \left( \frac{N_x - 1}{N_x} \right) \sqrt{h_{water} (2r - h_{water})}} \quad (7.45)$$

assuming a perfectly cylindrical tank. Since the separator length for water level calculation is on the left of the weir, the length  $L$  has been shortened by one control volume length using the factor  $\left( \frac{N_x - 1}{N_x} \right)$ .

### Pressure

We assume that the gas phase flashes out completely at the inlet part of the separator. A balance on moles of gas  $n_g$  inside the separator reads

$$\frac{dn_g}{dt} = \dot{n}_g^{in} - \dot{n}_g^{out}. \quad (7.46)$$

Employing the ideal gas law, we obtain

$$\frac{d}{dt} \left( \frac{P_g V_g}{R_g T} \right) = \left( \frac{P_{in} F_{in}^g}{R_g T} \right) - \left( \frac{P_g F_{out}^g}{R_g T} \right), \quad (7.47)$$

where  $R_g$  denotes the universal gas constant and  $T$  temperature. Since  $R_g$  and  $T$  are assumed to be constant, this simplifies to

$$\frac{d(P_g V_g)}{dt} = (P_{in} F_{in}^g - P_g F_{out}^g). \quad (7.48)$$

By applying chain rule to the left hand side, we get

$$V_g \frac{dP_g}{dt} + P_g \frac{dV_g}{dt} = (P_{in} F_{in}^g - P_g F_{out}^g), \quad (7.49)$$

Since the total separator volume,  $V_{sep} = V_l + V_g$ , is constant, we have  $\frac{dV_g}{dt} = -\frac{dV_l}{dt}$ . Inserting this relationship, we obtain

$$\frac{dP_g}{dt} = \frac{1}{V_g} \left( P_{in} F_{in}^g - P_g F_{out}^g + P_g \frac{dV_l}{dt} \right), \quad (7.50)$$

which when reformulated using (7.42), gives

$$\frac{dP_g}{dt} = \frac{1}{V_g} \left( P_{in} F_{in}^g - P_g F_{out}^g + P_g \left( F_{in}^l - F_{water} - F_{oil} \right) \right). \quad (7.51)$$

## 7.3 Optimal operation of a subsea separation system

### 7.3.1 Separation system overview

In this work, we consider a subsea separation system as shown in Figure 7.7.

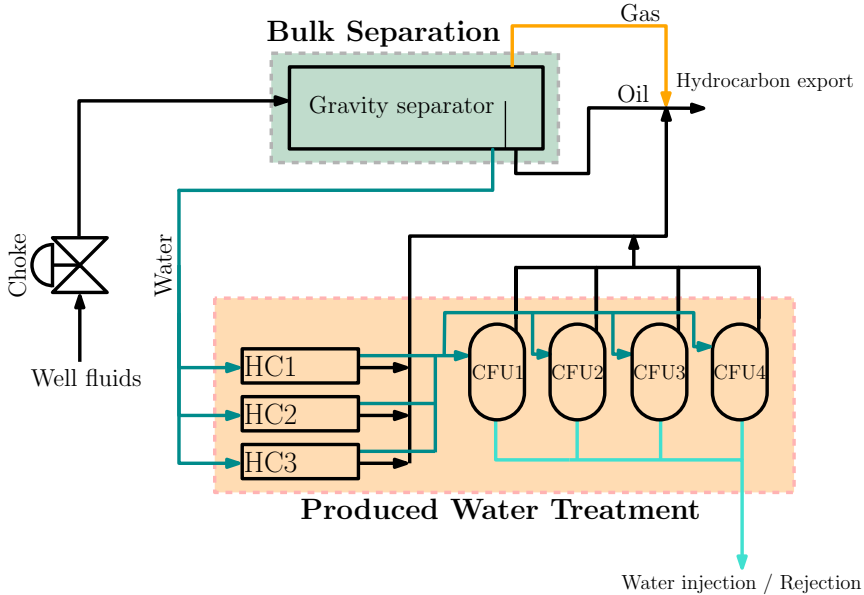


Figure 7.7: Our simulated subsea separation system.

The well stream containing water, oil and gas is fed to a gravity separator, in which a bulk separation into gas, oil and water phases takes place. The oil and gas streams are combined and directed to a hydrocarbon export line, while the water stream is further cleaned in three hydrocyclones in parallel, before being purified to the final specifications in four compact flotation units. The purified water is then injected to the reservoir, or discarded into the sea. Below we describe the different parts of the separation system in more detail.

#### Bulk separation

In the bulk separation, a multiphase mixture of oil, water and gas undergoes a preliminary separation into gas, oil and water in a gravity separator. Since this separation is fairly crude, the concentrations of oil dispersed in water and of water dispersed in oil are relatively high. The water separated in the gravity separator is cleaned further in produced water treatment. The separated gas, the separated oil and rejects from the produced water treatment are directed into the transport line.

### Produced water treatment

In western Europe, discharging produced water containing oil concentrations above 30 ppm into the sea is not permitted (OSPAR, 2001). Hence, in our produced water treatment, the water produced from the bulk separation goes through additional cleaning in hydrocyclones and compact flotation units. The hydrocyclones reduce the oil concentration in water to below 100 ppm. Next, the water is further purified in a compact flotation unit, which decreases the oil content below the discharge limit of 30 ppm.

**Hydrocyclone:** Inline deoiling hydrocyclones use a swirl element at the inlet of the hydrocyclone to put the flow into a swirling motion. Because of the angular

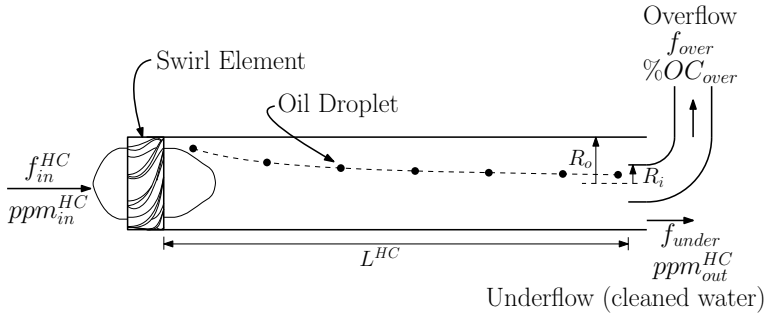


Figure 7.8: Schematic of an inline deoiling hydrocyclone, where  $L^{HC}$ ,  $R_o$ , and  $R_i$  represent dimensions.  $f_{over}$  denotes overflow,  $f_{under}$  underflow,  $f_{in}^{HC}$  water feed flow,  $ppm_{in}^{HC}$  oil concentration in water feed,  $ppm_{out}^{HC}$  oil concentration in underflow and  $\%OC_{over}$  percentage of oil fraction in overflow.

velocity of the bulk fluid, the dispersed oil droplets are radially accelerated towards the center. The oil phase accumulates near the axial center and is removed in a separate flow (overflow,  $f_{over}$ ). The rest of the flow continues into an underflow,  $f_{under}$ , as shown in Figure 7.8. The underflow is the purified water with an oil concentration below 100 ppm. The overflow is directed into the export line for transport to the topside or shore.

In the literature for HC modeling, data driven models are more prevalent in comparison to first principles models (Durdevic et al., 2015). However, they are known to be valid in a short range of operating conditions (Durdevic et al., 2017). Hence, in this paper, we use a simplified first-principles based hydrocyclone model developed by (Das and Jäschke, 2018b).

**Compact flotation unit:** The required level of 30 ppm oil concentration in water can potentially be attained with HCs. However, it is customary to use another step of water treatment, such as a CFU, to have added flexibility in the system to handle disturbances and to ensure an oil concentration below 30 ppm under all circumstances. A schematic of a CFU is shown in Figure 7.9. In a CFU, a water feed with dispersed oil droplets first undergoes a swirl motion, which leads to a fraction of oil getting separated and traveling upwards. The rest of the water with an oil concentration lower than that in the feed flows downwards and is contacted with a counter-flowing gas dispersed from the bottom. The gas forms small bubbles

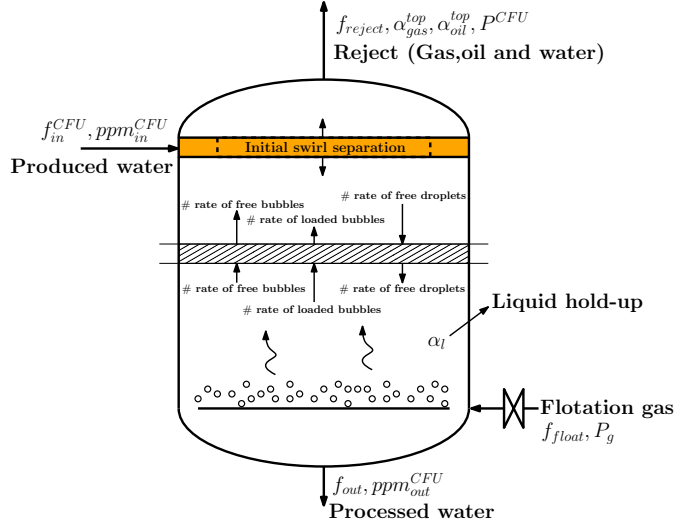


Figure 7.9: A schematic of a CFU.  $f_{in}^{CFU}$  denotes water inflow,  $ppm_{in}^{CFU}$  oil concentration in water feed,  $f_{out}$  processed water outflow,  $ppm_{out}^{CFU}$  oil concentration in water outflow,  $f_{float}$  flotation gas inflow at supply pressure  $P_g$ ,  $f_{reject}$  reject flow at pressure  $P^{CFU}$  having a gas volume fraction of  $\alpha_{gas}^{top}$  and an oil volume fraction of  $\alpha_{oil}^{top}$ . The water volume fraction in the reject flow is  $\alpha_{water}^{top} = (1 - \alpha_{gas}^{top} - \alpha_{oil}^{top})$ . The CFU is maintained at a pressure of  $P^{CFU}$  with a volumetric liquid hold-up of  $\alpha_l$ .

(free bubbles), attach to the downward flowing oil droplets to form loaded bubbles, and float them to the top. At the top of the CFU, the gas, the oil and some water is removed in a stream called reject. The purified water exits the separator from the bottom.

In this paper, we used a first-principles based CFU model, developed by (Das and Jäschke, 2018a). Other control oriented models for CFUs in the literature are data driven. Please refer to (Arvoh et al., 2012b), (Arvoh et al., 2012a) and (Asdahl and Rabe, 2013) for an overview of data driven models for CFUs and their uses.

### 7.3.2 Case study and set-up

For the simulations, we used the model parameters presented in Table 7.1. The final discretized model for the gravity separator consists of  $N_x(N_w + N_o) = 54$  control volumes. Further, we consider the same  $N_d$  droplet classes for oil dispersed in water as well as water dispersed in oil, resulting in  $N_d N_x(N_w + N_o) = 540$  differential equations, describing the change in the partial densities of the dispersed phase in each discrete cell for each of the  $N_d$  droplet classes. In addition, the equations for  $h_{oil}$ ,  $h_{water}$  and  $P_g$  lead to a total of 543 model equations for the gravity separator. Other relevant outputs of the model are water quality given by

$$ppm_{out}^{GS} = OC^{(N_x-1,1)} \times 10^6, \quad (7.52)$$

Table 7.1: Model parameters for gravity separator

Parameter	Symbol	Unit	Value
Separator length	$L$	[m]	15
Separator radius	$r$	[m]	2
Weir height	$h_{weir}$	[m]	2
Mass transfer coefficient for water	$k_w^{int}$	[m/s]	0.180217
Mass transfer coefficient for oil	$k_o^{int}$	[m/s]	0.198773
Temperature	$T$	[K]	328.5
Universal gas constant	$R_g$	[J/mol/K]	8.314
Fraction of water flow that enters water layer	$\gamma_w$	[-]	0.602039
Fraction of oil flow that enters oil layer	$\gamma_o$	[-]	0.99995
Phase inversion point in terms of water cut	$WC_p$	[-]	0.7
Phase inversion point in terms of oil cut	$OC_p$	[-]	0.3
Acceleration due to gravity	$g$	[m/s <sup>2</sup> ]	9.81
Density of pure water phase	$\rho_w$	[kg/m <sup>3</sup> ]	1000
Density of pure oil phase	$\rho_o$	[kg/m <sup>3</sup> ]	831.5
Molecular weight of gas phase	$M_g$	[kg/mol]	0.01604
Viscosity of pure water phase	$\mu_w$	[Pas]	$5 \times 10^{-4}$
Viscosity of pure oil phase	$\mu_o$	[Pas]	$1 \times 10^{-3}$
Coalescence reaction rate constants	$k_d$	[m <sup>3</sup> /s]	$1 \times 10^{-8}$
Diameter of base droplet class	$d_A$	[ $\mu$ m]	150
# of droplet classes	$N_d$	[-]	10
# of droplet-droplet coalescence reactions	$N_{reaction}$	[-]	25
# of horizontal discretizations	$N_x$	[-]	9
# of vertical discretizations in water layer	$N_w$	[-]	3
# of vertical discretizations in oil layer	$N_o$	[-]	3

and oil quality given by

$$\%WiO^{GS} = WC^{(N_x,1)} \times 100. \quad (7.53)$$

In accordance to Figure 7.7, the water flow coming out of the gravity separator is evenly distributed to three hydrocyclones, such that

$$f_{in}^{HC} = \frac{F_{water}}{3}, \quad (7.54)$$

and

$$ppm_{in}^{HC} = ppm_{out}^{GS}. \quad (7.55)$$

We consider three identical HCs in our HC system, hence,  $F_{in}^{HC} = 3f_{in}^{HC}$ ,  $F_{under} = 3f_{under}$ , and  $F_{over} = 3f_{over}$ . The total cleaned water outflow from the HCs  $F_{under}$  is then distributed evenly among the CFUs;

$$f_{in}^{CFU} = \frac{F_{under}}{4}, \quad (7.56)$$

and

$$ppm_{in}^{CFU} = ppm_{out}^{HC}. \quad (7.57)$$

We consider four identical CFUs in our CFU system, hence,  $F_{in}^{CFU} = 4f_{in}^{CFU}$ ,  $F_{out} = 4f_{out}$ ,  $F_{reject} = 4f_{reject}$ , and  $F_{float} = 4f_{float}$ .

### 7.3.3 Control structure design

We loosely follow the top-down plant-wide control design procedure by (Skogestad, 2004) for designing the control structure of the separation system. The procedure can be divided into the following steps:

#### Overall operational objective

The main objective of our subsea separation system is to maximize the flow of cleaned water out of the system. That is, we seek to maximize the operational cost given by  $J = F_{out}$ , subject to relevant operational constraints. Here, clean water refers to purified water that adheres to the regulatory emission standards (OSPAR, 2001).

#### Degrees of freedom and constraints in the gravity separator

The control degrees of freedom in the gravity separator are the gas outflow  $F_{out}^g$ , the oil outflow  $F_{oil}$  and the water outflow  $F_{water}$ , such that  $u^{GS} = [F_{out}^g \ F_{oil} \ F_{water}]$ . The changes in inlet conditions, such as the feed flow rate and the feed water cut are disturbances to the system. The weir height  $h_{weir}$  in the gravity separator is 2 m. Therefore, the oil level must be above 2 m and water level below 2 m. To keep a safety margin of 0.2 m, we constrain the oil level  $h_{oil}$  to be higher than 2.2 m and the water level  $h_{water}$  to be lower than 1.8 m. Furthermore, the oil level should be below its maximum possible value 2.5 m as a higher oil level leads to a poor gas quality and a lower buffer volume for slug handling. We consider that the separation system is situated around 50 m under the sea level, which translates into a hydrostatic pressure due to sea water of approximately 5 bara in the vicinity of the separation system. The well fluids are assumed to enter the gravity separator at a 11.07 bara pressure. In order to ensure a natural flow to topside, the pressure in the separator should not drop below a critical flow assurance pressure of 6 bara. Keeping a safety back-off of 2 bara from the critical flow assurance pressure and accounting for a pressure drop of approximately 3 bara from the feed pressure 11.07 bara, we set the operating pressure  $P_g$  to 8 bara.

#### Degrees of freedom and constraints in hydrocyclones

The total flow to the HCs and CFUs is distributed evenly to each unit, therefore the stream splits are not considered as degrees of freedom. The control degree of freedom in HCs  $u^{HC}$  is flow split  $FS = F_{over}/F_{in}^{HC}$ . The overflow valves in HC are typically designed to operate at flow splits in the range of approximately 1-3% Husveg et al. (2007). To keep a flow split back off of 0.5%, we constrain the flow split between 1.5% and 2.5%.

### Degrees of freedom and constraints in compact flotation units

The control degrees of freedom in CFUs are  $u^{CFU} = [F_{float} \ F_{out} \ F_{reject}]$ . We assume that the CFUs in our separation system are designed to be operated above 1 *bara*. At a pressure of 1 *bara*, solubility of methane in water is around 15-16 *mg/l* or *ppm* (Duan and Mao, 2006)<sup>1</sup>. Since, in our system, the produced gas as well as the flotation gas is methane, maintaining the CFU at a pressure any higher than 1 *bara* will lead to additional losses in the gas transported to the topside, as at a higher pressure water dissolves more gas. Hence, we choose a CFU pressure of 1 *bara*. Further, we constrain the  $ppm_{out}^{CFU}$  to below 10 *ppm*. Thereby, we keep a 20 *ppm* back-off from the 30 *ppm* limit, to account for fluctuations in  $ppm_{out}^{CFU}$  due to disturbances and imperfect control. A sensor for measuring gas fraction in the reject stream is assumed to be available that can accurately sense gas fraction in a range of 25-75%. For a method on gas fraction estimation in reject stream from CFU, refer to (Arvoh et al., 2012b). We keep a 20% back-off from both upper and lower limits so as to provide a larger window of accurate gas fraction measurement around the gas fraction set-point under transient conditions. Hence, we constrain the  $\alpha_{gas}^{top}$  between 45% and 55%.

### Optimal steady state operation

Combining the objective function and the constraints mentioned above results in the following steady state optimization problem:

$$\begin{aligned}
 & \max_{[u^{GS}, u^{HC}, u^{CFU}]} F_{out} \\
 & s.t. \quad \text{model equations} \\
 & \quad 2.2 \text{ m} \leq h_{oil} \leq 2.5 \text{ m} \\
 & \quad 0 \leq h_{water} \leq 1.8 \text{ m} \\
 & \quad P_g = 8 \text{ bara} \\
 & \quad 1.5\% \leq FS \leq 2.5\% \\
 & \quad p^{CFU} = 1 \text{ bara} \\
 & \quad 0 \leq ppm_{out}^{CFU} \leq 10 \\
 & \quad 0.45 \leq \alpha_{gas}^{top} \leq 0.55 \\
 & \quad 0 \leq \alpha_{oil}^{top} \leq 1 \\
 & \quad 0 \leq \alpha_{water}^{top} \leq 1
 \end{aligned} \tag{7.58}$$

We consider three different cases of inlet operating conditions. They are presented in Table 7.2. Case 1 is the nominal case, which is similar to the 1988 production data from Gullfaks-A field, used by (Backi et al., 2018). In Case 2, the total liquid production increases over that in Case 1 by 10%, which typically happens when a new well is tied-in to an existing producing well and the entire production is routed through the existing separation system. In Case 3, the total production

---

<sup>1</sup>The *ppm* contribution of the dissolved gases, such as methane is not counted in the 30 *ppm* limit of oil in water (OSPAR, 2001).

Table 7.2: Cases of inlet operating conditions

Variable	Case 1 (nominal case)	Case 2	Case 3
Liquid inflow $F_{in}^l$ , [ $m^3/h$ ]	2124.0	2336.4	2336.4
Water cut in inflow $\epsilon_{in}$ , [%]	15.0	15.0	16.5

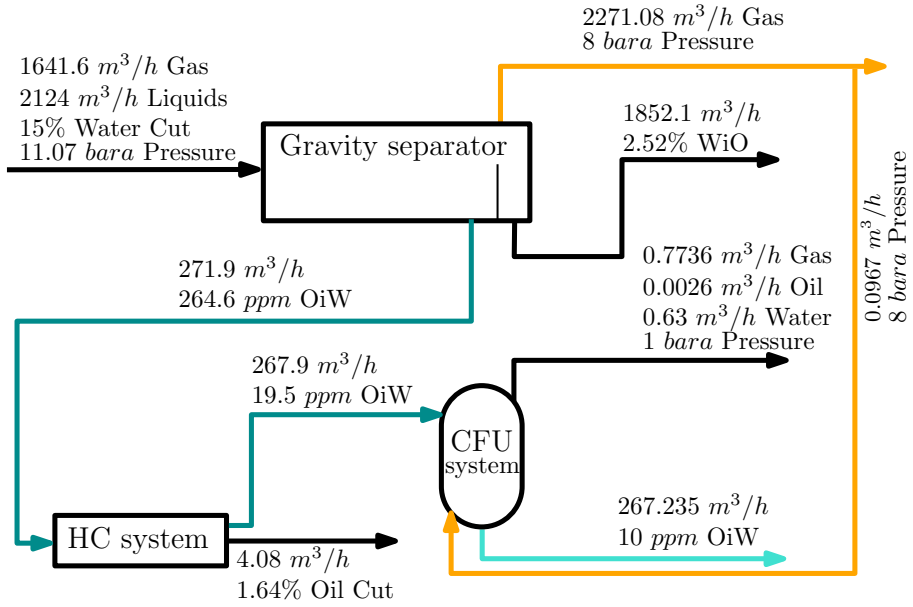


Figure 7.10: Optimal steady state solution for Case 1. HC system contains 3 HCs and CFU system contains 4 CFUs.

is the same as that in Case 2, whereas the water cut is raised by 10% from 15% to 16.5%. This indicates that the oil production drops and the water production rises, which is a typical scenario after some years of production from an oil and gas producing field.

For each case, we solved the steady state optimization problem described in (7.58). The values for important process variables for Case 1 are presented in Figure 7.10.

The optimal solutions for all the three cases are listed in Table 7.3, where separation efficiency for a separator is given by

$$\text{Separation efficiency} = \left(1 - \frac{\text{Purity of outgoing water}}{\text{Purity of incoming water}}\right). \quad (7.59)$$

We observe that the oil level in the gravity separator is always at its lowest value 2.2 m. As the optimization objective is to maximize the flow of cleaned water, the optimal oil level is determined by three competing effects - a higher residence

Table 7.3: Optimization results for different cases

Variable	Case 1	Case 2	Case 3	Comment
Gravity separator				
$h_{oil}$ , [m]	2.2	2.2	2.2	Active constraint
$h_{water}$ , [m]	1.6341	1.6217	1.5854	Not active constraint
$P_g$ , [bara]	8	8	8	Constrained
$ppm_{out}^{GS}$	264.56	272.80	251.86	
Hydrocyclone				
$ppm_{out}^{HC}$	19.51	22.25	25.07	
$FS$	1.5%	1.5%	1.5%	Active constraint
Separation efficiency	92.625%	91.846%	90.046%	
Compact flotation unit				
$P^{CFU}$ , [bara]	1	1	1	Constrained
$ppm_{out}^{CFU}$	10	10	10	Active constraint
$\alpha_{gas}^{top}$	0.55	0.55	0.55	Active constraint
Separation efficiency	48.750%	55.046%	60.113%	
$F_{out}$ , [m <sup>3</sup> /h]	267.235	289.055	319.990	Objective function
% of net water inflow cleaned	83.88%	82.48%	83.01%	

time due to a higher level, a shorter vertical distance to oil-water interface due to a lower level and a higher transfer area if the level is closer to the center of the separator. In this case considered here, the second and the third reasons dominate. The water level constraint in the gravity separator is not active for any of the cases. An explanation similar to that for the oil level is valid for the water level.

For a higher liquid inflow (Case 2) or a higher inlet water cut (Case 3), the separation load increases, which causes the oil concentration in the HC underflow,  $ppm_{out}^{HC}$ , to rise. The separation efficiency of the hydrocyclones gets worse, which is then made up by an increased separation efficiency of CFUs, due to the use of additional flotation gas.

The optimal solutions for gas hold up top in CFU for all the three cases lie at its maximum value 0.55. A higher gas hold up at the top in the CFU leads to a lower water hold up at the top, and hence a lower water loss in the reject stream. At the optimal solution, the oil content in the cleaned water from the CFU  $ppm_{out}^{CFU}$  is active at its upper limit of 10 *ppm*. This is due to two reasons - cleaning the water to below 10 *ppm* will require additional flotation gas, which will lead to a higher water loss in the reject stream, and discharging the highest permissible concentration of oil in the processed water will increase the total flow rate  $F_{out}$ .

**Steady state concentration profiles inside gravity separator:** For Case 1, the optimal steady state distributions of the droplet classes in all control volumes in the gravity separator are shown as logarithm of the number densities in Figure 7.11. As the feed contains only the lowest droplet class, all the leftmost control volumes have a relatively high number densities of small droplets. From left to right control volumes, we notice a reduction of small and medium sized droplets. This trend is a combined effect of the loss due to droplet-droplet coalescence and non-convective flow of droplets. In the medium to large droplet classes, the loss due to non-convective flow is somewhat compensated by the gain due to coalescence.

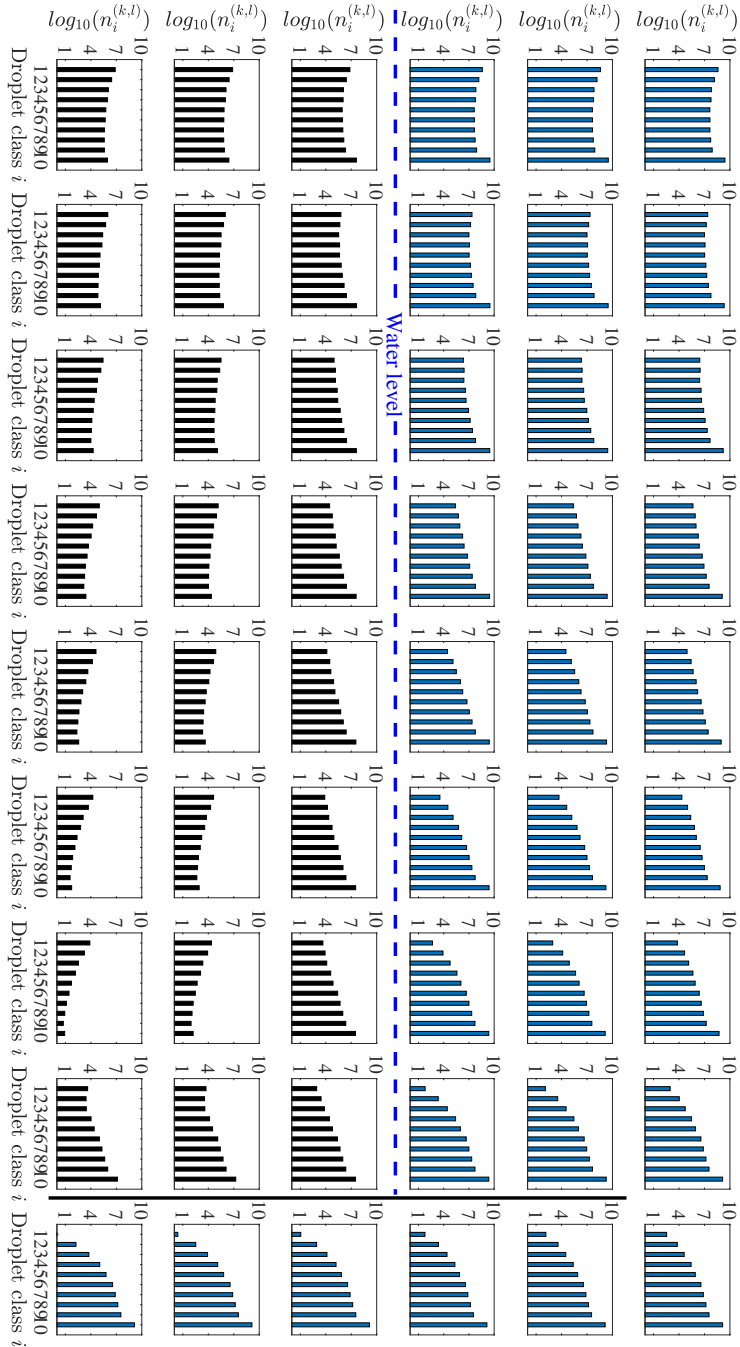


Figure 7.11: Dispersed phase number densities in all control volumes in the gravity separator corresponding to the optimal steady state for Case 1. The weir is indicated by a black line. The droplet sizes are [150, 189.0, 216.3, 238.5, 256.5, 272.6, 286.9, 300.0, 312.0, 323.2]  $\mu\text{m}$ .

Hence, the reduction in the number densities from left to right control volumes is not stark, especially in the oil layer.

In the water layer, the non-convective flows are relatively large. Hence, we see a continuous drop in the number densities of the medium to large droplet classes, in particular in the bottom two layers of control volumes. On the other hand, the number densities of the largest droplet class are relatively high in the control volumes adjacent to the oil-water interface. This is due to an accumulation of droplets resulting from no loss due to coalescence and a poor mass transport across the interface. In the oil layer, the water content increases from top to bottom control volumes due to the non-convective flow and a relatively slow mass transport of water droplets across the oil-water interface to the continuous water layer.

A similar but inverted trend can be seen in the oil droplets in the continuous water in the lower half of the figure. However, a trend that is slightly different for the water layer in comparison to the oil layer is relatively high number densities of the smallest droplet class well into the rightmost control volumes. This is a result of a slower coalescence, which happens because the oil fraction entering the water layer in the main separation zone is much lower than the water concentration entering the oil layer. This is because we assume that this separator is designed to produce a much cleaner water phase in comparison to the oil phase as water cleaning is the focus of our separation system. Besides, the sizes of the control volumes in water layer are larger than those in the oil layer, which makes the droplets travel longer distances vertically before they cross control volume boundaries and reach the oil-water interface. From bottom to top control volumes in water layer, the number densities for all classes increase due to an accumulation of droplets and a relatively slow mass transport of oil droplets across the oil-water interface to the continuous oil layer.

In the control volumes adjacent to the left of weir, we see an accumulation of the medium to large sized droplets, as also represented visually in Figure 7.4. This is because of the droplet-droplet coalescence and no non-convective flows, including no mass transfer across the oil-water interface. In all the control volumes to the right of weir, the net oil content is the same as no non-convective flows are considered in these control volumes, however, coalescence is still active, as can be seen in the disappearance of the smallest droplet class from top to bottom.

### Overall control structure and suggested pairings

The proposed control structure for the entire separation system is presented in Figure 7.12. The control pairings for each of the separators are explained in detail below.

**Gravity separator:** The pressure  $P_g$  reflects the gas inventory and is constrained for all conditions. It is controlled using the gas outflow  $F_{out}^g$ . The water inventory reflected in  $h_{water}$  is not active constraint, and should optimally vary under operation. It is controlled using the water outflow  $F_{water}$ . However, to optimally update the level according to the current operating conditions requires solving the optimization problem whenever the conditions change. This is not desirable for practical applications. Therefore, we propose to keep it at the nominally optimal set-point. This will result in suboptimal performance. We will later show that the

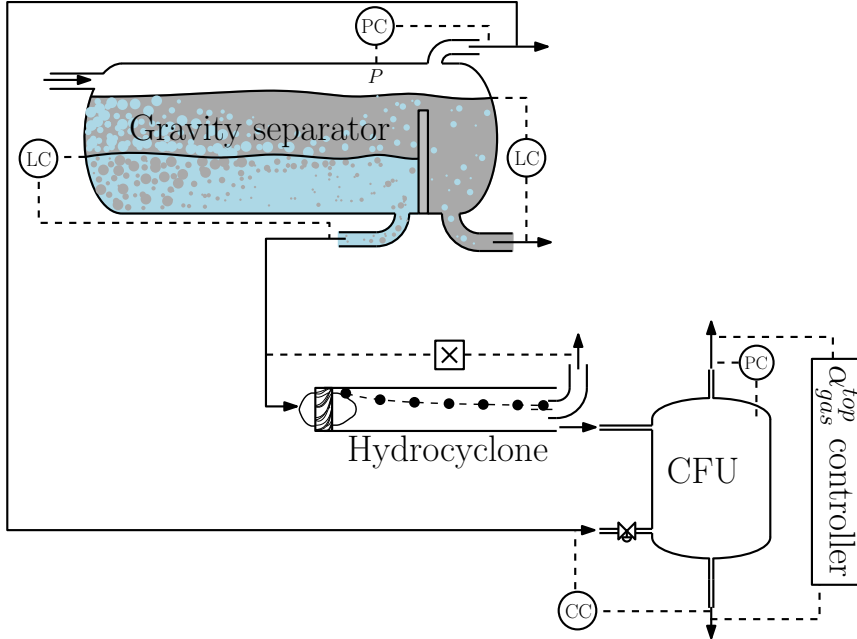


Figure 7.12: Control structure for the separation system with decentralized controllers for each separator. For all the regulatory controllers, it is assumed that the flow controllers are perfect, meaning there are no dynamics from the flow controllers to the actuators.

resulting loss is very small. The overall liquid level  $h_{oil}$  is also an active constraint, and is controlled by the oil outflow  $F_{oil}$ . The resulting pairings are

$$P_g \rightarrow F_{out}^g, \quad (7.60)$$

$$h_{oil} \rightarrow F_{oil}, \quad (7.61)$$

and

$$h_{water} \rightarrow F_{water}. \quad (7.62)$$

**Hydrocyclones:** We suggest a flow split controller with a set point of 1.5% as found in the optimization results. This controller adjusts the overflow  $F_{over}$ . In practice, a pressure drop ratio ( $PDR$ ) controller with a constant  $PDR$  set point is typically implemented (Yang et al., 2013, 2014, 2016) for the same and is shown to be equivalent to a flow split controller (Husveg et al., 2007). Since pressures are not modeled in the hydrocyclone model we use, we simulate the hydrocyclones using flow split controllers.

**Compact flotation units:** Based on the optimization results, we choose to control the variables that lie active at their constraints. These variables are  $ppm_{out}^{CFU}$ ,  $\alpha_{gas}^{top}$  and  $P^{CFU}$ . We propose to pair  $P^{CFU}$  and  $ppm_{out}^{CFU}$  with  $F_{reject}$  and  $F_{float}$  (Das and Jäschke, 2018a), respectively. The remaining degree of freedom  $F_{out}$  is

used to control the gas hold up at the top  $\alpha_{gas}^{top}$ . Hence, the resulting pairings are

$$ppm_{out}^{CFU} \rightarrow F_{float}, \quad (7.63)$$

$$P^{CFU} \rightarrow F_{reject}, \quad (7.64)$$

and

$$\alpha_{gas}^{top} \rightarrow F_{out}. \quad (7.65)$$

### 7.3.4 Analysis of the proposed control structure

Adjusting the set points to their optimal values whenever the disturbances change is not desirable in a real world application. Solving the nonlinear optimization problem in (7.58) every time the operating conditions change is impractical in most real-world applications due to the increased complexity and necessary hardware. For the disturbances considered here, the active constraints do not change, and therefore, controlling them at their bounds is always optimal. As shown in Table 7.3, there is only one variable not active at its constraint at the solution of (7.58). That variable is water level in the gravity separator, which is controlled using water outflow from gravity separator  $F_{water}$ . The optimal nominal value of  $h_{water}$  is shown in Table 7.3. By keeping  $h_{water}$  constant at its nominal set-point of 1.6341 m, we

Table 7.4: Loss in objective function value as a result of using the proposed control structure for different combinations of disturbances

Liquid inflow $F_{in}^l \rightarrow$ Water cut in $\epsilon_{in} \downarrow$	Nominal -10%	Nominal	Nominal +10%	Average loss in $F_{out}$ ( $m^3/h$ )
Nominal -10%	0.0522	0.0319	0.0186	0.0342
Nominal	0.0045	0.0000	0.0033	0.0026
Nominal +10%	0.0067	0.0270	0.0556	0.0298
Average loss in $F_{out}$ ( $m^3/h$ )	0.0211	0.0197	0.0258	0.0222

obtained an overall average loss in CFU water outflow  $F_{out}$  of 0.0222  $m^3/h$  compared to its optimal value, see Table 7.4, which shows loss as optimal objective function value minus the objective function value if the set-points for the nominal case are used. Considering that the optimal flow rate of purified water (the objective) is in the range of 218.63 to 319.99  $m^3/h$  with an average value of 267.05  $m^3/h$ , the average loss is 0.0083% of the average cleaned water flow rate. We consider it a very small and acceptable loss and hence, we conclude that the control structure is self-optimizing (Skogestad, 2000b,a; Jäschke et al., 2017). That is, the additional effort required to optimally update the water level set-point is not justified by the gain in separation performance.

### 7.3.5 Controller tunings

We select PI controllers of the form  $K_c(1 + \frac{1}{\tau_I s})$  for all feed-back control loops shown in Figure 7.12, where  $K_c$  denotes proportional gain for the controller and  $\tau_I$  integral time. The tunings have been found using SIMC rules by (Skogestad, 2003) and are given in Table 7.5.

Table 7.5: Controller tunings using SIMC rules

Controlled variable	Manipulated variable	$K_c$	$\tau_I$ (sec)	$\tau_c$ (sec)
$P_g$ [bara]	$F_{out}^g$ [ $m^3/s$ ]	-1935	20	5
$h_{oil}$ [m]	$F_{oil}$ [ $m^3/s$ ]	-0.6	400	100
$h_{water}$ [m]	$F_{water}$ [ $m^3/s$ ]	-0.0275	8000	2000
$ppm_{CFU}^{out}$	$F_{float}$ [ $m^3/h$ ]	-0.0665	2000	500
$P_{CFU}^{out}$ [bara]	$F_{reject}$ [ $m^3/h$ ]	-9.2325	400	100
$\alpha_{gas}^{top}$	$F_{out}$ [ $m^3/h$ ]	-15.3846	100	25

### 7.3.6 Closed loop simulation results

In Figures 7.13 - 7.16, we show how the system reacts dynamically to changes in inlet operating conditions, starting from Case 1, and going to Case 2 and then to Case 3 in steps at 4 h and 18 h, respectively. Though step disturbances are unlikely in real applications, we use them to demonstrate the behavior of the controllers. In addition, we introduce step changes in the set-points of the oil level and the water level in the gravity separator at 35 h and 40.55 h, respectively in order to demonstrate the behavior of the gravity separator model. Below we consider results for each separator individually.

#### Gravity separator

Figure 7.13 shows the results for the gravity separator. At 2 h, the gas inflow is raised, which causes the pressure controller to increase the gas outflow. At the transition from Case 1 to Case 2, the throughput is raised. Subsequently, the water in oil and oil in water in the outlets increase as a higher throughput causes a reduction in residence time for the fluids in the separator, causing a poorer separation performance. The inverse responses in the oil in water and water in oil on introduction of Case 2 are due to the fact that the disturbances in the inlet conditions cause the levels to rise beyond their set-points transiently, which makes the control volumes to increase in size everywhere in the separator whereas the dispersed fluids at the inlet take some time to reach the outlet. With the same dispersed phase masses in the control volumes close to the outlet and increased transient control volume sizes, the concentration first drops before reaching a new higher steady state later. The slow control of oil level causes the oil flow to react somewhat slowly, whereas the response in the water level is even slower due to an even slower control loop.

In Case 3, the inflow of water into the separator increases and that of oil reduces, which can be seen in the respective outflows as well. This leads to a reduced residence time of fluids in the water layer and a reduced concentration of oil into the water layer at the inlet. Overall, we see that the latter is the dominant effect as the oil concentration in the water outlet decreases. On the other hand, in the oil layer, the residence time of fluids is reduced and the concentration of water entering the oil layer at the inlet increases, leading to an increased water concentration in the oil outlet.

The increase in oil level set-point at 35 h causes the separation to get worse. The water content in the oil outflow increases due to fewer water droplets getting

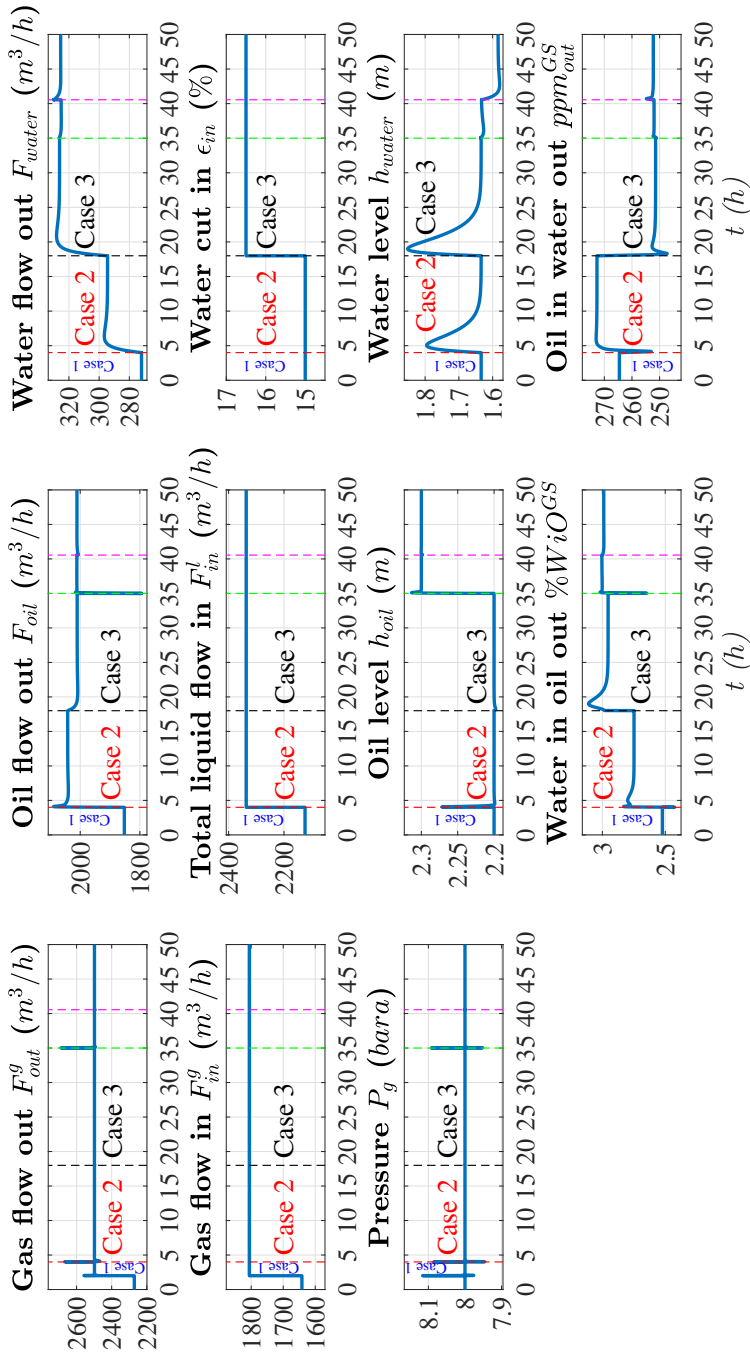


Figure 7.13: Closed loop results for gravity separator.

separated, having to travel a longer distance to reach the interface. The oil content in the water outflow increases due to reduced water transport into the water layer across the interface. The oil outflow increases due to additional water content in it, whereas the water outflow reduces. The water level set-point is reduced at 40.55  $h$ , which causes the water in oil outlet to drop due to an increased residence time in the oil layer. The oil in water outlet rises as a reduced residence time in the water layer dominates over the increased water transport across the interface.

**Concentrations profiles in selected control volumes:** Figure 7.14 presents the results for the concentrations of oil in the water phase and water in the oil phase in selected control volumes in the gravity separator. For the control volumes from top to bottom in the oil layer and bottom to top in the water layer, we notice an increase in the dispersed phase concentration. This is a result of an accumulation of dispersed phase due to a poor mass transport of dispersed phase into its respective continuous phase - a trend that is in agreement with Figure 7.11, especially for the medium to large sized droplet classes. When the inlet operating conditions change from Case 1 to Case 2, the total liquid inflow increases. This causes the concentrations of water in oil and oil in water to increase in most of the leftmost control volumes due to a reduced residence time for separation. This trend continues into the control volumes to the right as well as in the outgoing liquid streams of oil and water.

On the introduction of Case 3, the water cut increases i.e. the net water inflow rises and net oil inflow decreases, which causes more water to be dispersed in the oil phase and less oil to be dispersed in the water phase at the inlet of the separator. Hence, we observe a further increase in the water content in all the control volumes above the water level. Below the water level, we observe a reduction in oil concentration in all of the leftmost control volumes. However, the effect of an increased residence time is prominent in the increased oil concentration in the control volumes to the right, especially close to the bottom. Overall, the effect of the reduced oil feed to the water layer dominates, and consequently, we see a drop in the oil concentration in the water outlet.

The oil level increase at 35  $h$  yields an increased concentration of water in oil phase due to a larger distance that water droplets need to travel to reach the oil-water interface to get separated. However, closer to the interface, we notice a small reduction of water concentration especially in the control volumes in the left. This is due to a reduced number of water droplets coming from the top having to travel a longer distance and a higher residence time for separation of water droplets in the oil phase due to a slightly reduced oil flow. But, towards the right, the accumulation takes over and we see an increased water concentration. As a higher water concentration in the oil phase leads to a reduced water transport through the oil-water interface down to the water layer, the oil concentration increases slightly.

The water level reduction at 40.55  $h$  causes a reduction in the residence time in the water layer, which causes the oil concentration in all control volumes in water layer, except the ones at the oil-water interface, to rise due to poorer separation. Due to a higher residence time in the oil layer, more water is transported to the water layer, resulting in a reduced oil concentration in the control volumes in the water layer close to the interface. However, overall, we notice an increase in oil concentration in the water outlet, thereby confirming the dominance of the effect

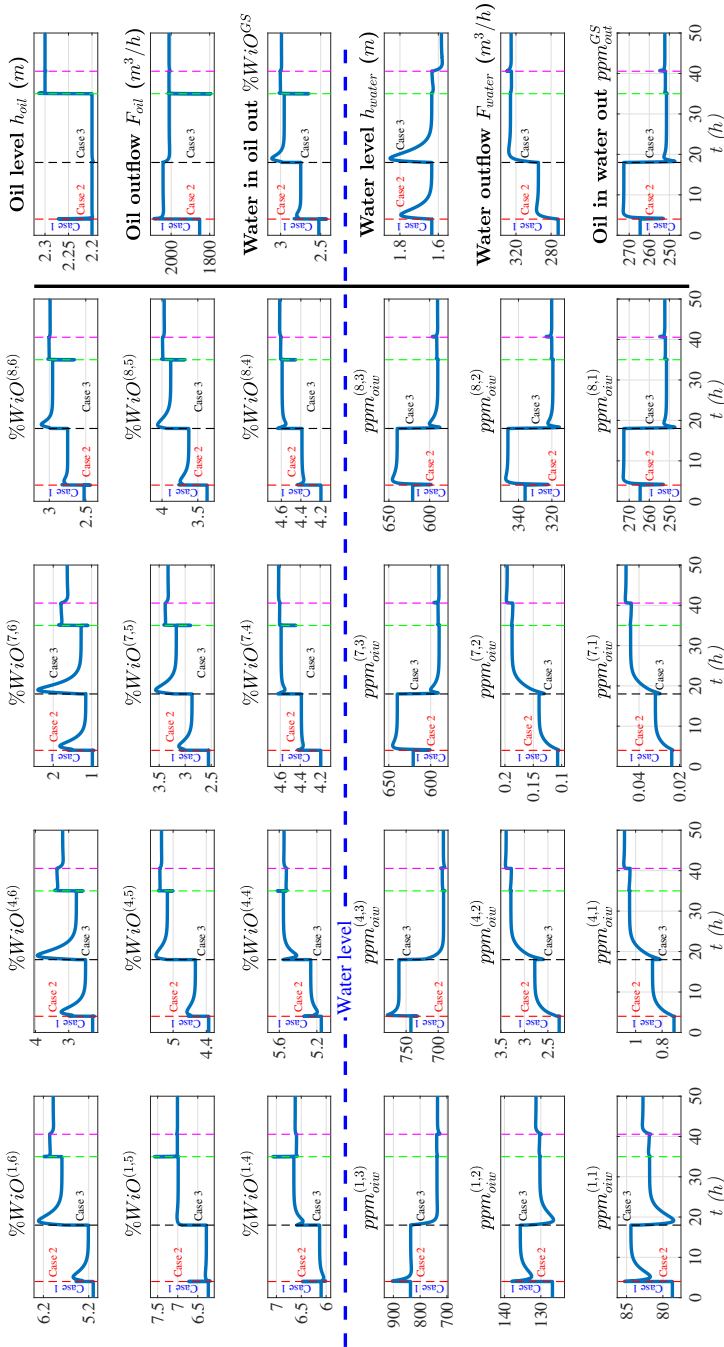


Figure 7.14: Dynamic responses in oil concentration in water and water concentration in oil in selected control volumes ( $k, l$ ) in the gravity separator. The water level is indicated by a blue dashed line dividing the figure in two halves, where the top half represents the oil layer and the bottom the water layer.

of the reduced residence time over other effects. As a result of an increased residence in the oil layer, the water concentrations in most of the control volumes are reduced. However, in the control volumes next to the interface, the water concentration rises marginally as an accumulation of the water droplets arriving from the top edges dominates over the increased water transport across the interface.

## Hydrocyclone

Figure 7.15 shows the results for the HC. The introduction of Case 2 causes an

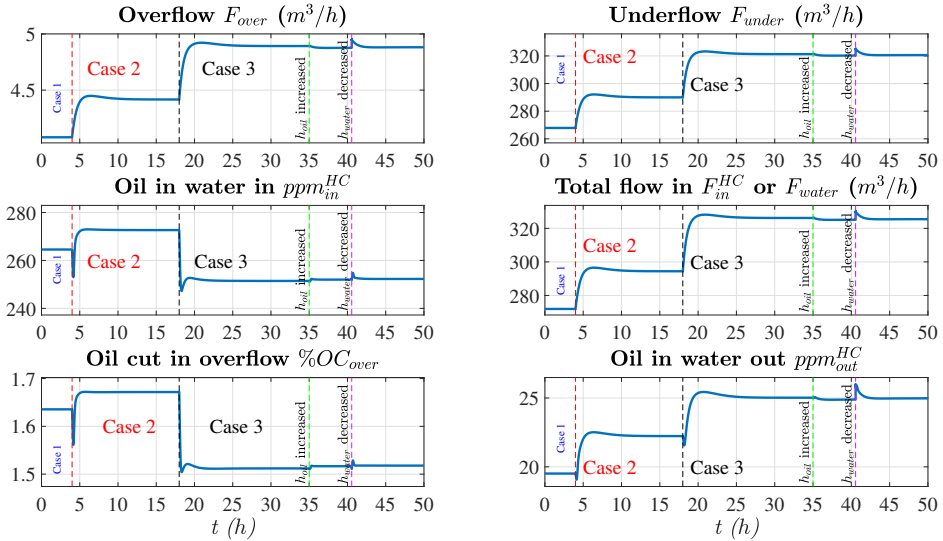


Figure 7.15: Closed loop results for hydrocyclones.

increase in feed flow as well as in feed oil concentration in water, which implies a higher load on the HC. The overflow  $F_{over}$  is adjusted such that it is equal to the product of inflow  $F_{in}^{HC}$  and a given set-point (1.5%) for the flow split  $F_{over}/F_{in}^{HC}$ . The oil in water at the outlet rises due to a poorer separation efficiency. The introduction of Case 3 causes an increase in feed flow and a reduction in feed oil concentration in water. The increased feed flow causes the overflow to increase. The resulting response of a higher oil content in the underflow despite a reduced oil concentration in the inflow is a result of a poorer separation due to a higher throughput.

The increase of oil level set-point in the gravity separator causes a reduction in the water flow, with an increase in the oil concentration therein, fed to the HC. This improves the separation efficiency of the HC and we see a reduced oil concentration in the underflow. The reduction in water level set-point in the gravity separator causes both the flow and the oil concentration of the water feed to the HC to increase. This affects the separation efficiency of the HC adversely and the oil content in the underflow rises.

### Compact flotation unit

Figure 7.16 shows the results for CFU. The underflow water from the outlet of hydrocyclones enter the CFUs. The pressure and the gas hold up top are controlled at constant set-points using reject flow and water outflow, respectively. The set-point for the gas hold up at the top is kept at its upper bound of 55%. The flotation gas flow is used as a manipulated variable to control the oil content in the water at the outlet. This loop is tuned slower than the other loops because a change in flotation gas inflow acts as a huge disturbance for the other two loops, which are expected to react quickly to satisfy the operational constraints on the pressure and the gas hold up at top. In other words, tight control of the pressure and the gas hold up top under transient conditions is prioritized over tight control of  $ppm_{out}^{CFU}$ .

On transition from Case 1 to Case 2, the water inflow and the incoming oil in water increases, causing a larger load on the CFU. Hence, the need for flotation gas flow increases. The reject stream is a vent for the gas inventory, hence the reject flow increases too in order to keep the pressure constant. Due to an increased gas inflow, the gas hold up at the top rapidly increases before it is brought back to its set point of 55% with an increased water outflow. A similar trend is observed at the introduction of Case 3 because the nature of the incoming disturbances are similar.

The increase of the oil level set-point in the gravity separator causes a reduced separation load on the CFU, which results in a reduced flotation gas usage and hence, a reduced reject flow. The reduction of the water level set-point in the gravity separator increases the separation load on the CFU, which increases the flotation gas usage and the reject flow. Since the water level controller in the gravity separator is tuned much slower than the oil level controller, the disturbances arriving to the CFU due to water level changes are much slower. Hence, it takes longer to reject those disturbances in the CFU.

In terms of optimal operation, we noticed that the values of the objective function, the water outflow from CFU for the different cases - 289.05  $m^3/h$  for Case 2 and 319.94  $m^3/h$  for Case 3 - are very close to the optimal values reported in Table 7.3. This is in agreement with the analysis of the control structure presented earlier.

## 7.4 Discussion

Necessarily, the model developed for the gravity separator has many simplifying assumptions. The influence of thermodynamics is ignored in the model, which if considered will affect the chemical compositions in the continuous as well as dispersed parts of the two phases - oil and water as a function of pressure and temperature in the separator. The gas phase will have a composition determined by fractions of components that are not dissolved in either water or oil. Since the pressure in the separator is tightly controlled, it can be assumed constant and the temperature is given by that of the incoming flow, which also does not change rapidly. Hence, for most practical purposes, the compositions of the three phases at the inlet of the separator can be considered constant if there are no fluctuations in the composition of the incoming well fluids. The inlet compositions will then decide the physical

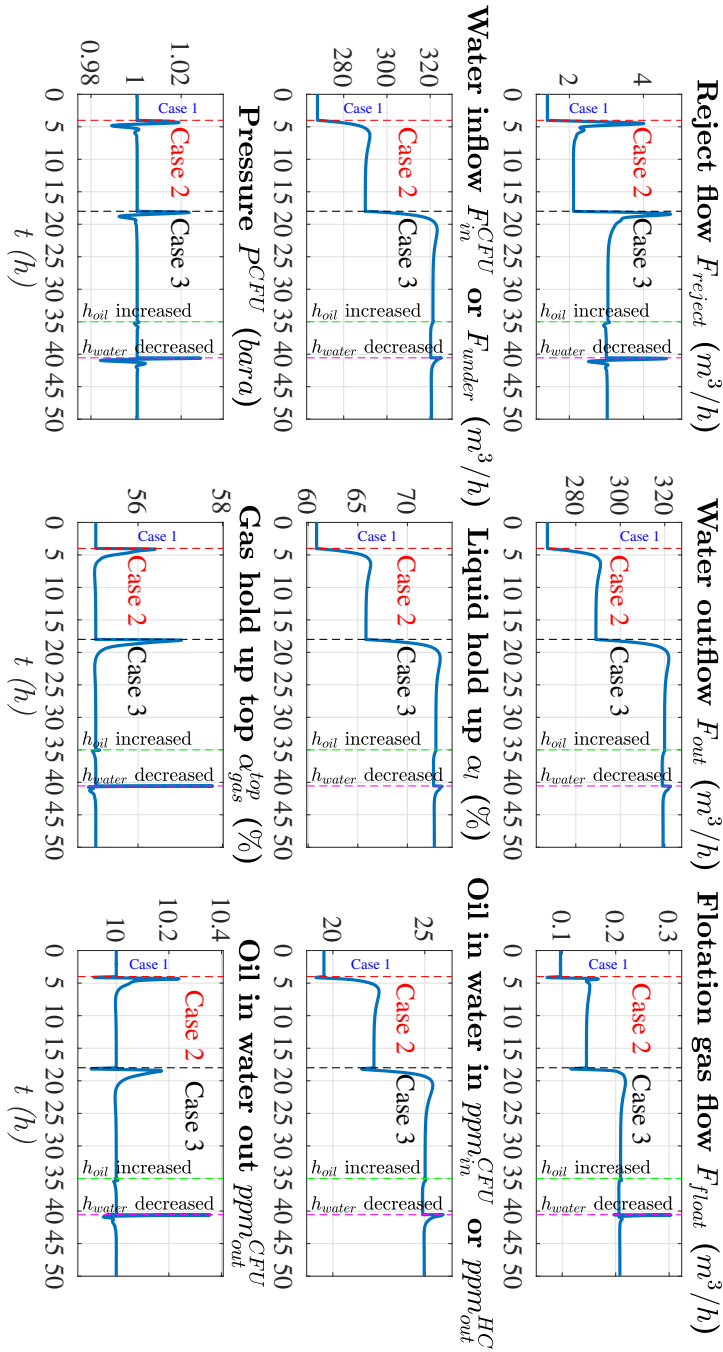


Figure 7.16: Closed loop results for compact flotation unit with regulatory control of pressure, gas hold-up top and  $ppm_{CFU}$ .

properties, such as viscosities and densities of the phases. If the physical properties as determined by thermodynamics are included, the rest of the model will be valid in its current state.

The model also assumes a fixed base droplet size and a finite set of droplet classes, which will not be true in a realistic setting. The droplet classes will be different and not discrete. Further, in this model we used a single constant value for the droplet-droplet coalescence reaction rate constant  $k_d$ . This rate constant is inversely proportional to the coalescence time  $t_{coal}$  as  $k_d \propto 1/t_{coal}$ , which means the lower the coalescence time, the higher the coalescence rate. Many models from literature assume that the coalescence time is proportional to the droplet size (Hahn and Slattery, 1985; Chesters, 1991; Lobo et al., 1993), indicating that in real systems, the  $k_d$  will decrease as the droplets grow in size. However, the  $k_d$  values for all droplet classes can, in general, be raised using external modules, such as electro-coalescers equipped in separators, or adding chemicals, such as demulsifiers. Lastly, the  $k_d$  values will be different for dispersed water in continuous oil and dispersed oil in continuous water and they need to be determined through experimental investigations, which is beyond the scope of this work.

In the dynamic simulation results, we noticed inverse responses in the concentration variables in the gravity separators. This response may have been avoided if the levels in the separator were considered to have a wave that travels through the separator in the axial direction. However, considering the wave would have made the model much more complex, hence, a flat level was assumed, as is commonly done in literature (Sayda and Taylor, 2007; Backi and Skogestad, 2017).

We presented results for different cases of inlet operating conditions. Our analysis suggests that the set-points of the controlled variables in the separation system do not need to be changed in order to maintain near optimal operation under changes in inlet conditions. Hence, we chose to not update the set-points when disturbances arrive. The constant set point policy (self-optimizing control) results in a very small loss, which is supported by the analysis of the control structure as well as dynamic simulations for Cases 1-3. Therefore, the control structure proposed in this paper is able to maintain near optimal operation under changing inlet operating conditions without having to change the set-points of the important controlled variables.

## 7.5 Conclusion

In this work, we developed a coalescence based gravity separator model, which can dynamically predict oil content in water and water content in oil to changes in inlet operating conditions and set-points for controlled variables. The model considers changes in gas inflow, total liquid inflow and water cut in the liquid inflow as disturbances, and separator pressure, oil level and water level as controlled variables.

Further, the gravity separator model has been used with existing literature models for hydrocyclones and compact flotation units, to model a subsea separation system that separates and then purifies water produced in the hydrocarbon production. This separation system has been used to optimize the process and

find a control structure that enables near optimal operation, where the objective is to maximize water removal through the separation system under varying inlet operating conditions.

In the optimization results, a detailed analysis of the evolution of dispersed droplet distribution inside the gravity separator has been presented. The optimal solution for the nominal case also provided the set-points for the variables that are controlled by the regulatory control layer. Thereafter, the closed loop results for each separator are presented and discussed in detail, along with an extended analysis of the dispersed phase concentration profiles within selected control volumes inside the gravity separator. The proposed control strategy has been shown to yield near-optimal operation without the need for a supervisory RTO layer or changes to the set-points.

## 7.6 Acknowledgements

The authors thank the project [SUBPRO](#) (Subsea production and processing) and the Norwegian Research Council for financial support. Johannes Jäschke acknowledges financial support by DNV GL.



## Part IV

# Closing remarks



## Chapter 8

# Conclusion and future work

### 8.1 Conclusions

The overall objective of this thesis is to present a basis for the control of important process variables for optimal operation of oil and gas separation processes, and a basis for the estimation of unmeasured variables. To structure the overall objective, the thesis was divided into three main parts. Each of the parts and their purpose are described below:

**Part I:** In this part, the need for models for the purpose of determining suitable operating points for an oil-water separation system was demonstrated. A simplified steady state model was developed for each of the constituent separators and these models were combined together to create a separation system. The overall oil content in the oily product was maximized using the degrees of freedom relating to each of the separators. The optimal solution provided the optimal way to operate this system.

Though the insight about the optimal operation is useful, it is important to note that this analysis could not be carried out without the knowledge of important variables from a real separation system. To either create a data driven model or to validate a first-principles model, real data of important variables is necessary. It could be assumed that the variables needed to develop these models are available via measurements during the testing phase. However, some of these variables may not be available as measurement data when a system is in operation. There comes the need for an estimator to provide these missing variables. Hence, in part **II**, some estimation results were presented. Also, every estimator needs dynamic process models as a prerequisite. Hence, that gap was partially fulfilled in part **II** and more wholly fulfilled in part **III**.

**Part II:** This part showed the use of estimation methods and simplified models for estimation of unmeasured variables along with alleviating some of the challenges encountered by advanced estimators. In chapter 3, some unmeasured inlet disturbances to a gravity separator were estimated using an extended Kalman filter and a simplified gravity separator model. In chapter 4, a method called pathfollowing was introduced to moving horizon estimation in order to reduce the computational burden relating to solving the numerical problem that results from a moving horizon

estimator.

**Part III:** This part presented three dynamic models, one each for - inline deoiling hydrocyclone, compact flotation unit and gravity separator and later combined them all together into a dynamic subsea separation system in order to study its optimal operation as well as its transient behavior. The models were developed by discretization of the separators into control volumes and then writing simplified mass balance equations on each of the control volumes. Models of this kind were not developed or studied in the literature. These models are able to predict important variables, such as oil concentration in water and water concentration in oil, which are difficult to measure in practice. Especially, for the analysis of a separation system in terms of separation efficiency, the knowledge of these variables are crucial. The analysis of the separation system revealed that optimal operation should not be studied for a standalone separator, but for a system. Also, the desired transient behavior from each of the separators can be obtained by tuning the lower level controllers for each of the separators in a way that takes into account the transient responses in the other separators.

## 8.2 Future work

### 8.2.1 Validation of the models

The models in this thesis have been developed based on a qualitative understanding of processes. For developing the models, very little data from real operation have been used. Hence, the next step is to validate each of the models.

### 8.2.2 Optimal operation of a validated separation system

The optimal operating conditions identified by the use of a set of unvalidated models in chapter 7 is misleading for the operation of a real separation system. Therefore, the optimal operating conditions need to be re-identified once the models are validated and the operational constraints are updated. The approaches presented in part III could be useful for this analysis.

### 8.2.3 Estimation using the validated models

The developed models once validated can be used to study estimation of important variables that are difficult to measure in practice. Methods described in part II can be useful for this study. If estimation using a feedback of measured entities is not possible, a once validated model can also be run in parallel to a real process with a periodic update of the model. The variables generated thereby can be used in the decision support system, such as a controller or by an operator to run the plant as desired.

## 8.3 Guidelines for developing models

For developing models, the most important pre-requisite is the understanding of the process being modeled. A model is a mere reflection of that understanding.

However, the methods used to develop models are often not very trivial. As a model developer, one should focus on expressing the understanding of the process in the simplest possible mathematical form that captures the most important details, while keeping the future use of the model in mind. For use in optimization or estimation, most of the modern solvers require that the model has important properties, such as differentiability. The property of differentiability cannot be guaranteed in every model, however, to know that not having this property hinders the future use of the model to a large extent is a huge incentive to look for other more reasonable alternatives already at the modeling phase. These aspects have been taken into consideration for developing models presented in this thesis, particularly in part III. The approaches for model development used in this thesis are, perhaps, applicable to other disciplines in which models are necessary.

For process models, it is often said that “All models are incorrect, only some are useful”. The incorrectness of models can be attributed to the inability to obtain comprehensive understanding of any real process. However, a model can be useful, if a clear application was kept in mind while developing it.

## 8.4 Use of models in process industry

In industry, for online control of processes, the use of first-principles based models is rather limited and in general, the influence of models on direct operation is mitigated. This choice is justified by the high level of uncertainty associated with the process models’ ability to accurately predict future process behavior in real applications. Models derived from first-principles have many underlying simplifying assumptions, as also seen in this thesis, which ignore many phenomena and the influence of unknown disturbances. These assumptions may not hold in real applications.

When a model is really necessary for online use in industry, a data driven model is preferred. On the other hand, first-principles models are often used for offline use in industry, such as for analysis of optimal operation, to test strategies to conduct a start-up or shut-down smoothly and quickly or to test different control strategies, to name a few. These models also find use in a wide variety of “not in the loop” online analysis, such as for monitoring of process performance and equipment condition through computation of indices, such as key performance indicator (KPI).

Based on this background, the work produced in this thesis may find some suitable applications in industry, however, they may not be of “in the loop” online type.

*In process control, the simplest methods are often the best ones.*



# References

- Joel Andersson. *A general-purpose software framework for dynamic optimization*. PhD thesis, Arenberg Doctoral School, KU Leuven, Department of Electrical Engineering (ESAT/SCD) and Optimization in Engineering Center, Kasteelpark Arenberg 10, 3001-Heverlee, Belgium, 2013.
- Joel Andersson, Johan Åkesson, and Moritz Diehl. Casadi: A symbolic package for automatic differentiation and optimal control. In *Recent advances in algorithmic differentiation*, pages 297–307. Springer, 2012.
- Richard Arntzen. *Gravity separator revamping*. PhD thesis, Norwegian University of Science and Technology Trondheim, Norway, 2001.
- Benjamin Kaku Arvoh, Steinar Asdahl, Karsten Rabe, Rolf Ergon, and Maths Halstensen. Online estimation of reject gas and liquid flow rates in compact flotation units for produced water treatment. *Flow Measurement and Instrumentation*, 24:63–70, 2012a. doi: 10.1016/j.flowmeasinst.2012.03.008.
- Benjamin Kaku Arvoh, Steinar Asdahl, Karsten Rabe, and Maths Halstensen. Online estimation of reject gas flow rates in compact flotation units for produced water treatment: A feasibility study. *Chemometrics and Intelligent Laboratory Systems*, 114:87–98, 2012b. doi: 10.1016/j.chemolab.2012.03.008.
- Steinar Asdahl and Karsten Rabe. Real-time automatic operation and optimization of produced-water treatment. In *SPE Middle East Intelligent Energy Conference and Exhibition*. Society of Petroleum Engineers, 2013. doi: 10.2118/167492-MS.
- Christoph J Backi and Sigurd Skogestad. A simple dynamic gravity separator model for separation efficiency evaluation incorporating level and pressure control. In *American Control Conference (ACC), 2017*, pages 2823–2828. IEEE, 2017.
- Christoph J Backi, Brian A Grimes, and Sigurd Skogestad. A control-and estimation-oriented gravity separator model for oil and gas applications based upon first-principles. *Industrial & Engineering Chemistry Research*, 57(21):7201–7217, 2018.
- Chris Baggs, Ian Kent, and John Allen. Troll pilot control system: advanced control system for a subsea separator. In *Offshore Technology Conference*. Offshore Technology Conference, 2000.

- Subash Balakrishna and Lorenz T. Biegler. Targeting strategies for the synthesis and energy integration of nonisothermal reactor networks. *Industrial & Engineering Chemistry Research*, 31(9):2152–2164, 1992. doi: 10.1021/ie00009a013.
- Mike Bhatnagar and Carl Johan Sverdrup. Advances in compact flotation units (cfus) for produced water treatment. In *Offshore Technology Conference-Asia*. Offshore Technology Conference, 2014. doi: 10.4043/24679-MS.
- B. Bringedal, T. Ingebretsen, and K. Haugen. Subsea separation and reinjection of produced water. In *Offshore Technology Conference*. Offshore Technology Conference, 1999.
- Denis Brondel, Randy Edwards, Andrew Hayman, Donald Hill, Shreekant Mehta, and Tony Semerad. Corrosion in the oil industry. *Oilfield review*, 6(2):4–18, 1994.
- A.K. Chesters. Modelling of coalescence processes in fluid-liquid dispersions: a review of current understanding. *Chemical engineering research and design*, 69(A4):259–270, 1991.
- A. Constantinides and N. Mostoufi. *Numerical Methods for Chemical Engineers with MATLAB Applications*. Prentice-Hall Inc., Upper Saddle River, New Jersey, 1999.
- Tamal Das and Johannes Jäschke. A simplified first-principles model of a compact flotation unit for use in optimization and control. *Submitted for publication in Industrial and Engineering Chemistry Research*, 2018a.
- Tamal Das and Johannes Jäschke. Modeling and control of an inline deoiling hydrocyclone. *IFAC-PapersOnLine*, 51(8):138–143, 2018b.
- Tamal Das, Preben Fürst Tyvold, and Johannes Jäschke. Modelling and optimization of compact subsea liquid-liquid separation system. In *Computer Aided Chemical Engineering*, volume 38, pages 1255–1260. Elsevier, 2016.
- Tamal Das, Christoph J Backi, and Johannes Jäschke. A model for subsea oil-water gravity separator to estimate unmeasured disturbances. In *Computer Aided Chemical Engineering*, volume 40, pages 1489–1494. Elsevier, 2017.
- M. Dirkzwanger. *A New Axial Cyclone Design for Fluid-Fluid Separation*. PhD thesis, Delft University of Technology, 1996.
- Zhenhao Duan and Shide Mao. A thermodynamic model for calculating methane solubility, density and gas phase composition of methane-bearing aqueous fluids from 273 to 523 k and from 1 to 2000 bar. *Geochimica et Cosmochimica Acta*, 70(13):3369–3386, 2006.
- Marcin Dudek, Eugénie Kancir, and Gisle Øye. Influence of the crude oil and water compositions on the quality of synthetic produced water. *Energy & Fuels*, 31(4): 3708–3716, 2017.

- Petar Durdevic, Simon Pedersen, Mads Bram, Dennis Hansen, Abdiladif Hassan, and Zhenyu Yang. Control oriented modeling of a de-oiling hydrocyclone. *IFAC-PapersOnLine*, 48(28):291–296, 2015.
- Petar Durdevic, Simon Pedersen, and Zhenyu Yang. Evaluation of oiw measurement technologies for deoiling hydrocyclone efficiency estimation and control. In *OCEANS 2016-Shanghai*, pages 1–7. IEEE, 2016.
- Petar Durdevic, Simon Pedersen, and Zhenyu Yang. Challenges in modelling and control of offshore de-oiling hydrocyclone systems. In *Journal of Physics: Conference Series*, volume 783. IOP Publishing, 2017.
- Mona Eftekhardadkhah, Svein Viggo Aanesen, Karsten Rabe, and Gisle Øye. Oil removal from produced water during laboratory-and pilot-scale gas flotation: The influence of interfacial adsorption and induction times. *Energy & Fuels*, 29(11): 7734–7740, 2015. doi: 10.1021/acs.energyfuels.5b02110.
- Ahmadun Fakhru’l-Razi, Alireza Pendashteh, Luqman Chuah Abdullah, Dayang Radiah Awang Biak, Sayed Siavash Madaeni, and Zurina Zainal Abidin. Review of technologies for oil and gas produced water treatment. *Journal of hazardous materials*, 170(2):530–551, 2009. doi: 10.1016/j.jhazmat.2009.05.044.
- Anthony V Fiacco. *Introduction to sensitivity and stability analysis in nonlinear programming*. Elsevier, 1983.
- Rolf Findeisen and Frank Allgöwer. Computational delay in nonlinear model predictive control. In *Proc. Int. Symp. Adv. Contr. of Chem. Proc.*, pages 427–432, 2004.
- Ted Frankiewicz, C-M Lee, and K Juniel. Compact induced gas flotation as an effective water treatment technology on deep water platforms. In *Offshore Technology Conference*. Offshore Technology Conference, 2005. doi: 10.4043/17612-MS.
- Tom Frising, Christine Noik, and Christine Dalmazzone. The liquid/liquid sedimentation process: from droplet coalescence to technologically enhanced water/oil emulsion gravity separators: a review. *Journal of dispersion science and technology*, 27(7):1035–1057, 2006.
- Ann Christin Gjerdsseth, Audun Faanes, and Rune Ramberg. The tordis ior project. In *Offshore technology conference*. Offshore Technology Conference, 2007.
- P.S. Hahn and J.C. Slattery. Effects of surface viscosities on the stability of a draining plane parallel liquid film as a small bubble approaches a liquid-gas interface. *AIChE journal*, 31(6):950–956, 1985.
- A Hallanger, F Soenstaboe, and T Knutsen. A simulation model for three-phase gravity separators. In *SPE Annual Technical Conference and Exhibition*. Society of Petroleum Engineers, 1996.
- Ernst WM Hansen. Phenomenological modelling and simulation of fluid flow and separation behavior in offshore gravity separators. *ASME-PUBLICATIONS-PVP*, 431:23–30, 2001.

- S Hartland and SAK Jeelani. Choice of model for predicting the dispersion height in liquid/liquid gravity settlers from batch settling data. *Chemical engineering science*, 42(8):1927–1938, 1987.
- Eric L Haseltine and James B Rawlings. Critical evaluation of extended kalman filtering and moving-horizon estimation. *Industrial & engineering chemistry research*, 44(8):2451–2460, 2005.
- A Hayatdavoudi, M Howdeshell, E Godeaux, N Pednekar, and V Dhumal. Performance analysis of a novel compact flotation unit. *Journal of energy resources technology*, 133(1):013101, 2011. doi: 10.1115/1.4003497.
- Sindre J Heggheim. Modelling and control of coalescence based gravity separators in a subsea separation system. Master’s thesis, Norwegian University of Science and Technology, Trondheim, Norway, 2018.
- Martin Henschke, Lars Holger Schlieper, and Andreas Pfennig. Determination of a coalescence parameter from batch-settling experiments. *Chemical Engineering Journal*, 85(2):369–378, 2002.
- Terje Horn, William Bakke, and Gunnar Eriksen. Experience in operating world’s first subsea separation and water injection station at troll oil field in the north sea. In *Offshore Technology Conference*. Offshore Technology Conference, 2003.
- Trygve Husveg, Odile Rambeau, Tormod Drenngstig, and Torleiv Bilstad. Performance of a deoiling hydrocyclone during variable flow rates. *Minerals Engineering*, 20(4):368–379, 2007.
- Johannes Jäschke, Xue Yang, and Lorenz T Biegler. Fast economic model predictive control based on nlp-sensitivities. *Journal of Process Control*, 24(8):1260–1272, 2014.
- Johannes Jäschke, Yi Cao, and Vinay Kariwala. Self-optimizing control—a survey. *Annual Reviews in Control*, 43:199–223, 2017.
- SAK Jeelani and S Hartland. Prediction of steady state dispersion height from batch settling data. *AIChE journal*, 31(5):711–720, 1985.
- SAK Jeelani and Stanley Hartland. The continuous separation of liquid/liquid dispersions. *Chemical engineering science*, 48(2):239–254, 1993.
- SAK Jeelani, R Hosig, and EJ Windhab. Kinetics of low reynolds number creaming and coalescence in droplet dispersions. *AIChE journal*, 51(1):149–161, 2005.
- Krisorn Jittorntrum. Solution point differentiability without strict complementarity in nonlinear programming. In *Sensitivity, Stability and Parametric Analysis*, pages 127–138. Springer, 1984.
- Sunil Lalchand Kokal. Crude oil emulsions: A state-of-the-art review. *SPE Production & facilities*, 20(01):5–13, 2005.

- Przemyslaw B Kowalczyk and Jan Drzymala. Physical meaning of the sauter mean diameter of spherical particulate matter. *Particulate Science and Technology*, 34(6):645–647, 2016.
- Peter Kühl, Moritz Diehl, Tom Kraus, Johannes P Schlöder, and Hans Georg Bock. A real-time algorithm for moving horizon state and parameter estimation. *Computers & chemical engineering*, 35(1):71–83, 2011.
- Vyacheslav Kungurtsev and Moritz Diehl. Sequential quadratic programming methods for parametric nonlinear optimization. *Computational Optimization and Applications*, 59(3):475–509, 2014.
- Yixiang Liao and Dirk Lucas. A literature review on mechanisms and models for the coalescence process of fluid particles. *Chemical Engineering Science*, 65(10):2851–2864, 2010.
- Lloyd Lobo, Ivan Ivanov, and Darsh Wasan. Dispersion coalescence: Kinetic stability of creamed dispersions. *AIChE journal*, 39(2):322–334, 1993.
- Rodrigo López-Negrete and Lorenz T Biegler. A moving horizon estimator for processes with multi-rate measurements: A nonlinear programming sensitivity approach. *Journal of Process Control*, 22(4):677–688, 2012.
- Rodrigo Lopez Negrete de la Fuente. *Nonlinear Programming Sensitivity Based Methods for Constrained State Estimation*. PhD thesis, Carnegie Mellon University, 2011.
- M Maelum and K Rabe. Improving oil separation from produced water using new compact flotation unit design. In *SPE Production and Operations Symposium*. Society of Petroleum Engineers, 2015. doi: 10.2118/173589-MS.
- R Moosai and RA Dawe. Oily wastewater cleanup by gas flotation. *West Indian J. Eng*, 25(1):25–41, 2002.
- AF Najafi, SM Mousavian, and K Amini. Numerical investigations on swirl intensity decay rate for turbulent swirling flow in a fixed pipe. *International Journal of Mechanical Sciences*, 53(10):801–811, 2011.
- JH Neuenkirchen. Tordis subsea separation boosting and injection (ssbi) project: Project presentation and description of the production control system. In *Subsea Controls and Data Acquisition 2006: Controlling the Future Subsea*. Society of Underwater Technology, 2006.
- L Neumann, ET White, and T Howes. What does a mean size mean? In *Chemeca 2003: Products and Processes for the 21st Century: Proceedings of the 31st Australasian Chemical Engineering Conference*, page 928. Institution of Engineers, Australia, 2003.
- RCG Oliveira, G Gonzalez, and JF Oliveira. Interfacial studies on dissolved gas flotation of oil droplets for water purification. *Colloids and Surfaces A: Physicochemical and Engineering Aspects*, 154(1):127–135, 1999. doi: 10.1016/S0927-7757(98)00890-5.

- Rene Orłowski, Mauro Luiz Lopes Euphemio, Mauro Lopes Euphemio, Cynthia Azevedo Andrade, Flavia Guedes, Luis Carlos Tosta da Silva, Rafael Guimaraes Pestana, Gustavo de Cerqueira, Igor Lourenço, and Alexandre Pivari. Marlim 3 phase subsea separation system-challenges and solutions for the subsea separation station to cope with process requirements. In *Offshore Technology Conference*. Offshore Technology Conference, 2012.
- OSPAR. Discharges, ospar convention, 2001. URL [www.ospar.org/work-areas/oic/discharges](http://www.ospar.org/work-areas/oic/discharges).
- Paul Pavelic, Joanne Vanderzalm, Peter Dillon, Andrew Herczeg, Karen Barry, Kerry Levett, Joao Mimoso, and Paul Magarey. Assessment of the potential for well clogging associated with salt water interception and deep injection at chowilla, sa. *Final Report to Department of Water, Land, Biodiversity and Conservation*, pages 13–27, 2007.
- C Hank Rawlins and Chien Ly. Mechanisms for flotation of fine oil droplets. *Separation Technologies for Minerals, Coal, and Earth Resources*, page 307, 2012.
- CHP Ribeiro, SC Miyoshi, AR Secchi, and A Bhaya. Model predictive control with quality requirements on petroleum production platforms. *Journal of Petroleum Science and Engineering*, 137:10–21, 2016.
- T Ruud, A Idrac, LJ McKenzie, and SH Høy. All subsea: A vision for the future of subsea processing. In *Offshore Technology Conference*. Offshore Technology Conference, 2015.
- Atalla F Sayda and James H Taylor. Modeling and control of three-phase gravity separators in oil production facilities. In *American Control Conference, 2007. ACC'07*, pages 4847–4853. IEEE, 2007.
- D Shannon. Developments in micro-footprint, multi-stage flotation, 2016.
- Dan Simon. *Optimal state estimation: Kalman, H infinity, and nonlinear approaches*. John Wiley & Sons, 2006.
- Sigurd Skogestad. Plantwide control: The search for the self-optimizing control structure. *Journal of process control*, 10(5):487–507, 2000a.
- Sigurd Skogestad. Self-optimizing control: The missing link between steady-state optimization and control. *Computers & Chemical Engineering*, 24(2-7):569–575, 2000b.
- Sigurd Skogestad. Simple analytic rules for model reduction and pid controller tuning. *Journal of process control*, 13(4):291–309, 2003.
- Sigurd Skogestad. Control structure design for complete chemical plants. *Computers & Chemical Engineering*, 28(1-2):219–234, 2004.
- Jesse Jonathan Slot. *Development of a centrifugal in-line separator for oil-water flows*. PhD thesis, University of Twente, 2013.

- 
- P Matthew Spiecker, Keith L Gawrys, Chad B Trail, and Peter K Kilpatrick. Effects of petroleum resins on asphaltene aggregation and water-in-oil emulsion formation. *Colloids and surfaces A: Physicochemical and engineering aspects*, 220(1-3):9–27, 2003.
- Eka Suwartadi, Vyacheslav Kungurtsev, and Johannes Jäschke. Sensitivity-based economic nmpc with a path-following approach. *Processes*, 5(1):8, 2017.
- Preben Fürst Tyvold. Modeling and optimization of a subsea oil-water separation system. Master’s thesis, NTNU, 2015.
- L. van Campen. *Bulk Dynamics of Droplets in Liquid-Liquid Axial Cyclones*. PhD thesis, Delft University of Technology, 2014.
- Andreas Wächter and Lorenz T Biegler. On the implementation of an interior-point filter line-search algorithm for large-scale nonlinear programming. *Mathematical programming*, 106(1):25–57, 2006.
- Zhenyu Yang, Jens Peter Stigkær, and Bo Løhndorf. Plant-wide control for better de-oiling of produced water in offshore oil & gas production. In *ICONS*, pages 45–50, 2013.
- Zhenyu Yang, Simon Pedersen, and Petar Durdevic. Cleaning the produced water in offshore oil production by using plant-wide optimal control strategy. In *Oceans-St. John’s, 2014*, pages 1–10. IEEE, 2014.
- Zhenyu Yang, Simon Pedersen, Petar Durdevic, Christian Mai, Leif Hansen, Kasper Jepsen, Alexandre Aillos, and Anders Andreasen. Plant-wide control strategy for improving produced water treatment. 2016.
- Victor M Zavala, Carl D Laird, and Lorenz T Biegler. A fast moving horizon estimation algorithm based on nonlinear programming sensitivity. *Journal of Process Control*, 18(9):876–884, 2008.